Annals of Physics 439 (2022) 168763

Contents lists available at ScienceDirect

Annals of Physics

journal homepage: www.elsevier.com/locate/aop

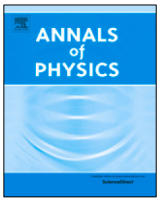

Large-*N* Chern insulators: Lattice field theory and quantum simulation approaches to correlation effects in the quantum anomalous Hall effect

L. Ziegler [a], E. Tirrito [b,c], M. Lewenstein [c,d], S. Hands [e], A. Bermudez [a,*]

[a] *Departamento de Física Teórica, Universidad Complutense, 28040 Madrid, Spain*
[b] *SISSA, Via Bonomea 265, 34136 Trieste, Italy*
[c] *ICFO - Institut de Ciències Fotòniques, The Barcelona Institute of Science and Technology, Av. Carl Friedrich Gauss 3, 08860 Castelldefels (Barcelona), Spain*
[d] *ICREA, Lluis Companys 23, 08010 Barcelona, Spain*
[e] *Department of Mathematical Sciences, University of Liverpool, Liverpool L69 3BX, United Kingdom*

ARTICLE INFO

Article history:
Received 4 January 2022
Accepted 13 January 2022
Available online 21 January 2022

Keywords:
Correlated Chern insulators
Quantum anomalous Hall effect
Four-Fermi lattice field theories
Large-N methods
tensor networks

ABSTRACT

Four-Fermi quantum field theories in (2+1) dimensions lie among the simplest models in high-energy physics, the understanding of which requires a non-perturbative lattice formulation addressing their strongly-coupled fixed points. These lattice models are also relevant in condensed matter, as they offer a neat playground to explore strong correlations in the quantum anomalous Hall (QAH) effect. We give a detailed description of our multidisciplinary approach to understand the fate of the QAH phases as the four-Fermi interactions are increased, which combines strong-coupling and effective-potential techniques, unveiling a rich phase diagram with large-*N* Chern insulators and Lorentz-breaking fermion condensates. Moreover, this toolbox can be enlarged with recent advances in quantum information science, as we show that tensor-network algorithms based on projected entangled pairs can be used to improve our understanding of the strong-coupling limit. We also present a detailed scheme that uses ultra-cold atoms in optical lattices with synthetic spin–orbit coupling to build quantum simulators of these four-Fermi models. This yields a promising alternative to characterize the

* Corresponding author.
E-mail address: albermud@ucm.es (A. Bermudez).

https://doi.org/10.1016/j.aop.2022.168763
0003-4916/© 2022 The Author(s). Published by Elsevier Inc. This is an open access article under the CC BY-NC-ND license (http://creativecommons.org/licenses/by-nc-nd/4.0/).

strongly-coupled fixed points and, moreover, could also explore real-time dynamics and finite-fermion densities.

© 2022 The Author(s). Published by Elsevier Inc. This is an open access article under the CC BY-NC-ND license (http://creativecommons.org/licenses/by-nc-nd/4.0/).

1. Introduction

One of the main tasks in condensed-matter physics is the prediction and classification of new phases of matter, understanding how they can transform into each other via phase transitions [1]. Symmetry has played a key role in this endeavour, [2,3], since the way in which it breaks can be used to understand many ordering patterns at the microscopic level. Despite decades of intense research, observing how different orderings arise from the same microscopic model, and how they can be described by emerging effective theories that cannot be predicted by simply looking at the individual microscopic constituents [4], is still a source of much fascination. This emergence is typically a consequence of the interplay of symmetry and strong inter-particle correlations, the latter being induced by interactions among the microscopic constituents. In condensed matter, these constituents typically correspond to the ions forming the crystal structure and the valence electrons, all of them interacting via Coulomb forces [5,6].

Narrow-band metals have turned out to be a particularly-rich playground for this emergence. Here, the Coulomb interaction between the electrons is screened, and can be approximated by a local four-Fermi term that leads to the Hubbard model, the archetype of strongly-correlated fermions in condensed matter [7]. The apparent simplicity of this model is deceptive, as it can host an interaction-induced metal–insulator transition at partial band fillings [8], which defies the naive band-theory distinction between insulators and conductors. In fact, in the half-filled case, these so-called Mott insulators display anti-ferromagnetic ordering as a consequence of magnetic super-exchange interactions and a phase transition where the spin rotational symmetry is spontaneous broken [9,10]. Moreover, as one dopes this Mott insulator away from half filling, the interplay of anti-ferromagnetism with the dynamics of the holes has been studied as a fully-electronic mechanism that may account for high-T_c superconductivity [11,12], as the mobility of holes can release the anti-ferromagnetic singlets, allowing them to condense into the superconductor.

Four-Fermi models have also played an important role at much higher energies, starting with the pioneering work of Enrico Fermi on β-decay in nuclei [13,14]; a precursor to the theory of electroweak interactions in the standard model of particle physics. Four-Fermi terms also appear in the so-called Nambu–Jona–Lasinio (NJL) models [15,16], introduced as a description of interactions between nucleons and predating the modern theory of the strong force in the quantum-chromodynamics (QCD) sector of the standard model. NJL models are nowadays considered as effective theories that capture essential properties of QCD, such as dynamical mass generation by the spontaneous breakdown of chiral symmetry [17]. Lowering the spacetime dimension, one finds the Gross–Neveu model in 1+1 dimensions [18], where the specific form of the Four-Fermi terms allows to study asymptotic freedom in a renormalizable framework, capturing in this way another essential feature of QCD. Note that, although all these four-Fermi models are defined by continuum quantum field theories (QFTs) of self-interacting Dirac fermions, one can always discretize spacetime in a lattice [19,20], which leads to lattice field theories (LFTs) that are closer in spirit to the aforementioned Hubbard models. These LFTs yield a non-perturbative approach to understand the strong-coupling nature of the fixed points governing the chiral-symmetry-breaking transitions [21], around which one can perform a long-wavelength approximation and connect to the QFTs [22].

This analogy between condensed matter and high-energy physics becomes more quantitative in the so-called *Dirac matter* including, as paradigmatic examples, graphene [23], Weyl semi-metals [24], and topological insulators and superconductors [25]. These materials have band structures that can be ultimately understood as specific lattice discretizations of Dirac-type Hamiltonian QFTs. The perspective, however, is rather different. Whereas the lattice is an artificial

scaffolding in LFTs, and the focus lies on the critical points around which one recovers the long-wavelength physics independent of lattice artifacts, the lattices of Dirac matter are physical and play a crucial role in determining the special properties of the phases. In the case of topological insulators and superconductors, these properties are a consequence of a different driving mechanism for the ordering of matter at the microscopic scale; a mechanism where topology and symmetry intertwine to determine the groundstate properties. Conceptually, topological phases of matter differ from those formed by spontaneous symmetry breaking (SSB), since they cannot be characterized in terms of local order parameters dictated by an underlying SSB process. Instead, the groundstates are characterized by quantized topological invariants, the values of which cannot change unless the energy gap to the lowest-lying excitations closes, and a quantum phase transition takes place [26]. Note that these so-called topological phase transitions do not require any symmetry breaking. On the contrary, it might actually be the preservation of certain symmetries [27–29], which determines the form of the topological invariant, and it becomes important to understand the robustness of these phases with respect to external perturbations. Besides their fundamental interest, these topological phenomena can lead to novel functionalities and promising technological applications [30].

The epitome of the aforementioned robustness to external perturbations, such as disorder, occurs in the quantum Hall effect [31]. Remarkably, this phase of matter has an underlying topological invariant [32] that corresponds to the first Chern number of a fibre bundle associated to the electronic band structure [33]. Moreover, this description is not limited to band theory, as the Chern numbers can be adiabatically connected to a many-body topological invariant when electron–electron interactions or disorder are switched on [34]. In fact, this invariant is responsible for the robust quantization of the transverse conductivity under generic weak perturbations that do not close the gap of the system. In this case, regardless of their symmetry properties, these perturbations cannot induce back-scattering in current-carrying edge states that propagate along the boundaries of the system [35,36], and can thus transport charge robustly even in the presence of an insulating gap. In this way, the naive band-theory distinction between insulators and conductors is again defied; only this time by the introduction of topology rather than correlations.

Coming back to the context of Dirac matter, the so-called Chern insulators [37–39] can feature the above quantum Hall effect even in absence of any external magnetic field, leading to what is currently known as the quantum anomalous Hall (QAH) effect [40]. In a seminal work [37], which stimulated subsequent contributions [41,42] that laid the foundations of topological insulators and superconductors [25,26], Haldane showed that a time-reversal-breaking discretization of the Dirac QFT on a honeycomb graphene-type lattice can support a non-zero Chern number that is related to the parity anomaly in $(2+1)$-dimensional quantum electrodynamics [43–46]. The associated transverse conductivity can again be associated with current-carrying edge states which circulate in a single direction along the boundaries of the system in spite of the absence of a net magnetic field.

From a LFT perspective, the continuum QFT that describes the Haldane model is that of a pair of Dirac fields with a different mass. Here, the doubling is related to a fundamental theorem for the lattice discretization of a Dirac field [47,48], whereas the mass difference is an instance of Wilson's prescription to deal with such a doubling [49]. The parallelism becomes clearer using a square-lattice discretization [38,39], sometimes refereed to as the Qi–Wu–Zhang model of the QAH effect. This model can be readily understood as a Hamiltonian formulation of LFTs [50], in which time remains continuous, and it is only the spatial coordinates that get discretized in a square lattice following Wilson's prescription [49]. From this perspective, the topological edge states that appear at the boundaries of these Chern insulators, and carry the transverse current in the QAH effect [38,39], can be understood as lower-dimensional versions of the so-called domain-wall fermions [51]. In this context, the aforementioned topological invariants also appear in other dimensions, and control a Chern–Simons-type response to additional external gauge fields [39,52,53]. We note that the QAH effect has been realized with thin films of semiconducting tetradymite compounds doped with magnetic atoms [54,55], as first proposed theoretically [56], or in layered compounds with intrinsic magnetic order [57]. More recently, the QAH effect has also been observed in magnetically-doped multi-layer systems, which have higher Chern numbers and display plateau-to-plateau topological phase transitions [58,59].

A fundamental question that has generated considerable interest in recent years is how topological insulators and superconductors get modified in the presence of interactions, ultimately seeking for new phases of matter driven by the interplay of symmetry, correlations and topology [60–63]. First of all, starting from initial studies [34], we note that topological invariants can be generalized to the many-body case [64,65], and formulated in terms of single-particle Green's functions that unveil the special role played by the self energy [66–70]. Additionally, there are entanglement-related quantities that give an alternative route to explore topology [71–73]. Equipped with these many-body tools for the characterization of topological phases, let us now briefly discuss some of the possible effects brought up by the inclusion of interactions. Due to the non-zero bulk gap, one expects that topological insulators will be generally robust to weak interactions. As first discussed in [42], electron–electron interactions can renormalize this bulk gap, and stabilize the topological phase further. In other situations, this renormalization of the band structure can even induce transitions from a trivial phase into a topological one [74,75]. Further interaction-induced effects can occur by means of SSB, as time-reversal symmetry can be spontaneously broken when the interactions increase, such that a new topological phase that cannot be understood from the renormalization of the free-particle parameters arises [76–78]. Note that SSB of unitary symmetries can also take place, leading to order parameters that coexist with non-zero topological invariants, leading to the concept of symmetry-breaking topological insulators induced by interactions [79–81]. A final possibility brought up by interactions is that new topological phases arise without any free-particle counterpart, such as topological Mott insulators [82] or fractional Chern insulators [83–85].

Despite this large body of theoretical work, the vast majority of materials that have been found to host topological phenomena in the absence of strong external magnetic fields, only display weak electron–electron interactions. A notable exception is bilayer graphene, either twisted at a specific magic angle [86–90], or misaligned with respect to a substrate [91]. Let us note, however, that the microscopic description of these materials differs markedly from the paradigmatic lattice models that have been thoroughly studied in the presence of Hubbard-type interactions [63], and where most of the interaction-induced effects discussed above have been identified. This also occurs for the experimental realizations of the QAH effect in thin-film materials [54,55,57,86], in which a Haldane-type model [38,39] serves as a guide to build a qualitative understanding, but where many of the microscopic details are clearly different [40]. Moreover, since the effective spinor degrees of freedom are related to bonding/anti-bonding states in the two opposite surfaces of the thin film, interactions will not be described by a simple contact Hubbard-type term.

Moving away from condensed matter into the realm of atomic, molecular and optical (AMO) physics, the microscopic tunability of gases of ultracold atoms trapped in optical lattices [92] allows one to face the quantum many-body problem from a different perspective, that of quantum simulations (QSs) [93–95]. The idea here is that one can control these dilute and highly non-relativistic gases of atoms, making them behave according to a specific model of interest at a widely-different scale. For instance, one may use these AMO quantum simulators to explore much denser systems in condensed matter, or much more energetic ones in particle physics. Although research on QSs focused for some time on condensed-matter models [96–99], applications to high-energy physics are becoming more popular in recent years [100–108]. The present context of topological Dirac matter actually touches both of these directions, as recent experiments with ultra-cold fermions in shaken optical lattices have allowed to realize Haldane's model for the first time [109]. In contrast to the previous condensed-matter realizations, where the archetype lattice models serve to build a qualitative understanding, the Haldane model is an accurate description of this AMO experiment and, moreover, one can control the fermion filling and microscopic parameters, and even modify the latter dynamically and measure real-time evolution.

Beyond the interest in observing interaction-induced effects in the QAH effect, we note that the related $(2+1)$-dimensional four-Fermi LFTs are typically controlled by strongly-coupled fixed points, the properties of which can only be accessed by non-perturbative methods, and are still a subject of active research [21,110,111]. One can thus exploit the interdisciplinary character of this field, and combine the different tools developed by these communities to advance our understanding further. For instance, in order to understand non-perturbative phenomena, one may employ a large-N expansion through which QFTs simplify significantly and become solvable in the limit of a large

number of flavours N [112]. Within this framework, it has been possible to predict some of the fundamental features of QCD in the simpler four-Fermi Gross–Neveu model in $1{+}1d$, including asymptotic freedom and dynamical symmetry breakdown [18]. The large-N expansion is also very important in four-Fermi models in $(2{+}1)$ dimensions, as it offers a renormalizable framework that contrast the situation of a perturbative approach. In this article, we shall exploit large-N tools to understand correlation effects in a QAH effect, and combine them with strong-coupling predictions based on the condensed-matter concept of super-exchange to understand the full phase diagram. Finally, exploiting the third facet, we give a detailed account of a cold-atom realization of the model for a single flavour based on a scheme for synthetic spin–orbit coupling.

From the perspective of the QS of a correlated QAH effect, the most direct route would be to explore a spinful version of the experiment with ultra-cold fermions in shaken honeycomb lattices [109]. In this case, the Hubbard interaction is directly implemented by the low-temperature scattering dominated by two-particle s-wave collisions [92], which can actually be tuned by additional Feshbach resonances [113]. However, the combination of Hubbard interactions with periodic shaking has been hampered, in several experimental realizations, by a larger heating mechanism due to a denser spectrum of excitations. Here, the atoms get excited by resonantly absorbing quanta from the periodic drive that shakes the lattice, a process that causes an effective heating [114–116]. In a recent manuscript [117], we have explored a different route to explore correlated QAH insulators and their connection to strongly-coupled four-Fermi QFTs. This alternative route considers Fermi gases with synthetic spin–orbit coupling [118–120] induced by a so-called Raman optical lattice [121,122], which has been recently demonstrated in experiments [123–126]. Although residual photon scattering from the Raman beams can also induce some heating, it should not be as severe as in the shaken optical lattice if sufficient laser power is available, allowing one to work at sufficiently large Raman detunings. In presence of interactions, correlated phenomena may need slower experimental time scales so this heating may again become a practical limitation. In this case, one may consider realizations based on alkaline-earth or lanthanide atoms, where it can be further minimized. Below, we describe this scheme in detail.

In this work, we start from a discretized anisotropic variant of a Gross–Neveu model with N flavours of Wilson fermion in $2{+}1$ dimensions. In contrast to common LFT approaches to the $(2{+}1)d$ Gross–Neveu model, we dispense with the notion of chirality from the outset by restricting our attention to two-component spinors instead of the four-component ones that permit a definition of a non-trivial γ^5 matrix [21,110]. Since chiral symmetry and its breakdown is a fundamental ingredient of Gross–Neveu-type models, but is lacking in our case, we prefer to refer to the current discretization as a *four-Fermi–Wilson model*. In the single-flavour limit, this lattice model has a neat connection to a spin–orbit-coupled Hubbard model, bringing a direct connection to the aforementioned QSs of spin–orbit-coupled Fermi gases in optical lattices. Although the large-N approximation is only exact in the limit $N \to \infty$, we provide a detailed analysis that shows that our large-N calculations predict the same structure of the phase diagram as the $N = 1$ limit, which can be explored using a super-exchange strong-coupling approach and various variational ansätze.

This article is organized as follows. In Section 2, we introduce our four-Fermi–Wilson model, and describe the topological properties of the non-interacting limit, showing that the model can host N-flavoured Chern insulators and allow for various topological phase transitions as the microscopic bare parameters are modified. In Section 3, we explore the opposite limit of very strong four-Fermi interactions and a single fermion flavour $N = 1$, which we approach by deriving an effective Hamiltonian using the concept of super-exchange interactions. We show that this effective model corresponds to a quantum compass model, where symmetry-breaking orbital ferromagnets can be identified using a variational mean-field method, and in the framework of tensor networks using projected entangled pairs (PEPs). In Section 4, we derive and solve the large-N gap equations, both in continuous time and discretized time, showing that the aforementioned orbital ferromagnets can be interpreted as fermion condensates that spontaneously break a $\mathbb{Z}_2$ inversion symmetry and forbid recovering a QFT invariant under Lorentz boosts in the continuum limit. We discuss how an additive renormalization and a suitable re-scaling must be considered in order connect both continuum and discrete-time approaches. In Section 5, we use the discrete-time approach to obtain an effective potential, which allows us to explore not only the symmetry-broken condensates, but

also to delimit the topological QAH phase at intermediate interactions. Using the large-N self-energy in the symmetry-preserved region, we show that this QAH regions are characterized by large-N Chern insulators that display a non-zero value of a non-perturbative many-body topological invariant. We also discuss how the effective potential allows for a neat account of first- or second-order nature that separate these phases from the Lorentz-breaking condensates. Finally, in Section 6, an experimental scheme for the QS of the single-favour four-Fermi–Wilson model with ultracold atoms in optical lattices is presented, where we also discuss in detail how the available measurement protocols could be used to explore this model in the laboratory.

2. Four-Fermi–Wilson model in 2+1 dimensions

2.1. Chiral and non-chiral four-Fermi field theories in 2+1 dimensions

The original Gross–Neveu model is a chiral-invariant QFT describing N flavours of massless Dirac fermions, which live in one spatial and one time dimension, and interact via four-Fermi terms [18]. This model gained considerable attention in the early days of QCD, since it is a renormalizable field theory that shares important features with QCD such as asymptotic freedom, chiral symmetry breaking by dynamical mass generation, and dimensional transmutation, all of which can be explored in a much simpler setup. In a Hamiltonian field-theory formulation, this model can be easily extended to 2+1 dimensions, where the Hamiltonian density $\mathscr{H}(\boldsymbol{x})$ corresponding to the Hamiltonian $H = \int \mathrm{d}^2x :\mathscr{H}(\boldsymbol{x}):$ reads

$$\mathscr{H} = -\sum_{f=1}^{N} \overline{\psi}_{\mathsf{f}}(\boldsymbol{x})(\mathrm{i}\gamma^j\partial_j)\psi_{\mathsf{f}}(\boldsymbol{x}) - \frac{g^2}{2N}\left(\sum_{\mathsf{f}=1}^{N} \overline{\psi}_{\mathsf{f}}(\boldsymbol{x})\psi_{\mathsf{f}}(\boldsymbol{x})\right)^2, \tag{1}$$

where the repeated-index summation only runs over the spatial indexes $j \in \{1, 2\}$. Here, we have introduced the field operators $\psi_f(\boldsymbol{x})$, which annihilate a fermion of a given flavour $\mathsf{f} \in \{1, 2, \ldots, N\}$ at a specific spatial location $\boldsymbol{x} = (x, y)^t$, and the corresponding adjoints $\overline{\psi}_{\mathsf{f}}(\boldsymbol{x}) = \psi_{\mathsf{f}}^\dagger(\boldsymbol{x})\gamma_0$, which are defined in terms of the analogous creation operators $\psi_{\mathsf{f}}^\dagger(\boldsymbol{x})$. While the first term in Eq. (1) describes the kinetic energy of N massless Dirac fermions, the second one represents the four-Fermi term responsible for intra- and inter-flavour interactions. Note that, in contrast to the (1+1)-dimensional case [18], the coupling strength g^2 is not dimensionless, but has units of inverse mass $[g^2] = \mathsf{M}^{-1}$ when considering natural units $\hbar = c = 1$. By power counting, the four-Fermi term is no longer marginal as in (1+1) dimensions [18], but becomes irrelevant thus forbidding a perturbative renormalization. Remarkably, a large-N expansion provides such a renormalizable framework, and one can explore the nature of the strongly-coupled fixed point to different orders of $\mathscr{O}(1/N^\alpha)$ [110].

In order to guarantee Lorentz invariance, the above Hamiltonian is expressed in terms of gamma matrices γ^μ, such that fermionic fields become spinors with well-defined transformations under the Lorentz group. These matrices must satisfy Clifford's algebra $\{\gamma^\mu, \gamma^\nu\} = 2\eta^{\mu\nu}$, where $\eta = \mathrm{diag}(1, -1, -1)$ is Minkowski's metric, and the spacetime indexes for a (2+1)-dimensional spacetime are $\mu, \nu \in \{0, 1, 2\}$. In 2+1 dimensions, there are two possible strategies to satisfy this algebra. The simplest one is to choose a set of adapted Pauli matrices, such as

$$\gamma^0 = \sigma^z, \quad \gamma^1 = \mathrm{i}\sigma^y, \quad \gamma^2 = -\mathrm{i}\sigma^x, \tag{2}$$

which leads to two-component spinor fields for each of the flavours $\psi_{\mathsf{f}}(\boldsymbol{x}) = (\psi_{\mathsf{f},1}(\boldsymbol{x}), \psi_{\mathsf{f},2}(\boldsymbol{x}))^{\mathrm{t}}$. The would-be chiral gamma matrix, which must be Hermitian and anti-commute with the rest, is typically defined as $\gamma^5 = \mathrm{i}\gamma^0\gamma^1\gamma^2$, which can be easily checked to be trivial in this case $\gamma^5 = \mathbb{I}_2$. Accordingly, it does not satisfy the anti-commutation requirement $\{\gamma_5, \gamma_\mu\} = 0$, and one speaks of the absence of chirality. This is actually a generic feature in all odd spacetime dimensions with an irreducible representation of gamma matrices, as one already exhausts all possibilities with the gamma matrices assigned to the spacetime indexes. An alternative is to consider higher-dimensional representations of the gamma matrices, such as

$$\gamma^0 = \sigma^z \otimes \sigma^z, \quad \gamma^1 = \mathbb{I}_2 \otimes (\mathrm{i}\sigma^y), \quad \gamma^2 = \mathbb{I}_2 \otimes (-\mathrm{i}\sigma^x), \tag{3}$$

for $(2+1)$ dimensions. This representation allows for a pair of choices $\gamma^5 \in \{\sigma^x \otimes \sigma^z, \sigma^y \otimes \sigma^z\}$ fulfilling the Hermiticity and anti-commutation constraints. For either choice, the four-Fermi QFT (1) is invariant under a discrete axial rotation

$$\psi_{\mathrm{f}}(x) \mapsto \mathrm{e}^{\mathrm{i}\frac{\pi}{2}\gamma^5}\psi_{\mathrm{f}}(x) = \mathrm{i}\gamma^5\psi_{\mathrm{f}}(x), \tag{4}$$

and one speaks of a discrete chiral symmetry that prevents the fermions from having a mass [21, 110]. In this work, however, we stick to the lowest-dimensional representation (2), and thus dispense with the notion of chirality and axial rotations from the outset. As discussed below, however, there will still be remnants of dynamical mass generation and strongly-coupled phenomena, although one cannot relate them to chiral symmetry breaking. We note that our model exhibits a global $U(N)$ flavour symmetry, which becomes apparent by expressing the fields as a vector $\Psi(\boldsymbol{x}) = (\psi_1(\boldsymbol{x}), \ldots, \psi_N(\boldsymbol{x}))^t$ and applying the transformation $\Psi(\boldsymbol{x}) \mapsto (u \otimes \mathbb{I}_2)\Psi(\boldsymbol{x})$ on both components of the N-flavoured Dirac spinors, where $u \in U(N)$.

2.2. Wilson-type discretizations of four-Fermi field theories and Hubbard bilayers

Let us now describe the lattice scheme chosen to regularize the QFT (1). First, spatial coordinates are discretized by introducing an anisotropic lattice spacing, leading to a simple rectangular Bravais lattice described by

$$\Lambda_s = \{n_1 a_1 \boldsymbol{e}_1 + n_2 a_2 \boldsymbol{e}_2 : \ \boldsymbol{n} = (n_1, n_2) \in \mathbb{Z}_{N_1} \times \mathbb{Z}_{N_2}\}. \tag{5}$$

This lattice is determined by the lattice spacings a_1, a_2, the unit vectors $\boldsymbol{e}_1, \boldsymbol{e}_2$, the number of columns (rows) N_1 (N_2) along the x- and y-directions, and the corresponding spatial area $A_s = \prod_j N_j a_j$. In the Hamiltonian version [127] of the naive-fermion prescription [20], the Hamiltonian density $\mathscr{H}_N(\boldsymbol{x})$ in vector representation includes the following tunnelling processes in the spatial lattice

$$\mathscr{H}_N(\boldsymbol{x}) = -\sum_j \left(\overline{\Psi}(\boldsymbol{x}) \frac{\mathrm{i}(\mathbb{I}_N \otimes \gamma^j)}{2a_j} \Psi(\boldsymbol{x} + a_j \boldsymbol{e}_j) + \mathrm{H.c.} \right), \tag{6}$$

which follow from the substitution of the spatial derivatives by forward finite differences. The corresponding Hamiltonian is given by $H_N = a_1 a_2 \sum_{\boldsymbol{x} \in \Lambda_s} :\mathscr{H}_N(\boldsymbol{x}):$, where the integrals have been replaced by sums. We note that the lattice anisotropy $a_1 \neq a_2$ should not lead to an anisotropic speed of light, such that Lorentz invariance will still be recovered in the continuum limit. Note that, from a condensed-matter perspective, the discretization anisotropy translates into anisotropic nearest-neighbour tunnellings (6), and has thus a natural microscopic interpretation. As discussed at length in the following sections, this anisotropy will play an important role in the correlation effects of a QAH effect.

As is well-known in LFT [47,48], this naive-fermion approach gives rise to additional Dirac fermions in the continuum limit, known as fermion doublers, which actually appear as long-wavelength excitations around the boundaries of the Brillouin zone. As advanced in the introduction, we consider Wilson's prescription [49] to deal with the doublers, which can be sent to the UV-cutoff by introducing an additional mass term that is proportional to the inverse lattice spacings $1/a_j$. This is achieved through the following Wilson term

$$\mathscr{H}_W(\boldsymbol{x}) = \sum_j \left(\overline{\Psi}(\boldsymbol{x}) \frac{r_j}{2a_j} \big(\Psi(\boldsymbol{x}) - \Psi(\boldsymbol{x} + a_j \boldsymbol{e}_j) \big) + \mathrm{H.c.} \right) \tag{7}$$

where r_j is an anisotropic version the dimensionless Wilson parameter. This term is usually supplemented by an additional bare mass m via

$$\mathscr{H}_M(\boldsymbol{x}) = m\, \overline{\Psi}(\boldsymbol{x}) \Psi(\boldsymbol{x}). \tag{8}$$

The Wilson term (7) stems from the finite-difference discretization of a second-derivative on the fields, which would be an irrelevant perturbation in the continuum QFT. Accordingly, one may

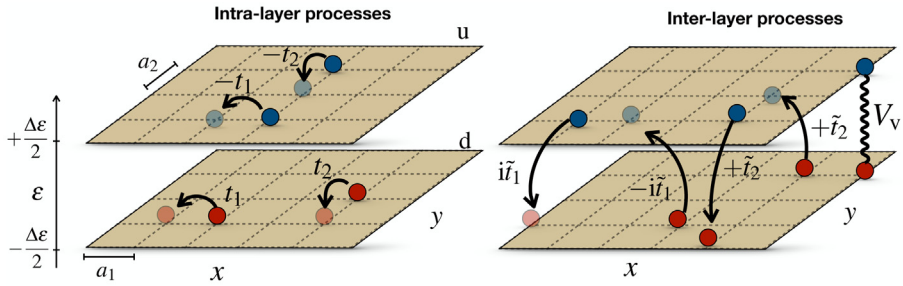

Fig. 1. Hubbard bilayer for the single-flavour four-Fermi–Wilson model: Visualization of hopping and interaction terms in the 2+1 dimensional Hamiltonian field theory of Eq. (10) for $N = 1$. The two-component Dirac spinor $\psi_f(\boldsymbol{x}) = (\psi_{f,1}(\boldsymbol{x}), \psi_{f,2}(\boldsymbol{x}))^t$ can be mapped onto fermionic operators for the up/down layers $c_{\boldsymbol{n},u}, c_{\boldsymbol{n},d}$. On the left panel, the intra-layer terms t_1, t_2 describe the tunnelling of fermions along the x and y directions of the rectangular lattice (3), such that the different signs of the tunnelling strengths allow one to implement the Wilson term (7). For our choice of gamma matrices, the bare mass (8) corresponds to an energy imbalance $\pm\Delta\epsilon/2$ between the two layers. On the right panel, we depict the inter-layer terms $\tilde{t}_1, \tilde{t}_2$ corresponding to the tunnelling of fermions along the x and y directions with the simultaneous change of layer. Finally, the four-Fermi term (9) can be described as an inter-layer Hubbard interaction of strength V_v along the vertical direction. The correspondence of the microscopic parameters is derived in Section 3.

expect that the doublers shall not influence the universal low-energy properties in the continuum limit, which can be recovered around certain critical points of the lattice model. Let us emphasize, however, that this expectation can be a drastic oversimplification, especially in the presence of additional four-Fermi terms

$$\mathscr{V}_g(\boldsymbol{x}) = -\frac{g^2}{2N}\left(\overline{\Psi}(\boldsymbol{x})\Psi(\boldsymbol{x})\right)^2 . \tag{9}$$

As already noted in the introduction, the critical points of the Wilson-discretized model can actually separate topological from trivial phases, where the relative signs of the doubler masses play a crucial role. Such phases have widely different low-energy behaviours, as is the case of the QAH effect. This phase of matter can support a non-zero topological invariant [39,52,53], and a transverse current in spite of the bulk gap [37–39], which is carried by mid-gap current-carrying edge states that may be understood as (1+1)-dimensional versions of domain-wall fermions [51]. In fact, from this perspective [128–135], topological insulators in different symmetry classes and dimensions [136] correspond to lower-dimensional versions of these domain-wall fermions [51] with different representations of the Clifford algebra. In the trivial phase, on the other hand, these edge states are absent, and the long-wavelength description of the model is that of a trivially gapped phase. These differences can be formalized quantitatively in the presence of interactions by means of the renormalization group [137,138], as explicitly shown for lower-dimensional instances in [133]. The other possibility, also found in lower-dimensional models [130,131], is that the interplay of interactions and topology leads to critical lines in the phase diagram that contain continuum QFTs defining different universality classes.

The full Hamiltonian of the four-Fermi–Wilson model [117] can be defined by summing up the four terms defined above

$$H = a_1 a_2 \sum_{\boldsymbol{x}\in\Lambda_s} :\mathscr{H}_N(\boldsymbol{x}) + \mathscr{H}_W(\boldsymbol{x}) + \mathscr{H}_M(\boldsymbol{x}) + \mathscr{V}_g(\boldsymbol{x}): . \tag{10}$$

As displayed in Fig. 1 for the single-flavour limit $N = 1$, and discussed in more detail in the following section, the discretized model can be regarded as a bilayer model, where the upper (lower) plane belongs to the first (second) component of the Dirac spinor. Within this picture, and in light of our choice of gamma matrices (2), the first contribution (6) describes inter-layer tunnellings. The Wilson term (7) contributes to intra-layer tunnellings of opposite strengths for each of the layers and, together with the bare mass (8), determines the energy imbalance between the upper and

lower layers. Finally, the four-Fermi coupling (9) is depicted as spring that describes the interactions of two fermions that occupy simultaneously the same site of the upper and lower layers, and can be seen to correspond to a Hubbard-type density–density interaction.

This representation can be interpreted as a (2+1)-dimensional generalization of Creutz's cross-link ladder [139], a paradigmatic model of topological insulators in the AIII class that has been the subject of intensive studies in recent years [130,140–147]. If we now introduce more flavours $N > 1$, the picture would be that of stacked bilayers that get coupled among each other via the four-Fermi term. This perspective can be understood in light of the synthetic dimensions [148,149], and will offer valuable insight when exploring the phase diagram of the model in the strong-coupling limit. Let us note, however, that we can interpret this model as a Fermi–Hubbard model with a generalized spin–orbit coupling, which also yields valuable insight as it underlies the proposal for the QS cold-atom scheme, briefly presented in [117], and described in detail below.

2.3. N-flavoured Chern insulators and the quantum anomalous Hall effect

Due to the discrete translation symmetry introduced by the lattice (5), it is natural to Fourier transform the fields

$$\Psi(\boldsymbol{x}) = \frac{1}{\sqrt{A_s}} \sum_{\boldsymbol{k}\in \mathrm{BZ}} \mathrm{e}^{\mathrm{i}\boldsymbol{k}\cdot\boldsymbol{x}} \Psi(\boldsymbol{k}) \tag{11}$$

where the momenta $\boldsymbol{k} = (k_1, k_2)^t$ are restricted to the first Brillouin zone $\mathrm{BZ} = \{k_j = -\pi/a_j + 2\pi n_j/N_j a_j : \ n_j \in \mathbb{Z}_{N_j}, \ j \in \{1, 2\}\}$, and we assume periodic boundary conditions such that the BZ is a 2-torus. After this Fourier transform, and in the absence of the four-Fermi term (9), the quadratic free Hamiltonian obtained by restricting the sum in Eq. (10) to the naive, Wilson and bare mass terms, can be rewritten as

$$H_F = \sum_{\boldsymbol{k}\in \mathrm{BZ}} \Psi^\dagger(\boldsymbol{k}) h_{\boldsymbol{k}}(m) \Psi(\boldsymbol{k}). \tag{12}$$

Here, the single-particle Hamiltonian reads

$$h_{\boldsymbol{k}}(m) = \boldsymbol{d}_{\boldsymbol{k}}(m) \cdot (\mathbb{I}_N \otimes \boldsymbol{\sigma}), \tag{13}$$

where we have introduced the vector of Pauli matrices $\boldsymbol{\sigma}$, and the following mapping of the BZ to a real vector

$$\boldsymbol{d}_{\boldsymbol{k}}(m) = \left(\frac{\sin(k_1 a_1)}{a_1}, \frac{\sin(k_2 a_2)}{a_2}, m + \sum_j \frac{r_j}{a_j} \Big(1 - \cos(k_j a_j) \Big) \right). \tag{14}$$

This can be readily diagonalized yielding $2N$ energy bands, a pair $\epsilon_\pm(\boldsymbol{k}) = \pm\epsilon(\boldsymbol{k}) = \pm \parallel \boldsymbol{d}_{\boldsymbol{k}}(m) \parallel$ for each flavour. These bands display a relativistic dispersion at small momenta $\delta k_j \ll 1/a_j$, namely $\epsilon(\delta\boldsymbol{k}) \approx (\delta\boldsymbol{k}^2 + m^2)^{1/2}$, where we find an effective speed of light $c = 1$ in accordance with natural units and the emergence of Lorentz invariance. Note that there are additional points in $\boldsymbol{k}$-space, $\boldsymbol{K}_{\boldsymbol{n}_d} = (\pi n_{d,1}/a_1, \pi n_{d,2}/a_2)$ for $\boldsymbol{n}_d = (n_{d,1}, n_{d,2}) \in \{0, 1\} \times \{0, 1\}$, around which the energy dispersion corresponds again to that of a continuum Dirac equation with a non-zero mass. These fermion doublers can thus be described by a collection of Dirac spinors $\{\Psi_{\boldsymbol{n}_d}(\boldsymbol{x})\}_{\boldsymbol{n}_d}$ with N flavours, which are governed by the following long-wavelength quantum field theory in the free case

$$H_F = \int \mathrm{d}^2 x \sum_{\boldsymbol{n}_d} \overline{\Psi}_{\boldsymbol{n}_d}(\boldsymbol{x}) \left(-\mathrm{i} \big(\mathbb{I}_N \otimes \gamma^j_{\boldsymbol{n}_d} \big) \partial_j + m_{\boldsymbol{n}_d} \right) \Psi_{\boldsymbol{n}_d}(\boldsymbol{x}). \tag{15}$$

Here, depending on the particular doubler, the corresponding representation of the gamma matrices may involve different signs with respect to that of the original QFT (2), namely

$$\gamma^0_{\boldsymbol{n}_d} = \gamma^0, \quad \gamma^1_{\boldsymbol{n}_d} = (-1)^{n_{d,1}} \gamma^1, \quad \gamma^2_{\boldsymbol{n}_d} = (-1)^{n_{d,2}} \gamma^2. \tag{16}$$

Likewise, the effective mass depends on the particular doubler, and is usually referred to as a Wilson mass

$$m_{\boldsymbol{n}_d} = m + \frac{2r_1}{a_1} n_{d,1} + \frac{2r_2}{a_2} n_{d,2}. \tag{17}$$

We thus see that, in addition to the Dirac fermion of mass $m_{(0,0)} = m$ around the centre of the Brillouin zone, the so-called Γ point for $\boldsymbol{n}_d = (0, 0)$; there are three additional fermions at high-symmetry points, such as the corner R for $\boldsymbol{n}_d = (1, 1)$, and the edge centres M for $\boldsymbol{n}_d \in \{(1, 0), (0, 1)\}$, which have Wilson masses that scale with the inverse lattice spacings. If the bare mass is small enough $ma_j \ll 1$, and one takes the continuum limit $a_j \to 0$, these doublers become infinitely heavy and are naively expected to decouple from the universal long-wavelength physics. Note, however, that the bare mass is simply a lattice parameter and could also take large negative values $ma_j \approx -2r_j$, such that some of the Wilson masses (17) flip their sign. This connects to the band-inversion that leads to topological insulators [25,26], and is responsible for the non-zero quantization of the transverse conductivity in the QAH effect [37–39].

In the non-interacting regime, the Thouless–Kohmoto–Nightingale–den–Nijs formula [32] provides a direct link of such a transverse conductivity σ_{xy} with the Chern numbers $\{N_{\mathrm{Ch,b}}\}$ that characterize the band structure. Mathematically [33], these correspond to the topological invariants associated to the fibre sub-bundles for each occupied energy band. In the present context, N bands get fully occupied in the half-filled groundstate, such that the transverse conductivity reads

$$\sigma_{xy} = \frac{e^2}{2\pi\hbar} N_{\mathrm{Ch}}, \quad N_{\mathrm{Ch}} = \sum_{\mathrm{b}=1}^{N} N_{\mathrm{Ch,b}}. \tag{18}$$

These Chern numbers turn out to be proportional to the Berry phase γ_{b} defined as the integral of the Berry curvature in momentum space $\mathscr{F}^{ij}_{\mathrm{b}}(\boldsymbol{k}) = \partial_{k_i}\mathscr{A}^{j}_{\mathrm{b}}(\boldsymbol{k}) - \partial_{k_j}\mathscr{A}^{i}_{\mathrm{b}}(\boldsymbol{k})$, where $\mathscr{A}_{\mathrm{b}}(\boldsymbol{k}) = \langle\epsilon_{\mathrm{b}}(\boldsymbol{k})|\mathrm{i}\nabla_{\boldsymbol{k}}|\epsilon_{\mathrm{b}}(\boldsymbol{k})\rangle$ is the Berry connection [150]. In the present context, and considering periodic boundary conditions to explore the bulk band structure, the Brillouin zone corresponds to a toroidal manifold acting as the base space of the principal $U(1)$ bundle associated to the eigenstates where the Chern invariants are defined

$$N_{\mathrm{Ch,b}} = -\frac{1}{2\pi}\gamma_{\mathrm{b}} = -\frac{1}{4\pi}\int_{\mathrm{BZ}} dk_i \wedge dk_j\, \mathscr{F}^{ij}_{\mathrm{b}}(\boldsymbol{k}). \tag{19}$$

As neatly discussed in [151], this topological invariant can be rewritten as the Pontryagin index, the winding number of the mapping between the momentum-space 2-torus and the unit 2-sphere $\hat{\boldsymbol{d}} : \mathbb{T}^2 \to \mathbb{S}^2$, given by the unitary vector field $\hat{\boldsymbol{d}}_{\boldsymbol{k}}(m) = \boldsymbol{d}_{\boldsymbol{k}}(m)/\| \boldsymbol{d}_{\boldsymbol{k}}(m) \|$ obtained by normalizing Eq. (14). This winding number counts how many times the mapping wraps around the unit sphere, and yields

$$N_{\mathrm{Ch,b}} = \frac{1}{4\pi}\int_{\mathrm{BZ}} \mathrm{d}^2k\, \hat{\boldsymbol{d}}_{\boldsymbol{k}}(m) \cdot (\partial_{k_1}\hat{\boldsymbol{d}}_{\boldsymbol{k}}(m) \wedge \partial_{k_2}\hat{\boldsymbol{d}}_{\boldsymbol{k}}(m)). \tag{20}$$

As one can numerically check, this integral can be accurately evaluated using the long-wavelength approximation (15). Each of the N-flavour massive Dirac fermions, including the doublers, may be considered as a monopole for the Berry curvature with a non-zero contribution to the winding number

$$N_{\mathrm{Ch}} = \frac{N}{2}\sum_{\boldsymbol{n}_d} (-1)^{(n_{d,1}+n_{d,2})}\mathrm{sign}(m_{\boldsymbol{n}_d}). \tag{21}$$

Assuming that the Wilson parameters are $r_j = 1$, the lattice constants are $a_1 \leq a_2$, and introducing their anisotropy ratio

$$\xi_2 = \frac{a_1}{a_2} \tag{22}$$

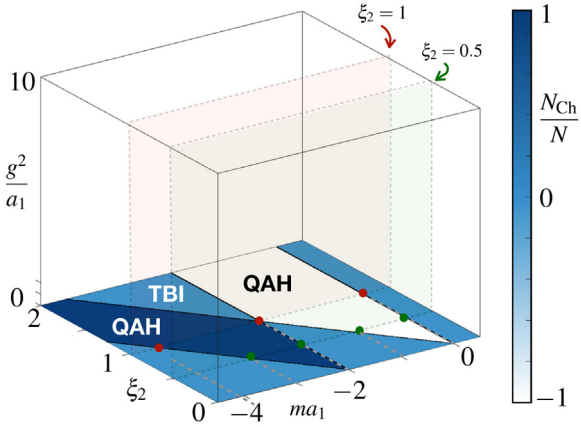

Fig. 2. Phase diagram and non-interacting QAH phases: We define parameter space as $\{ma_1, \xi_2, g^2/2a_1\}$, such that the free-fermion case $g^2 = 0$ corresponds to the base plane where one can depict the Chern numbers (21) in a contour plot. In this limit, one finds quantum anomalous Hall (QAH) and trivial band insulating (TBI) phases separated by topological quantum phase transitions. For spatial anisotropy $\xi_2 = \frac{1}{2}$, there are four critical points which, according to Eq. (23), lie at $ma_1 \in \{-3, -2, -1, 0\}$ and are marked with green dots in the figure where the Wilson mass (17) of a single fermion gets inverted by changing m. In the isotropic case $\xi_2 = 1$, there are only three critical points depicted by red dots. The central one at $ma_1 = -2$ marks the mass inversion of a couple of fermions, and thus connects two different QAH phases with edge currents circulating in opposite directions. In the sections below, we shall explore the vertical direction as $g^2 > 0$ along the two planes $\xi_2 \in \{\frac{1}{2}, 1\}$ shaded green/red. (For interpretation of the references to colour in this figure legend, the reader is referred to the web version of this article.)

fulfilling $\xi_2 < 1$, we find that the Chern numbers are

$$N_{\mathrm{Ch}} = \begin{cases} 0, & \text{if } \ 0 < ma_1, \\ -N, & \text{if } \ -2\xi_2 < ma_1 < 0, \\ 0, & \text{if } \ -2 < ma_1 < -2, \\ +N, & \text{if } \ -2(1+\xi_2) < ma_1 < -2\xi_2, \\ 0, & \text{if } \ ma_1 < -2(1+\xi_2). \end{cases} \tag{23}$$

As advanced previously, as the bare mass takes negative values proportional to the inverse lattice spacings, the groundstate of the system can support a non-zero Chern number (23), and thus transport current transversally (18). We shall refer to these states as N-flavoured Chern insulators. The specific values of the dimensionless parameter $-ma_1$ where the Chern number undergoes an abrupt change are associated with the closure of the energy gap and, thus, to a second-order quantum phase transition that cannot be characterized by an order parameter or any spontaneous symmetry breaking. On the contrary, there is an observable (18) that displays robust quantized values depending on an underlying topological invariant (21) that changes across these critical points and leads to a topological quantum phase transition (TQPT). Each of the TQPTs in Eq. (23) is marked by the mass inversion of one of the emerging Dirac fermions (15). Only when the number of negative Wilson masses (17) is odd, does the groundstate lead to a Chern insulator with a non-zero transverse conductivity.

For instance, in the single-flavour case, there are topological phases with $N_{\mathrm{Ch}} \in \{1, -1\}$ characterized by either 1 or 3 Dirac fermions with a negative Wilson mass, respectively. As depicted in Fig. 2, for spatial anisotropies $\xi_2 \neq 1$, these Chern insulators are separated in parameter space by an intermediate trivial phase with $N_{\mathrm{Ch}} = 0$, which is characterized by the same number of Dirac fermions with negative and positive Wilson masses. In the isotropic limit $a_1 = a_2$, the Wilson masses at the edge centres M of the Brillouin zone become degenerate $m_{(1,0)} = m_{(0,1)}$, such that there is no intermediate trivial phase separating the two QAH phases with $N_{\mathrm{Ch}} = \pm 1$. We note that the regime of opposite anisotropy $\xi_2 > 1$ has a completely analogous description (23), where one must

only exchange $a_1 \leftrightarrow a_2$ in the expressions above. Also, although we have set $r_j = 1$, we note that different values of the Wilson parameters would simply lead to rescalings of the bare mass axis to $ma_1 \to ma_1/r_1$, and the spatial anisotropy $\xi_2 \to \xi_2 r_2/r_1$, without changing the overall structure of the phase diagram. In the following, we will set $r_j = 1$. The question to be answered below is to what extent these topological phases survive for substantial non-zero interactions $g^2 > 0$, as one explores the parameter space in the vertical direction of Fig. 2.

3. Strong couplings and orbital magnetism

In this section, we explore the strong-coupling limit where the four-Fermi term (9) dominates. We note that, as discussed below Eq. (1), the four-Fermi coupling strength g^2 is not dimensionless, as for the Gross–Neveu model in (1+1) dimensions where dynamical mass generation yields an example of dimensional transmutation [18]. In $(2+1)$ dimensions, the coupling strength has units of inverse mass, and we can define the strong-coupling regime of the four-Fermi–Wilson model by letting the bare parameters $g^2/a_j \gg 1$, $\forall j$.

3.1. Super-exchange and quantum compass models

Let us start by discussing the single-flavour limit $N = 1$. To find the explicit connection with the Hubbard bilayer depicted in Fig. 1, let us note that the lattice field operators in Eq. (11) have dimensions of mass, and can be thus rescaled to define the upper- and lower-layer $\ell \in \{\mathrm{u}, \mathrm{d}\}$ fermionic operators

$$c_{\boldsymbol{n},\mathrm{u}} = \sqrt{a_1 a_2}\psi_1(\boldsymbol{x}), \quad c_{\boldsymbol{n},\mathrm{d}} = \sqrt{a_1 a_2}\psi_2(\boldsymbol{x}), \tag{24}$$

for the anisotropic rectangular lattice (5). These operators satisfy the standard anti-commutation relations used in condensed matter $\{c_{\boldsymbol{n},\ell}, c^\dagger_{\boldsymbol{n}',\ell'}\} = \delta_{\ell,\ell'}\delta_{\boldsymbol{n},\boldsymbol{n}'}$. This rescaling leads directly to the following free Hamiltonian

$$\begin{aligned} H_F = &-\sum_{\boldsymbol{n},j}\left(t_j\left(c^\dagger_{\boldsymbol{n},\mathrm{u}}c_{\boldsymbol{n}+\mathbf{e}_j,\mathrm{u}} - c^\dagger_{\boldsymbol{n},\mathrm{d}}c_{\boldsymbol{n}+\mathbf{e}_j,\mathrm{d}}\right) + \mathrm{H.c.}\right) \\ &-\sum_{\boldsymbol{n},j}\left(\mathrm{i}^j\tilde{t}_j\left(c^\dagger_{\boldsymbol{n},\mathrm{u}}c_{\boldsymbol{n}+\mathbf{e}_j,\mathrm{d}} + (-1)^j c^\dagger_{\boldsymbol{n},\mathrm{d}}c_{\boldsymbol{n}+\mathbf{e}_j,\mathrm{u}}\right) + \mathrm{H.c.}\right) \\ &+\sum_{\boldsymbol{n},j}\frac{\Delta\epsilon}{2}\left(c^\dagger_{\boldsymbol{n},\mathrm{u}}c_{\boldsymbol{n},\mathrm{u}} - c^\dagger_{\boldsymbol{n},\mathrm{d}}c_{\boldsymbol{n},\mathrm{d}}\right), \end{aligned} \tag{25}$$

where we recall that $j = 1, 2$. Here, we have introduced the intra- t_j and inter-layer $\tilde{t}_j$ tunnellings along the jth axis in the first two lines, depicted by black arrows in Fig. 1

$$t_1 = \frac{1}{2a_1}, \quad t_2 = \frac{1}{2a_2}, \quad \tilde{t}_1 = \frac{1}{2a_1}, \quad \tilde{t}_2 = \frac{1}{2a_2}. \tag{26}$$

The third line of the above Hamiltonian contains an energy imbalance $\Delta\epsilon$ between the layers, which is depicted by the energy scale in Fig. 1, and corresponds to

$$\frac{\Delta\epsilon}{2} = m + \frac{1}{a_1} + \frac{1}{a_2}. \tag{27}$$

In addition, up to irrelevant quadratic terms that only contribute with a constant shift of the energies for a fixed number of particles, the single-flavour four-Fermi term (9) can be rewritten as a density–density Hubbard interaction between the two layers

$$V_g = \sum_{\boldsymbol{n}} V_{\mathrm{v}} c^\dagger_{\boldsymbol{n},\mathrm{u}}c_{\boldsymbol{n},\mathrm{u}}c^\dagger_{\boldsymbol{n},\mathrm{d}}c_{\boldsymbol{n},\mathrm{d}}, \tag{28}$$

where the Hubbard interaction strength is repulsive

$$V_{\mathrm{v}} = \frac{g^2}{a_1 a_2}. \tag{29}$$

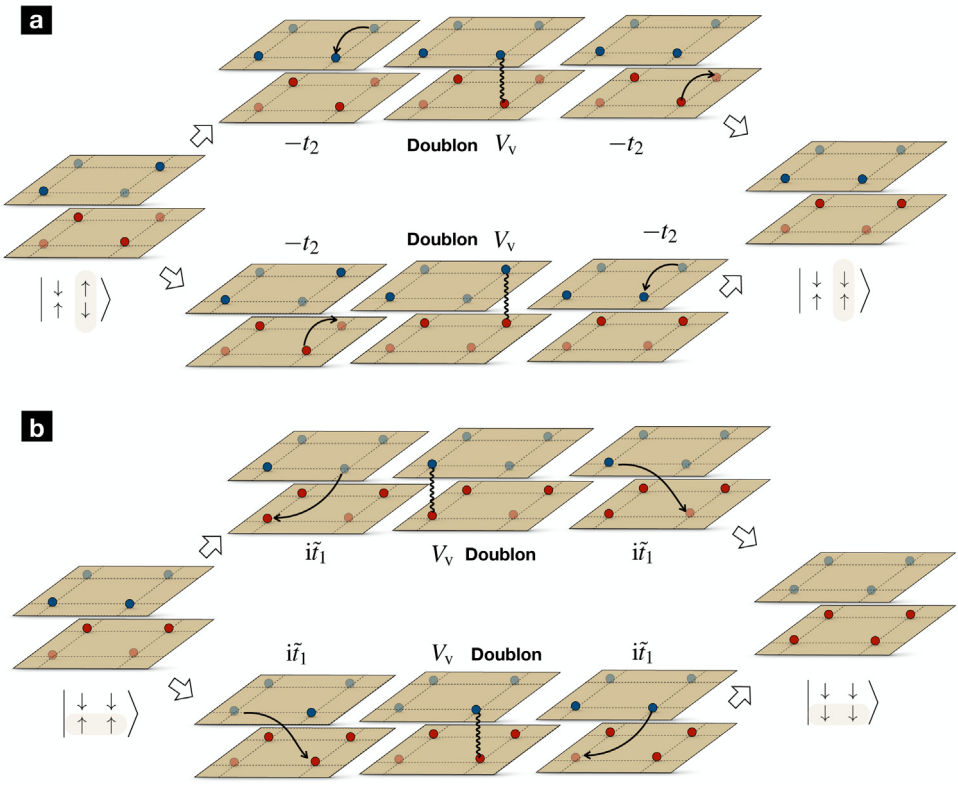

Fig. 3. Super-exchange processes in the strong-coupling limit: For $g^2/a_j \gg 1$, the half-filled groundstate corresponds to a Mott insulator where fermions occupy single sites of each layer, avoiding double occupancies of neighbouring sites along the vertical direction (i.e. doublons). This is can be achieved by different fermion configurations corresponding to individually half-filled layers, as depicted in the left schemes of **(a)** and **(b)**. Sequential tunnelling processes can virtually create doublons with an energy cost proportional to the Hubbard interaction strength V_v and, as depicted by the central panels, connect to a different groundstate configuration that is consistent with the Mott-insulating constraint. The depicted super-exchange processes correspond to **(a)** single spin-flip along the y axis, and **(b)** double spin-flip along the x axis.

According to the strong-coupling condition $g^2/a_j \gg 1$, we see that the Hubbard interactions are much larger than any of the intra- or inter-layer tunnellings in this particular regime, since $V_v \gg 1/a_j = |t_j| = |\tilde{t}_j|$. Accordingly, the half-filled groundstate corresponds to a Mott insulator without any pair of fermions occupying simultaneously both layers at the same site (see Fig. 3). Following the condensed-matter nomenclature, we call such high-lying excitations doublons, which necessarily appear as we dope the system away from half-filling, where a non-zero charge gap appears. The remaining question to address is if this Mott insulator is featureless, or if there is some ordering with respect to the orbital/layer degrees of freedom and a non-zero orbital gap.

Although the tunnelling of fermions is inhibited in the half-filled Mott insulator, as it leads to the creation of doublons with a very large energy cost, there can be second-order processes where such doublons are virtually created and annihilated. These virtual tunnellings, also known as super-exchange processes [9,10], are the leading perturbative corrections and become responsible for the antiferromagnetic ordering of Mott insulators in the strong-coupling limit of the standard Hubbard model, as discussed in the introduction. In the present context, analogous super-exchange

mechanisms can be formalized using the language of $SU(2)$ orbital spin operators

$$\begin{aligned}\tau^x_{\boldsymbol{n}} &= c^\dagger_{\boldsymbol{n},\mathrm{u}} c_{\boldsymbol{n},\mathrm{d}} + c^\dagger_{\boldsymbol{n},\mathrm{d}} c_{\boldsymbol{n},\mathrm{u}},\\ \tau^y_{\boldsymbol{n}} &= \mathrm{i} c^\dagger_{\boldsymbol{n},\mathrm{d}} c_{\boldsymbol{n},\mathrm{u}} - \mathrm{i} c^\dagger_{\boldsymbol{n},\mathrm{u}} c_{\boldsymbol{n},\mathrm{d}},\\ \tau^z_{\boldsymbol{n}} &= c^\dagger_{\boldsymbol{n},\mathrm{u}} c_{\boldsymbol{n},\mathrm{u}} - c^\dagger_{\boldsymbol{n},\mathrm{d}} c_{\boldsymbol{n},\mathrm{d}},\end{aligned} \tag{30}$$

and a Schrieffer–Wolff transformation [152] with the following graphical interpretation. Let us start from a common situation that is also found in the standard Hubbard model if we consider that the spin up/down states of the electrons correspond to the two layers. In this process, a pair of fermions occupying neighbouring sites in different layers tunnels, creating a virtual doublon, and then annihilates it through a second tunnelling event. This may lead to an effective swap of the fermions that can be interpreted as a spin-flip exchange $|\uparrow_{\boldsymbol{n}}, \downarrow_{\boldsymbol{n}+\boldsymbol{e}_j}\rangle \rightarrow |\downarrow_{\boldsymbol{n}}, \uparrow_{\boldsymbol{n}+\boldsymbol{e}_j}\rangle$ along any of the two spatial directions (see Fig. 3**(a)** for such an spin-flip exchange along the y axis). We note that, due to the anisotropic fermion tunnellings (see Fig. 1), these spin-flip exchanges will have different strengths along the two axes, the specific value of which can be obtained through the Schrieffer–Wolff formalism $J_{\perp,1} = -1/g^2\xi_2, J_{\perp,2} = -\xi_2/g^2$.

A new virtual process allowed by the pattern of inter-layer tunnellings, with no counterpart in the standard Hubbard model, occurs for a pair of fermions occupying neighbouring sites within the same layer. These fermions can tunnel to the adjacent site by simultaneously changing layer, virtually creating a doublon, and then annihilate it through a second inter-layer tunnelling event. This can lead to an effective pair-tunnelling between the different layers that is consistent with the Mott-insulating state, and may be interpreted as a double-spin-flip exchange $|\uparrow_{\boldsymbol{n}}, \uparrow_{\boldsymbol{n}+\boldsymbol{e}_j}\rangle \rightarrow |\downarrow_{\boldsymbol{n}}, \downarrow_{\boldsymbol{n}+\boldsymbol{e}_j}\rangle$ along any of the two spatial directions (see Fig. 3**(b)** for such a double-spin-flip exchange along the x axis). In this case, the anisotropy and the different phases of the inter-layer tunnellings conspire to yield spin flips of a different strength, but also of an opposite sign depending on direction $\tilde{J}_{\perp,1} = +1/g^2\xi_2, \tilde{J}_{\perp,2} = -\xi_2/g^2$. This sign difference is crucial, as the combination of the two types of spin-flip process can be rewritten as the following effective spin model with direction-dependent interaction:

$$H_{\mathrm{eff}} = \sum_{\boldsymbol{n}} \left(J_x \tau^x_{\boldsymbol{n}} \tau^x_{\boldsymbol{n}+\boldsymbol{e}_2} + J_y \tau^y_{\boldsymbol{n}} \tau^y_{\boldsymbol{n}+\boldsymbol{e}_1} - h\tau^z_{\boldsymbol{n}} \right), \tag{31}$$

where we have introduced the following coupling strengths

$$J_x = \frac{-a_1}{2g^2 a_2}, \quad J_y = \frac{-a_2}{2g^2 a_1}, \quad h = -m - \frac{1}{a_1} - \frac{1}{a_2}. \tag{32}$$

Let us note that, in contrast to the original lattice model (10) we started from, the above model only contains nearest-neighbour quartic terms, and must be supplemented by a so-called Gutzwiller projector $\mathscr{P}_G = \Pi_{\boldsymbol{n}}(1 - c^\dagger_{\boldsymbol{n},\mathrm{u}} c_{\boldsymbol{n},\mathrm{u}} c^\dagger_{\boldsymbol{n},\mathrm{d}} c_{\boldsymbol{n},\mathrm{d}})$ onto the no-doublon subspace. Accordingly, at half filling, every site labelled by $\boldsymbol{n}$ is filled with a single fermion that may occupy either layer, such that the projected orbital four-Fermi operators (30) can be represented in a tensor-product Hilbert space $\mathsf{H}_{\mathrm{eff}} = \otimes_{\boldsymbol{n}} \mathbb{C}^2 = \otimes_{\boldsymbol{n}} \mathrm{span}\{|\uparrow_{\boldsymbol{n}}\rangle, |\downarrow_{\boldsymbol{n}}\rangle\}$ using the standard Pauli matrices

$$\tau^\alpha_{\boldsymbol{n}} = \mathbb{I}_2 \overset{m-1}{\cdots} \otimes \mathbb{I}_2 \otimes \sigma^\alpha \otimes \mathbb{I}_2 \otimes \overset{N_1 N_2 - m}{\cdots} \otimes \mathbb{I}_2, \tag{33}$$

where $m = (n_2 - 1)N_1 + n_1$ labels the sites of the rectangular lattice from east to west and south to north. In the rest of this section, we use this tensor-product description of the strong-coupling Hilbert space. This allows us to interpret Eq. (31) as a spin model with ferromagnetic couplings (32), such that the original fermionic statistics no longer apply. We note that, by performing a unitary operation flipping the operators $\tau^x_{\boldsymbol{n}}, \tau^y_{\boldsymbol{n}} \rightarrow, (-1)^{(n_1+n_2)}\tau^x_{\boldsymbol{n}}, (-1)^{(n_1+n_2)}\tau^y_{\boldsymbol{n}}$ in a checkerboard pattern, the ferromagnetic couplings become anti-ferromagnetic $J_x, J_y \rightarrow -J_x, -J_y$, while the transverse field is preserved. There is thus no fundamental difference between the ferromagnetic or anti-ferromagnetic spin models.

Notably, this spin model (31) belongs to the family of *quantum compass models* [153]. In comparison to the Heisenberg model [154], which arises in the strong-coupling limit of the standard Hubbard model [155], there are no $\tau^z\tau^z$ interactions. Moreover, $\tau^x\tau^x$ interactions only

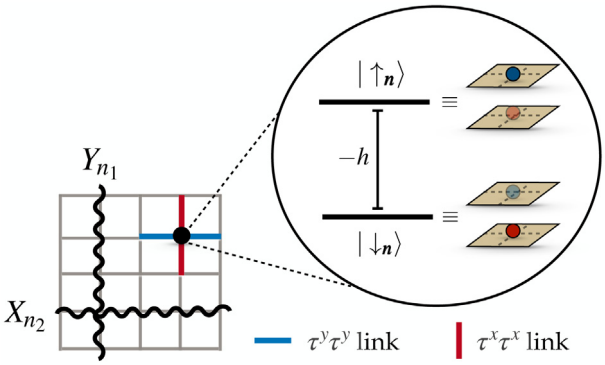

Fig. 4. Scheme of the 90° quantum compass model in a transverse field: The orbital spins are arranged on the sites of a rectangular lattice, where the inset depicts the mapping of the spin states to the two possible distribution of fermions avoiding doublons. The energy difference between these two spin states is proportional to the transverse field h. The spin–spin interactions can be depicted by blue (red) links forming 90°, which represent a $\tau^y\tau^y$ ($\tau^x\tau^x$) coupling of strength J_x (J_y). The wavy lines represent the two types of sliding symmetry described in the text. (For interpretation of the references to colour in this figure legend, the reader is referred to the web version of this article.)

couple neighbouring sites along the y-direction, whereas the $\tau^y\tau^y$ interactions do so along the x-direction, as depicted in the scheme of Fig. 4. Up to an irrelevant relabelling, this corresponds to the anisotropic 90° compass model in a square lattice [156], since $J_x \neq J_y$ in general (32). This characteristic directionality of the spin–spin interactions, which are no longer invariant under C_4 rotations of the spatial lattice, evokes a compass that distinguishes north/south from east/west directions. In the honeycomb lattice [157], a similar directionality is responsible for the appearance of intrinsic topological order in a spin-liquid groundstate [158,159]. Again, this ordering cannot be understood by the spontaneous breakdown of symmetry or by the onset of a non-zero order parameter, all of which are absent in spin liquids even down to zero temperature. Instead, intrinsic topological order hosts long-range entanglement in the groundstate and anionic excitations, which differs from the QAH phases that have been discussed so far.

In the case of the square lattice, the anisotropic 90° compass model for a vanishing transverse field $h = 0$ (31) has been thoroughly studied from both condensed-matter and quantum-information perspectives. This model is invariant under the so-called sliding symmetries [156, 160], which lie midway between a local gauge symmetry and a purely global one. These sliding symmetries consist of strings formed by the product of $\tau^x_{\boldsymbol{n}}$, $\tau^y_{\boldsymbol{n}}$ operators along rows and columns $X_{n_2} = \prod_{n_1} \tau^x_{(n_1,n_2)}$, $Y_{n_1} = \prod_{n_2} \tau^y_{(n_1,n_2)}$ which, due to the interaction directionality, clearly commute with the Hamiltonian $[X_{n_2}, H_{\text{eff}}] = [Y_{n_1}, H_{\text{eff}}] = 0$, but anti-commute with each other $\{X_{n_2}, Y_{n_1}\} = 0$, $\forall n_1, n_2$. In Kitaev's toric [161] and surface [162–164] codes for quantum error correction (QEC), where the spins are arranged on the lattice links rather than the sites and interact via four-body terms instead of two-body ones, these sliding symmetries also appear along rows and columns of the real and reciprocal lattices, and can be related to Dirac's electric and 't Hooft's magnetic field lines of a $\mathbb{Z}_2$ lattice gauge theory [165–167]. This underlying gauge symmetry allows one to identify an extensive set of local operators that commute with the Hamiltonian and with each other, and generate the so-called stabilizer group [168] under which the groundstate manifold remains invariant. Moreover, these stabilizers also allow one to connect the sliding symmetries acting on different rows (columns), such that they have the same effect on the groundstate manifold. In this way, one can use the sliding symmetries as unitary operations on logical qubit(s) encoded in the groundstate manifold. Although these logical qubits are not inherently robust to noise, one can perform QEC by measuring the local stabilizers, inferring the most likely error and, subsequently, correcting it by applying simple unitaries to bring the system back to the groundstate manifold, withstanding a considerable amount of physical errors [169]. From a condensed-matter

perspective, the groundstate of the toric/surface-code Hamiltonian is a quantum spin liquid with intrinsic topological order rather than symmetry-breaking long-range order, such that the encoded logical qubits and QEC codes are typically referred to as topological qubits and topological codes, respectively.

For the 90° compass model (31), on the contrary, there is no $\mathbb{Z}_2$ gauge symmetry and the commuting set of stabilizers is no longer formed by local observables. Instead, one defines the stabilizers by taking the product of two sliding symmetries along a neighbouring pair of rows (columns) $X_{n_2}X_{n_2+1}$ $\left(Y_{n_1}Y_{n_1+1}\right)$, which leads to the so-called subsystem Bacon–Shor codes [170]. Although gauge symmetry is no longer present in these codes, the underlying notion of redundancy that underlies such local symmetries still appears in a different guise. These codes host additional gauge qubits, the state of which is irrelevant, and can be manipulated using certain gauge operations without affecting the encoded logical information [171]. This can be exploited to improve the QEC routines. For instance, QEC based on the Bacon–Shor code can still be performed by the sequential measurements of a set of local gauge operators corresponding to some of the compass-model pairwise interactions (31), such that their product yields the measurement outcome of the desired non-local stabilizer. This approach lowers the overhead and complexity with respect to fault-tolerant protocols for the toric/surface code [172,173] but, on the other hand, can only attain a bounded reduction of the logical error rate with respect to the physical one, which is achieved for intermediate optimal lattice sizes [174]. Interestingly, one may also use these pairwise interactions to modify the stabilizers by a so-called gauge fixing, making the encoded logical qubits more robust to certain types of biased errors. This leads to the so-called two-dimensional compass codes which, in contrast to Bacon–Shor codes, have a non-zero error threshold, below which the protection of the logical qubits can be improved arbitrarily by steadily increasing the lattice size [175,176].

Regardless of the relevance of the 90° compass model for QEC, the limit of zero transverse field $h = 0$ has also received considerable attention from the condensed-matter community. Note that the total number of sliding symmetries X_{n_2}, Y_{n_1} scales with half of the perimeter of the square lattice $N_1 + N_2$, which could lead to exponentially-large groundstate degeneracies as occurs for classically-frustrated magnets. Since these symmetries anti-commute with each other $\{X_{n_2}, Y_{n_1}\} = 0$, while the aforementioned stabilizers satisfy $[X_{n_2}X_{n_2+1}, Y_{n_1}] = 0 = [X_{n_2}, Y_{n_1}Y_{n_1+1}]$, $\forall n_1, n_2$, one can indeed prove rigorously that all of the eigenstates are at least two-fold degenerate, independently of the specific system size [160]. This does not preclude, however, that higher degeneracies exist. In fact, it has been argued numerically that there are exponentially-many low-lying excitations that collapse exponentially fast to the groundstate as the lattice size increases [177], leading to the aforementioned analogue of frustrated magnets with an exponentially-large groundstate manifold. This connects to the quantum-mechanical version of the mechanism of order by disorder [178] whereby quantum fluctuations, which typically tend to destroy a possible long-range order, instead induce it by selecting a particular groundstate from the exponentially-large manifold of possible candidates. In fact, instead of a quantum spin-liquid phase, one finds two different ferromagnetic orders in the groundstate, which are connected by a first-order phase transition [177,179,180] as the ratio of the exchange couplings is varied across the self-dual point $J_x = J_y$ [156].

To the best of our knowledge, the 90° compass model in a non-vanishing transverse field (31) remains largely unexplored in comparison to the zero-field limit discussed above. The transverse field is a source of additional quantum fluctuations, which favours a paramagnetic phase where all spins align in the direction of the transverse field. In our recent work [117], we briefly discussed how the competition with the magnetic phases can give rise to second-order phase transitions at finite ratios of the transverse-field to exchange couplings. In the two following subsections, we shall give a detailed exposition of our findings using variational mean-field and tensor-network approaches. Since either magnetic or paramagnetic phases are ultimately different from the QAH phase discussed in the previous section, our results show that the fate of this topological phase is to disappear in the strong-coupling limit. Equipped with the lessons learned from the strong-coupling limit, and in particular the identification of the magnetic orders that compete with the topological phase, we will analyse in the next section how large the interactions can be before the correlated QAH phase gives way to the (para)magnets. Before turning to this discussion, let us note that the effective spin models will be modified when other choices of the Wilson parameters $r_j \neq 1$ are

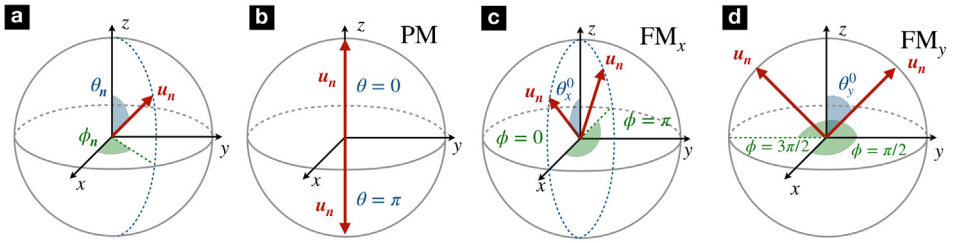

Fig. 5. Spin coherent states and mean-field solutions: **(a)** The variational ansatz (34) is built from a tensor product of spin coherent states characterized by a unit vector $\boldsymbol{u}_n$ with polar and azimuthal angles $\theta_{\boldsymbol{n}}, \phi_{\boldsymbol{n}}$. For spin $S = 1/2$, the unit sphere is commonly referred to as Bloch's sphere. **(b)** Paramagnetic PM phase, where each of the spins points along the north or south pole depending on the sign of the transverse field h. **(c, d)** Ferromagnetic phases where all spins are parallel and point in two possible directions within the xz (FM$_x$) or yz (FM$_y$) plane.

explored. By simple inspection of Fig. 3, it is clear that the intra-layer second-order processes **(a)** and the inter-layer ones **(b)** have different strengths even when acting along the same axis, which will lead to perturbations breaking the perfect directionality of the spin–spin interactions. However, these perturbations should preserve the underlying global symmetry, and we believe that unless one focuses on very large values of the Wilson parameters, they will not modify the nature of the critical lines. This question will be studied in the future.

3.2. Variational mean-field description

Let us now describe a variational mean-field approach to the groundstate of the 90° compass model in a non-vanishing transverse field (31). There are a variety of methods for obtaining a mean-field approximation in a many-body problem [181], all of which share the common aspect of addressing non-perturbative phenomena, such as criticality and phase transitions, by underestimating the effect of inter-particle correlations. Although mean-field methods have their own well-known limitations, they typically give a correct qualitative picture of effects that cannot be captured by perturbation theory. In this subsection, we focus on variational mean-field theory [181], where one constructs a variational ansatz by a family of fully-uncorrelated tensor product states.

In the present context, we define the variational ansatz as $|\Psi_{\mathrm{MF}}(\{\theta_{\boldsymbol{n}}, \phi_{\boldsymbol{n}}\})\rangle = \otimes_{\boldsymbol{n}} |\psi_{\mathrm{MF}}(\theta_{\boldsymbol{n}}, \phi_{\boldsymbol{n}})\rangle$, where the state of each of the lattice spins $|\psi_{\mathrm{MF}}(\theta_{\boldsymbol{n}}, \phi_{\boldsymbol{n}})\rangle$ is described by a spin coherent state pointing along the unit vector $\boldsymbol{u}_{\boldsymbol{n}} = (\sin\theta_{\boldsymbol{n}} \cos\phi_{\boldsymbol{n}}, \sin\theta_{\boldsymbol{n}} \sin\phi_{\boldsymbol{n}}, \cos\theta_{\boldsymbol{n}})$ within the 2-sphere [182]. Here, $\theta_{\boldsymbol{n}} \in [0, \pi]$ and $\phi_{\boldsymbol{n}} \in [0, 2\pi)$ are the so-called polar and azimuthal angles depicted in Fig. 5**(a)**, which can in principle be inhomogeneous across the lattice. However, given our previous discussion of the zero-field limit, where we remarked on the competition of two possible ferromagnetic orders, we shall assume that all spins point in the same direction $\theta_{\boldsymbol{n}} = \theta$, $\phi_{\boldsymbol{n}} = \phi$, $\forall \boldsymbol{n}$, such that translational invariance is maintained in the groundstate. By selecting the state where all spins point to the north pole as a fiducial state, the spin coherent state can be written as

$$|\Psi_{\mathrm{MF}}(\{\theta, \phi\})\rangle = \otimes_{\boldsymbol{n}} \mathrm{e}^{\frac{\mathrm{i}}{2}\theta\left(\sin\phi\tau^x_{\boldsymbol{n}} - \cos\phi\tau^y_{\boldsymbol{n}}\right)} |\uparrow_{\boldsymbol{n}}\rangle, \tag{34}$$

which leads to the following set of expectation values

$$\begin{aligned} &\langle\Psi_{\mathrm{MF}}(\{\theta, \phi\})|\tau^{\alpha}_{\boldsymbol{n}}|\Psi_{\mathrm{MF}}(\{\theta, \phi\})\rangle = u^{\alpha}_{\boldsymbol{n}}, \\ &\langle\Psi_{\mathrm{MF}}(\{\theta, \phi\})|\tau^{\alpha}_{\boldsymbol{n}} \cdot \tau^{\beta}_{\boldsymbol{n}'}|\Psi_{\mathrm{MF}}(\{\theta, \phi\})\rangle = u^{\alpha}_{\boldsymbol{n}} u^{\beta}_{\boldsymbol{n}'}. \end{aligned} \tag{35}$$

We can now calculate the variational energy through the expectation value of the effective compass Hamiltonian on these coherent states $\epsilon(\theta, \phi) = \langle\Psi_{\mathrm{MF}}|H_{\mathrm{eff}}|\Psi_{\mathrm{MF}}\rangle / N_1 N_2$, yielding

$$\epsilon(\theta, \phi) = J_x \sin^2\theta \cos^2\phi + J_y \sin^2\theta \sin^2\phi - h\cos\theta. \tag{36}$$

In a variational approach, the groundstate can be found by calculating the partial derivatives of the variational energy with respect to θ, ϕ and setting them equal to zero, which leads to the non-linear system of equations

$$\sin(2\theta)(J_x\cos^2\phi + J_y\sin^2\phi) + h\sin\theta = 0, \tag{37}$$

$$\sin(2\phi)\sin^2\theta(J_x - J_y) = 0. \tag{38}$$

There are three different types of solution. If $\theta = p\cdot\pi$ with $p\in\mathbb{Z}_2$, all the terms in (37) and (38) are zero for arbitrary ϕ. In this case all the spins point along the poles of the 2-sphere, as depicted in Fig. 5**(b)** such that the energy is

$$\epsilon(p\pi, \phi) = \pm h. \tag{39}$$

The two possible states represent paramagnetic states with the spins either aligned or anti-aligned with respect to the transverse magnetic field. We shall refer to this phase as PM.

The second set of possible solutions is found for $\phi = p\cdot\pi$ with $p\in\mathbb{Z}_2$, such that Eq. (38) is always zero. In this case the first equation reduces to $2J_x\cos(\theta) + h = 0$, and the solution is found for the groundstate polar angle

$$\theta_x^0 = \arccos\left(\left|\frac{h}{2J_x}\right|\right). \tag{40}$$

The particular ground state energy is given by

$$\epsilon(\theta_x^0, p\pi) = -|J_x|\left(1 - \frac{h^2}{4J_x^2}\right). \tag{41}$$

Considering the expectation values in Eq. (35), these solutions describe a ferromagnetic state where all spins have a non-zero magnetization along the x-z plane (see Fig. 5**(c)**). We shall refer to this phase as FM_x.

The third type of solution occurs for $\phi = (2p+1)\frac{\pi}{2}$ with $p\in\mathbb{Z}_2$, where equation (38) is again zero. Then, the first equation reduces to $2J_y\cos(\theta) + h = 0$. It follows that the groundstate polar angle is given by

$$\theta_y^0 = \arccos\left(\left|\frac{h}{2J_y}\right|\right), \tag{42}$$

and the corresponding energy per spin is

$$\epsilon\left(\theta_y^0, (2p+1)\frac{\pi}{2}\right) = -|J_y|\left(1 - \frac{h^2}{4J_y^2}\right). \tag{43}$$

Considering the expectation values in Eq. (35), these solutions describe a ferromagnetic state where all spins have a non-zero magnetization along the y-z plane (see Fig. 5 **(d)**). We shall refer to this phase as FM_y.

Let us now discuss the possibility of finding also a mean-field solution with mixed magnetization along both the x and y directions. As one can see, the condition $J_x = J_y =: J$ solves directly the second equation (38) for all possible angles. Similarly, all the dependence of Eq. (37) on ϕ disappears, such that one can find solutions for arbitrary azimuthal angle provided that $2J\cos\theta + h = 0$, all of which have the same energy (36). These solutions contain the previous second- and third-type ferromagnetic solutions discussed previously, and will be referred to as FM_ϕ. For zero transverse field, this is the mean-field account of the special isotropic point of the 90° compass model, where we recall that an exponentially-large groundstate degeneracy was predicted in the thermodynamic limit [177]. Although the variational mean-field does not capture the exponentially-fast clustering of the low-lying excitations with the system size, it identifies the isotropic regime $J_x = J_y$ as a special point. Let us note that, contrary to the standard situation in Heisenberg (XY) models, the independence on the azimuthal angle does not derive from a global $SU(2)$ ($U(1)$) symmetry, where spontaneous symmetry breaking would in principle select only a specific groundstate angle. For the compass model, this independence is instead related to the intermediate sliding symmetries. By

inspecting the two solutions in Eqs. (41)–(43), one can also see that the point $J_x = J_y$ corresponds to a level crossing, such that the mean-field analysis also captures the first-order nature of the phase transition at zero transverse field. At this point, the spins change their orientation abruptly from x- to y-direction.

It is now a matter of comparing the energies of all the possible mean-field solutions in Eqs. (39), (41) and (43) to find the groundstate and possible quantum phase transitions for a non-vanishing transverse field. Note that the compass Hamiltonian (31) in the limit $|J_x| \gg |J_y|, |h|$ corresponds to a set of decoupled Ising columns with a ferromagnetic ground state where all spins point along the x-direction. From our mean-field solution, this phase turns out to be the low-energy configuration for weaker exchange couplings J_x whenever $|J_x| > |J_y|$, which requires $a_1 > a_2$ in light of Eq. (32), and

$$\langle \tau^x_{\boldsymbol{n}} \rangle = \sin(\theta^0_x) = \sqrt{1 - \frac{h^2}{4J_x^2}}, \quad \text{if } |J_x| \geq \frac{|h|}{2}. \tag{44}$$

Note that this leads to a quantum phase transition towards the second type of solution (44) at $|h| = 2|J_x|$, where the global $\mathbb{Z}_2$ symmetry generated by $U = \Pi_{\boldsymbol{n}} \tau^z_{\boldsymbol{n}}$ is spontaneously broken. This symmetry can also be combined with inversion symmetry of the spins about the centre of the rectangular lattice $\boldsymbol{n} \to (N_1, N_2) - \boldsymbol{n}$. For smaller transverse fields, the order parameter (44) becomes non-zero, and can be attained by two possible azimuthal angles $\phi = p\pi$ with $p \in \{0, 1\}$, corresponding to the two possible ferromagnetic arrangements, which are degenerate due to the spontaneous breaking of the $\mathbb{Z}_2$ symmetry. For larger transverse fields, the spins align with the transverse field, pointing along the $\pm z$ axis for positive/negative values of h, and the spontaneous magnetization along the x axis vanishes exactly. Note that only one of the paramagnetic configurations is the low-energy state, and there is thus no degeneracy as the $\mathbb{Z}_2$ symmetry is preserved in this case. This critical point thus represents a second-order quantum phase transition between a ferromagnet along the x axis (FM_x) and a paramagnet (PM), in contrast to the first-order nature of the self-dual critical point $J_x = J_y$ for vanishing transverse field. We emphasize that the symmetry being broken is not related to the internal $U(N)$ symmetry, but is instead a combined spatial and spin inversion symmetry in the language of the quantum compass model. In the following sections, we shall re-interpret this discrete symmetry in the language of the Dirac spinors and the emerging continuum QFTs.

The same type of argument holds in the opposite direction of the exchange-coupling anisotropy, where the model becomes a set of decoupled Ising rows in the limit of very large anisotropy $|J_y| \gg |J_x|, |h|$. We find that for $|J_y| > |J_x|$ and $|J_y| > |h|/2$, the non-zero order parameter is

$$\langle \tau^y_{\boldsymbol{n}} \rangle = \sin(\theta^0_y) = \sqrt{1 - \frac{h^2}{4J_y^2}}, \quad \text{if } |J_y| \geq \frac{|h|}{2}. \tag{45}$$

and corresponds to the third type of variational solutions discussed above. In this case, the critical point $|h| = 2|J_y|$ describes a second-order quantum phase transition between an ferromagnet along the y axis (FM_y) and a paramagnet (PM).

At this point it is worth taking a step back to understand these phases from the perspective of the orbital spin operators (30) and the Hubbard bilayer interpretation. The PM corresponds to a density-imbalanced Mott-insulating phase, where one finds the fermions occupying all of the sites of a single layer. Depending on the sign of the effective transverse field (32), the upper ($h > 0$) or lower ($h < 0$) layers will be the preferred choice. The FM_x (FM_y) phases represent a long-range order whereby the fermions equally populate both layers, avoiding double occupancies, and delocalizing over the two vertically-neighbouring sites of the bilayer. This establishes a real (complex) non-zero bond density $\langle \tau^x_{\boldsymbol{n}} \rangle \propto \mathrm{Re}\{\langle c^\dagger_{\boldsymbol{n},\mathrm{u}} c_{\boldsymbol{n},\mathrm{d}} \rangle\}$ $\left(\langle \tau^y_{\boldsymbol{n}} \rangle \propto \mathrm{Im}\{\langle c^\dagger_{\boldsymbol{n},\mathrm{u}} c_{\boldsymbol{n},\mathrm{d}} \rangle\} \right)$ that preserves translational invariance and long-range order $\langle \tau^x_{\boldsymbol{n}} \tau^x_{\boldsymbol{n}+\boldsymbol{r}} \rangle \to \langle \tau^x_{\boldsymbol{n}} \rangle^2$ $\left(\langle \tau^y_{\boldsymbol{n}} \tau^y_{\boldsymbol{n}+\boldsymbol{r}} \rangle \to \langle \tau^y_{\boldsymbol{n}} \rangle^2 \right)$ as $|\boldsymbol{r}| \to \infty$. We will generally refer to these phases as orbital ferromagnets and orbital paramagnets.

Let us now rewrite the equations for the critical lines separating these orbital phases in terms of the original microscopic parameters of the four-Fermi–Wilson model (32). We find two different

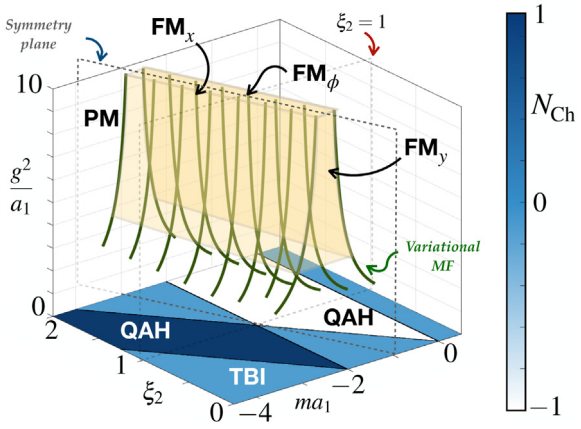

Fig. 6. Orbital ferromagnetism for strong couplings and $N = 1$: In the limit of large interactions $g^2/a_j \gg 1$, we have identified orbital paramagnetic (PM) and ferromagnetic (FM$_x$,FM$_y$, separated by the critical lines in Eq. (46). The inner volume, coloured with a light orange, contained within these lines corresponds to a ferromagnetic phase where the orbital spins point along the x axis for spatial anisotropies $\xi_2 > 1$, or along the y axis for $\xi_2 < 1$. In the isotropic limit $\xi_2 = 1$, the spins van order along any azimuthal angle $\phi \in [0, 2\pi)$, leading to the FM$_\phi$ phase contained in the area within the critical lines in Eq. (46). All the surrounding region in white for $g^2 > 0$ corresponds to the paramagnet. We also plot the symmetry plane that divides the ferromagnets into two equal halves, given by the condition of a vanishing transverse field $h = 0$, i.e. $ma_1 = 1 + \xi_2$. (For interpretation of the references to colour in this figure legend, the reader is referred to the web version of this article.)

critical lines depending on the anisotropy

$$\begin{aligned} g^2 &= \frac{a_1}{a_2\left|m + \frac{1}{a_1} + \frac{1}{a_2}\right|}, \quad \text{if } a_1 > a_2, \\ g^2 &= \frac{a_2}{a_1\left|m + \frac{1}{a_1} + \frac{1}{a_2}\right|}, \quad \text{if } a_1 < a_2. \end{aligned} \tag{46}$$

These critical lines are depicted as green solid lines in Fig. 6, and delimit a volume in parameter space where one expects to find the symmetry-broken orbital ferromagnets. We are thus certain that the QAH phases described in the previous section will disappear when the interactions g^2 are sufficiently strong. However, the variational mean-field approach for the strong-coupling limit has its own limitations. First of all, being a strong-coupling limit that is exact in the strict limit $g^2/a_j \to \infty$, we cannot predict what happens at intermediate interactions, nor locate the critical lines separating the QAH phase from the ferromagnets and paramagnets. In addition, being a mean-field approximation, we expect that the exact location of the critical lines and the scaling of the order parameter will differ from the correct critical phenomena, which would require other methods that can better accommodate for inter-particle correlations. We will address both limitations in the following sections.

3.3. Variational tensor-network description

In this section, we benchmark the results of the mean-field approximation for the 90° compass model presented in the previous section by means of a variational algorithm based on a projected entangled-pair state (PEPS) [183–186]. The PEPS represents a natural generalization of the one-dimensional variational ansatz based on matrix product states (MPS) [184,187] to two, or even higher, spatial dimensions. These variational states improve upon the separable mean-field ansatz (34) by including inter-particle correlations, and can be understood in terms of pairs of maximally-entangled states describing auxiliary degrees of freedom on neighbouring lattice sites,

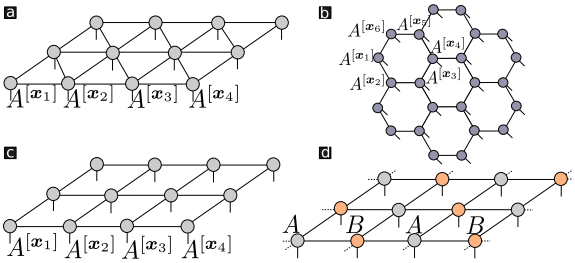

Fig. 7. PEPS representations: Diagrammatic representations of PEPSs corresponding to different lattice patterns: **(a)** a triangular lattice, **(b)** a hexagonal lattice, **(c)** a square lattice, and **(d)** infinite square lattice PEPS with a two-site unit cell.

which are locally projected onto the lower-dimensional subspace of physical spins residing at each lattice site. This construction can be mathematically expressed as a network of tensors with multiple indexes corresponding to the physical and auxiliary degrees of freedom, such that those corresponding to the auxiliary ones are contracted. Accordingly, the PEPS belongs to the family of tensor-network variational algorithms.

To study groundstate properties of quantum lattice Hamiltonians in two spatial dimensions, one can *(i)* variationally optimize the PEPS tensors, so as to minimize the expectation value of the corresponding Hamiltonian [188,189]. Alternatively, in analogy to spectroscopic methods that determine the particle spectrum via the imaginary-time evolution of correlators in Euclidean LFTs [20], *(ii)* one may evolve the system in imaginary time until a stationary state corresponding to the groundstate is reached. This assumes that this groundstate is unique, and that the energy gap is non-zero, as done in the time-evolving block-decimation method (TEBD) for one-dimensional chains [190–192]. In the following, we will use this second method in the thermodynamic limit, for the infinite PEPS state (iPEPS), which we describe briefly in the next section.

3.3.1. Projected entangled pair states (PEPS)

Here, we briefly review the notation and fundamental properties of projected entangled pair states. Let us consider a two-dimensional spatial lattice consisting of N_1N_2 sites, each of which hosts a quantum sub-system with a d-dimensional local Hilbert space $\mathbb{C}^d$, e.g. $d = 2$ for a spin-1/2 lattice model. The full Hilbert space of the system is thus $\mathsf{H} = \mathbb{C}^d \otimes \overset{N_1N_2-2}{\cdots} \otimes \mathbb{C}^d$, such that the dimension grows exponentially with the number of lattice sites, and the problem quickly becomes intractable, already for moderately low values of N_1N_2. In order to avoid this problem, we use a PEPS to represent a pure state.

The PEPS describes a state through interconnected tensors. As in Eq. (33), we use an integer $m \in \{1, \ldots, N_1N_2\}$ to label the lattice sites ordered from east to west and south to north $\boldsymbol{x}_m = (x_m, y_m)$, and define the PEPS variational ansatz as

$$|\psi\rangle = \sum_{\{s_{\boldsymbol{x}_m}\}} F\left(A^{[\boldsymbol{x}_1]}_{s_{\boldsymbol{x}_1}}, A^{[\boldsymbol{x}_2]}_{s_{\boldsymbol{x}_2}}, \ldots, A^{[\boldsymbol{x}_{N_1N_2}]}_{s_{\boldsymbol{x}_{N_1N_2}}}\right) |s_{\boldsymbol{x}_1}, s_{\boldsymbol{x}_2} \ldots, s_{\boldsymbol{x}_{N_1N_2}}\rangle, \tag{47}$$

where we sum over all possible states in the basis of the local Hilbert space, labelled by $\{s_{\boldsymbol{x}_m}\}$. This PEPS is represented by a network of N_1N_2 tensors $A^{[\boldsymbol{x}_m]}_{s_{\boldsymbol{x}_n}}$, some of which are connected according to the geometry of the lattice and the notion of neighbouring lattice sites. Each tensor of the PEPS has n so-called bond indices of dimension D, which describe the aforementioned auxiliary degrees of freedom, and a single physical index of dimension d. The choice of n in the tensor network depends on the geometry of the lattice and can be chosen arbitrary. The function F contracts all the tensors $A^{[\boldsymbol{x}_m]}_{s_{\boldsymbol{x}_m}}$, according to this pattern, and then performs the trace to obtain a scalar quantity such that Eq. (47) can be understood as a parametrization of a particular set of states in the exponentially-large physical Hilbert space H. In Fig. 7, we show diagrammatically several PEPSs for systems corresponding to different geometries with open boundary conditions (OBC). The spheres

represent the tensors, with solid lines depicting the auxiliary and physical indexes. The vertical ones stand for the physical indexes, whereas the planar ones that connect neighbouring tensors stand for the contracted auxiliary indexes. In the case of the system geometry being a square lattice pattern with OBC, the PEPS consists of tensors in the bulk $A^{[\boldsymbol{x}_m]}$, which have four bond indices connecting neighbouring tensors, and one physical index s_m (Fig. 7**(c)**). Overall, the PEPS depends on $O(N_1N_2D^4d)$ variational parameters.

If we assume a translationally-invariant state with bond dimension $D = 1$ and spin-1/2 physical states $d = 2$, we are left with only two variational parameters, corresponding to our previous mean-field ansatz. Accordingly, for any $D > 1$, the PEPS captures inter-particle correlations and improves upon the mean-field variational family. The accuracy of the ansatz can be systematically controlled by the bond dimension D of the auxiliary indices. This parameter is related to the maximum entanglement content that can be handled by the simulations [183]. In practice, increasing the value of D leads to a better description of the groundstate and, therefore, to more accurate estimations of the different observable quantities. It turns out that the PEPS parametrization can describe very well the entanglement structure of many interesting two-dimensional quantum systems, including low-energy eigenstates of gapped Hamiltonians with local interactions. More specifically, PEPS satisfy the entanglement area law and the scaling of entanglement entropy of an $L \times L$ block within the larger $N_1 \times N_2$ lattice of a PEPS scales with $O(L \log D)$.

This construction can be generalized to any lattice shape and dimension and one can show that any state can be written as a PEPS if we allow the bond dimension to become very large. In the thermodynamic limit, an efficient variational tensor network ansatz is the iPEPS. It consists of a rectangular unit cell of tensors with one tensor per lattice site, $A^{[x,y]}$ where $[x, y]$ label the coordinates of a tensor relative to the unit cell of size $L_x \times L_y = N_T$, as shown in Fig. 7**(d)** for a 4-site cell.

3.3.2. Infinite PEPS ansatz and optimal update

In order to get an approximate representation of the groundstate of a given Hamiltonian H, the tensors of the PEPS in Eq. (47) need to be optimized. This is typically obtained by minimizing the expectation value of $\langle\psi|H|\psi\rangle$, or by simulating an evolution in imaginary time $|\psi\rangle \simeq e^{-\beta H}|\psi_0\rangle$, where $|\psi_0\rangle$ is some initial state. In either case, the tensors that define the iPEPS are optimized iteratively.

In this work, this optimization has been performed based on the imaginary-time evolution of the initial state. In particular, we use the full update introduced in Refs. [193,194]. Indeed, for a given Hamiltonian H, and for a given initial state described by an iPEPS with a unit cell composed of two tensors A and B, the ground state of the system can be obtained by evolving an initial state $|\psi_0\rangle$ in imaginary time β as

$$|\psi_{GS}\rangle = \lim_{\beta\to\infty} \frac{e^{-\beta H}|\psi_0\rangle}{\|e^{-\beta H}|\psi_0\rangle\|} \tag{48}$$

This imaginary-time evolution is achieved in practice by breaking the evolution operator $e^{-\beta H}$ into a sequence of two-body gates, using a Suzuki–Trotter decomposition expansion. To this end, the Hamiltonian H is rewritten as

$$H = H_l + H_r + H_u + H_d, \tag{49}$$

where each term H_i is the sum of commuting Hamiltonian terms for links labelled as (left l, right r, up u, and down d). Using the first order Suzuki–Trotter decomposition, the time-evolution operator is split into

$$e^{-\beta H} = \left(e^{-H\delta}\right)^M \simeq \left(e^{-H_l\delta}e^{-H_r\delta}e^{-H_u\delta}e^{-H_d\delta}\right)^m, \tag{50}$$

where we have divided the total evolution time into $M = \beta/\delta$ steps, where δ represents the infinitesimal imaginary-time step. Each term of the Hamiltonian H_i is a sum of commuting terms, so that, we can rewrite $e^{H_i\delta}$ in Eq. (50) as a product of two-site operators

$$e^{H_i\delta} = \prod e^{-h^{[\boldsymbol{x},\boldsymbol{x}']}\delta} = \prod g^{[\boldsymbol{x},\boldsymbol{x}']}. \tag{51}$$

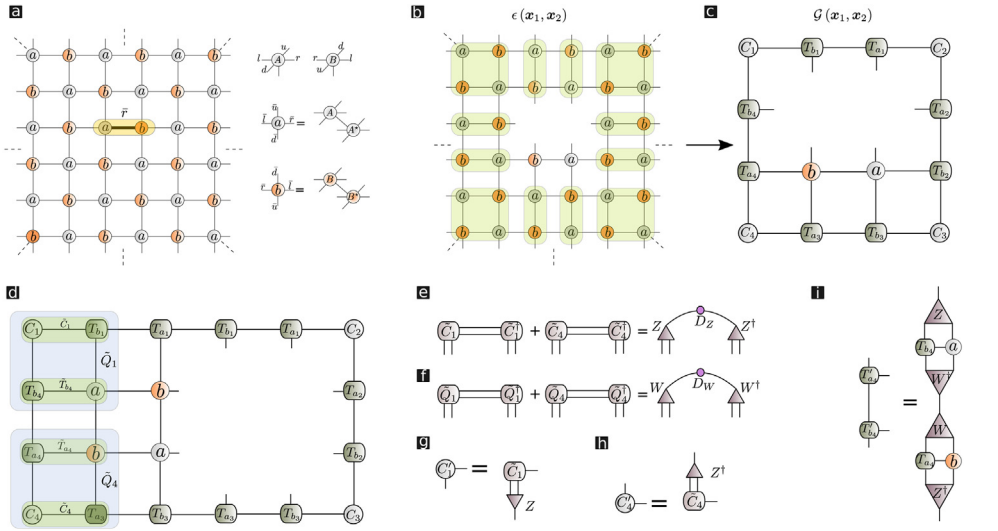

Fig. 8. Effective environment in the iPEPS algorithm: **(a)** Left: 2d lattice of tensors formed from a and b; right: contractions to obtain tensors a and b. **(b)** Environment of the two-site unit cell for a specific r link. **(c)** Effective environment of a given link on the lattice (here an r link). It is formed by twelve tensors. **(d)** two new columns are inserted, absorbed towards the left, and renormalized individually. **(e)** Eigenvalue decomposition for the sum of the squares of CTMs. **(f)** Eigenvalue decomposition for the sum of the squares of Q tensors. **(g)**–**(h)** The CTMs $\tilde{C}_1$, and $\tilde{C}_4$ are renormalized with isometry Z. **(i)** Two isometries Z and W are used to obtain the renormalized half-row transfer matrices T'_{a_4} and T'_{b_4}. (For interpretation of the references to colour in this figure legend, the reader is referred to the web version of this article.)

We start by addressing only the update of the tensors A and B defining a r link, after applying $e^{-\delta H_r}$ to $|\psi\rangle$, which can then be generalized to all of the remaining links. We thus assume that the gate g is applied on just one of the r links. After applying the gate, we obtain a new iPEPS $|\psi_{A',B'}\rangle$ which is characterized by a tensor A and B everywhere except for the two tensors connected by the link where the gate acted. The effect of the gate g is to increase the bond dimension of the iPEPS. For this reason, the iPEPS $|\psi_{A',B'}\rangle$ needs to be approximated by a new one defined by two approximated tensors $\tilde{A}$ and $\tilde{B}$, where these two tensors again have the same bond dimension D fixed at the beginning of the algorithm. In particular, the new PEPS is calculated by minimizing the distance to $|\psi_{A',B'}\rangle$

$$\min_{\tilde{A},\tilde{B}} \| |\psi_{A',B'}\rangle - |\psi_{\tilde{A},\tilde{B}}\rangle \|^2 = \min_{\tilde{A},\tilde{B}} d\left(\tilde{A},\tilde{B}\right), \tag{52}$$

where we have introduced

$$d\left(\tilde{A},\tilde{B}\right) = \langle \psi_{A',B'}|\psi_{A',B'}\rangle + \langle \psi_{\tilde{A},\tilde{B}}|\psi_{\tilde{A},\tilde{B}}\rangle - \langle \psi_{\tilde{A},\tilde{B}}|\psi_{A',B'}\rangle - \langle \psi_{A',B'}|\psi_{\tilde{A},\tilde{B}}\rangle. \tag{53}$$

Therefore, in order to optimally update the iPEPS, minimizing the distance $d\left(\tilde{A},\tilde{B}\right)$ in Eq. (53), we need to *(i)* compute the environment for that specific r link following the corner transfer matrix (CTM) scheme, which was originally derived by Baxter [195,196]. This leads to an approximate representation of the environment in terms of corner matrices and transfer tensors [193]. After this step, we need to *(ii)* determine the optimal new tensors $\tilde{A}$ and $\tilde{B}$ for the link, using the optimization techniques proposed in [192,194], which are referred to the full update scheme. This represents a clean and accurate protocol for performing the tensor update during the imaginary time evolution in which the effect of the entire wave function on the bond tensors is considered including the environmental tensor network. Let us now discuss some further important details of the algorithm.

(i) Environment approximation: To compute the environment approximation, we contract the PEPS using the corner transfer matrix renormalization group (CTMRG), as suggested in [197]. To explain this method, let a and b be the reduced tensors

$$a = \sum_{s=1}^{d} A_s \otimes A_s^{\star}, \tag{54}$$

$$b = \sum_{s=1}^{d} B_s \otimes B_s^{\star}, \tag{55}$$

with double bond indices such as $\bar{u} = (u, u')$. Then, the scalar product $\langle\psi|\psi\rangle$ can be expressed as a two-dimensional network $\epsilon(\boldsymbol{x}_1, \boldsymbol{x}_2)$ made of infinitely many copies of a and b (see Fig. 8**(a)**). The exact environment of sites $\boldsymbol{x}_1$ and $\boldsymbol{x}_2$ is obtained for $\epsilon\ (\boldsymbol{x}_1, \boldsymbol{x}_2)$ by removing the tensors a and b, as shown in Fig. 8**(b)**. The goal of the CTM method is to compute an approximation $\mathscr{G}\ (\boldsymbol{x}_1, \boldsymbol{x}_2)$ to $\epsilon\ (\boldsymbol{x}_1, \boldsymbol{x}_2)$ by finding the fixed point of the four CTMs. This effective environment is given in terms of a set of four $\chi \times \chi$ corner transfer matrices $\{C_1, C_2, C_3, C_4\}$, eight half transfer row/column tensors $\left\{T_{a_1}, T_{a_2}, T_{a_3}, T_{a_4}, T_{b_1}, T_{b_2}, T_{b_3}, T_{b_4}\right\}$ and the two tensors a and b (see Fig. 8**(c)**). The twelve tensors of $\mathscr{G}\ (\boldsymbol{x}_1, \boldsymbol{x}_2)$ are updated according to four directional coarse-graining moves, namely left, right, up and down moves, which are iterated until the environment converges. Given an effective environment $\mathscr{G}\ (\boldsymbol{x}_1, \boldsymbol{x}_2)$ a move, e.g. to left, consists to the following three main steps:

- **Insertion:** Insert a new column made of tensors T_{b_1}, a, b and T_{a_3} (see Fig. 8**(d)**).
- **Absorption:** Contract tensor C_1 and T_{b_1}, tensor C_4 and T_{a_3}, tensor T_{b_4} and a, and also the tensor T_{a_4} and b, resulting in two new CTMs $\tilde{C}_1$ and $\tilde{C}_2$ and two new transfer tensors $\tilde{T}_{a_4}$ and $\tilde{T}_{b_4}$, represented by shaded green areas in Fig. 8**(d)**).
- **Renormalization:** The renormalization step requires introducing two isometries Z and W. This produces renormalized CTM's $C_1' = Z^{\dagger}\tilde{C}_1$, $C_4' = Z^{\dagger}\tilde{C}_4$ and half-raw transfer matrices T_{a_4}' and T_{b_4}' (see Figs. 8 **(g)–(i)**).

A proper choice of the isometries Z in the renormalization step is of great importance. Here, we consider instead the eigenvalue decomposition of $\tilde{C}_1\tilde{C}_1^{\dagger} + \tilde{C}_1\tilde{C}_1^{\dagger} = \tilde{Z}D_z\tilde{Z}^{\dagger}$ (see first equation of Fig. 8**(e)**), and use the isometry Z that results from keeping to entries of $\tilde{Z}$ corresponding to the χ largest eigenvalues of D_z. Instead, for the isometry W, we decompose $\tilde{Q}_1 + \tilde{Q}_1^{\dagger} + \tilde{Q}_4 + \tilde{Q}_4^{\dagger} = \tilde{W}D_w\tilde{W}^{\dagger}$ (see second equation of Fig. 8**(f)**). The numerical cost of implementing these steps scales with D and χ as $O(D^6\chi^3)$. The net result is a new effective environment $\mathscr{G}'$ for sites $\boldsymbol{x}_1$ and $\boldsymbol{x}_2$. By composing the four moves of the directional CTMs, we can recover one iteration of the CTMRG.

(ii) Tensor optimization: To find the optimal tensors $\tilde{A}$ and $\tilde{B}$ after a single step of imaginary-time evolution, we have to minimize the distance in Eq. (53). We proceed as follows:

- We fix tensor $\tilde{B}$ to some initial tensor or, alternatively, to the tensor obtained from the previous iteration. In order to find $\tilde{A}$, we rewrite Eq. (53) as a quadratic scalar expression for the tensor, namely

$$d(\tilde{A}, \tilde{A}^{\dagger}) = \tilde{A}^{\dagger}R\tilde{A} - \tilde{A}^{\dagger}S - S^{\dagger}\tilde{A} + T \tag{56}$$

  where R, S, and T can be obtained from the appropriate tensor contractions including the effective environment around the r-link.
- We then find the minimum of $d(\tilde{A}, \tilde{A}^{\dagger})$ with respect to $\tilde{A}^{\dagger}$, which is given by $\tilde{A} = R^{-1}S$.
- Next, we fix the tensor $\tilde{A}$, and search for an optimal $\tilde{B}$ using the corresponding procedure described in the two previous steps.

The above steps are iterated until the cost function $d\left(\tilde{A}, \tilde{B}\right)$ converges to a sufficiently small value, which can be set to a specific desired value in the algorithm. Once the optimal tensors are found, these are replaced over the entire lattice considering the four-site unit cell layout, which thus approximates simultaneously the effect of all the gates g acting over the infinitely-many links of

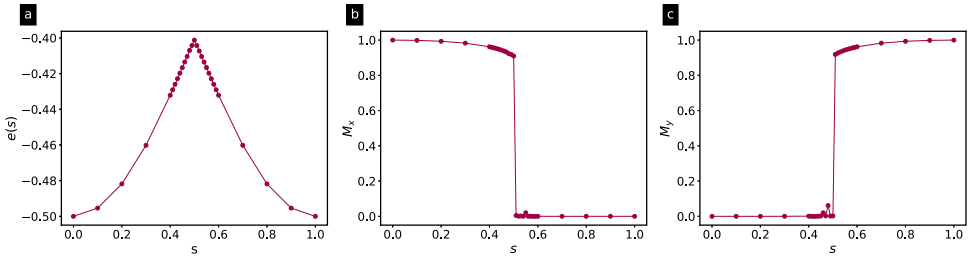

Fig. 9. Magnetizations and magnetic susceptibilities: **(a)** Ferromagnetic magnetization along the y direction for fixed coupling strength $J_y = 1$, and for different couplings J_x and magnetic fields h. The system develops a non-zero expectation value for transverse fields below a critical value $h < h_c$. In the inset, we show the magnetic susceptibility χ_{M_x} for the same parameters, which develops peaks at those critical points. **(b)** Paramagnetic magnetization along the z direction. In the inset, we show the magnetic susceptibility χ_{M_z}, which shows peaks that coincide with those of **(a)**.

the same type, here r links. Such a procedure defines the updated infinite PEPS $|\psi_{\tilde{A},\tilde{B}}\rangle$ in terms of the two new tensors. Finally, the same procedure is repeated for the l-, u- and d-links to complete one full step of imaginary-time evolution. These steps can then be concatenated until we reach the stationary state that approximates the groundstate within the PEPS family with a specific accuracy.

3.3.3. Quantum compass phase transitions

In this section, we show the results obtained by using the above iPEPS algorithm to compute the groundstate $|\Psi_{GS}\rangle$ of the 90° compass model H_{eff} (31) in a non-vanishing transverse field, working directly in the infinite-lattice limit. In particular, we have computed the ground state wave function $|\psi_{GS}\rangle$ of the system by performing the imaginary-time evolution for different values of the spin couplings J_x, J_y and the transverse magnetic field h, and then evaluated observable quantities on it, such as the groundstate energy and the local order parameters related to the aforementioned ferromagnetic phases.

In the following, we benchmark our PEPS numerical routine by fixing the bond dimension to $D = 2$ and setting $h = 0$. As shown in [180] for the zero-field limit $h = 0$, iPEPS with $D = 2$ already yields better results than those obtained by combining fermionization with mean-field theory [179]. As discussed in this reference, the values of the groundstate energy per bond agree with those obtained through a rough extrapolation to the thermodynamic limit of exact diagonalization and Green's function Monte Carlo results for finite systems presented in [177]. In the limit $h = 0$, as one tunes the couplings across the symmetric self-dual point $J_x = J_y$, a first-order phase transition between two gapped ferromagnetic orders occurs, i.e. $M_x = \langle \tau_x \rangle \neq 0$, when $J_x > J_y$ and $M_y = \langle \tau_y \rangle \neq 0$ when $J_y > J_x$. To study this phase transition, we will consider adimensional couplings, and restrict them to the range $J_x, J_y \in [0, 1]$ by the parametrization $J_x = \cos(s\pi/2)$ and $J_y = \sin(s\pi/2)$ with $s \in [0, 1]$. In Fig. 10**(a)**, we show the ground state energy per lattice link $e(s) = \langle \Psi_{GS}|H_{\text{eff}}|\Psi_{GS}\rangle/2N_1N_2$. Our results show the presence of a sharp kink at $s = 1/2$, which is compatible with the existence of a first order phase transition at $J_x = J_y$, and agrees with the numerical results presented in [180]. Other indicators for this phase transition are the magnetization $M_x = \langle \Psi_{GS}|\tau^x|\Psi_{GS}\rangle$ and $M_y = \langle \Psi_{GS}|\tau^y|\Psi_{GS}\rangle$ displayed in Fig. 10**(b)–(c)**, which show a clear discontinuity at $s = 1/2$ that separates the FM_x and FM_y phases that where identified with our mean-field ansatz. We interpret this fact as conclusive evidence of the existence of a first order phase transition, which agree with the results presented in [180], and thus gives compelling evidence for the validity of our iPEPS routine. Having benchmarked this limit, let us now switch on the transverse magnetic field to a non-zero value $h > 0$, which favours a paramagnetic phase PM with all spins pointing along the z-axis.

In contrast to the $h = 0$ limit, the transverse-field compass model has not been studied so thoroughly. In the previous section, we used a mean-field ansatz to predict a critical line (46) separating the symmetry-broken orbital ferromagnets from this paramagnet via second-order phase transitions. These critical lines are represented by green lines in Fig. 6. In order to test the validity

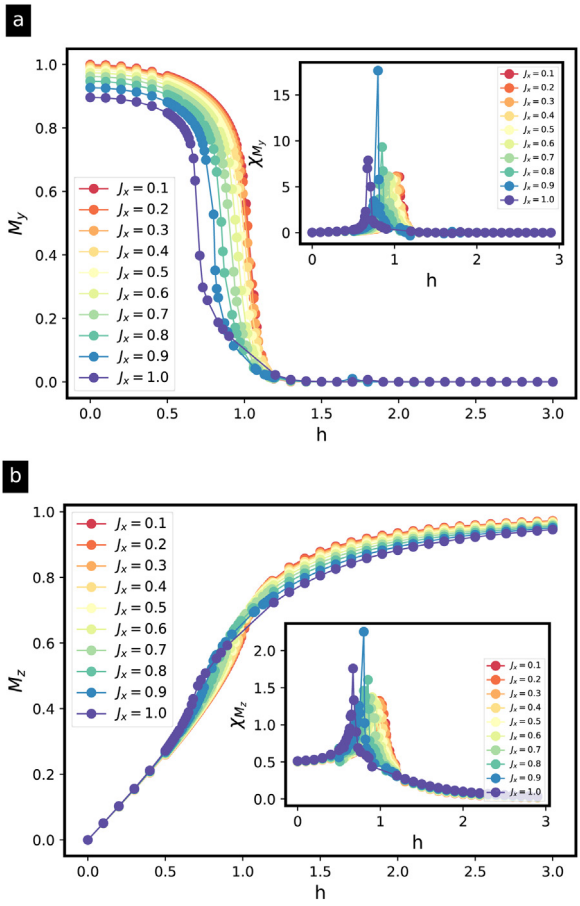

Fig. 10. First-order phase transition in the zero-field 90° compass model: **(a)** Energy of the groundstate per link $e(s)$ on an infinite square lattice obtained by using the iPEPS algorithm with $D = 2$. The energy $e(s)$ has a sharp kink with a discontinuous first derivative, signalling the first-order nature of the transition. **(b)–(c)** Expectation values of the local order parameters $M_x = \langle \tau^x \rangle$ and $M_y = \langle \tau^y \rangle$ for the ground state $|\psi_{GS}(s)\rangle$, which clearly display a discontinuity at the self-dual point $J_x = J_y$ for $s = 1/2$, marking the occurrence of a first-order phase transition.

of these mean-field predictions, we use our iPEPS algorithm for $D = 2$ with the hope that, as occurs for the $h = 0$ limit, it will also give a quantitatively-better account of this second-order phase transition than the previous mean-field ansatz. By measuring the paramagnetic and ferromagnetic magnetizations, we confirm that these quantities can be used to identify the critical points also for a non-zero magnetic field $h > 0$. In Fig. 9**(a)**, we present the magnetization $M_y = \langle \tau^y \rangle$ as a function of the transverse magnetic field h, setting $J_y = 1$ and exploring different values of $J_x < 1$. This figure shows that, for weak transverse fields, the magnetization attains a non-zero value that signals a symmetry-broken FM_y. In the inset, we show that the corresponding magnetic susceptibility $\chi_{M_y} = \partial M_y / \partial h$ peaks at a specific value of the transverse field, which can be used to locate the corresponding critical points. This flow of the FM_y-PM critical point $h/J_y|_c$ as a function of J_x is to be expected, as the $J_x \to 0$ limit corresponds to a set of decoupled rows, each of which chain with a well-known critical point $h/J_y|_c = 1$ [198]. We find that, as $J_x \to J_y = 1$, the critical point shifts towards $h/J_y|_c = 0.7$. In Fig. 9**(b)**, we depict the transverse magnetization $M_z = \langle \tau^z \rangle$, which is not an order parameter of the model, and can display a non-zero value for arbitrary value

of the couplings, saturating at $M_z = 1$ when all spins are perfectly aligned with the z axis for $h \gg 1$. In the inset, we represent the susceptibility $\chi_{M_z} = \partial M_z / \partial h$, which peaks at the transition points, in analogy to the transverse-field Ising chain.

Let us now discuss how these results can be applied to recover the iPEPS analogue of the strong-coupling mean-field critical lines in Eq. (46). Note that, according to Eq. (32), the ratio of the spin couplings is set by the lattice anisotropy $J_x/J_y = (a_1/a_2)^2 = \xi_2^2$. In Fig. 2, we consider the planes in parameter space for $\xi_2 = 1$, and $\xi_2 = 1/2$, such that $J_x/J_y = 1$, and $J_x/J_y = 1/4$ respectively. For this particular ratio, our iPEPS algorithm for $D = 2$ estimates the critical points at $h/J_y|c \approx 0.7$ and $h/J_y|c \approx 1.07$, respectively. Note that there is a large deviation in both cases with respect to the corresponding mean-field prediction $h/J_y|_c = 2$. Using the expressions for the transverse field and spin coupling strength in terms of the microscopic parameters of the four-Fermi–Wilson model (32), we obtain a pair of critical lines that are represented by the red lines in Fig. 17 **(a)–(b)** below. As can be seen from these results, although the analytical mean-field predictions (46) capture the correct parametric dependence of the critical lines, the iPEPS predicts a smaller region for the symmetry-broken FM_y phase. Given the fact that iPEPS treats correlations more accurately, we believe that these iPEPS result capture the correct trend and, although better estimates will be achieved by increasing the bond dimension beyond $D = 2$, the extend of the FM_y will in any case be smaller than that predicted by the mean-field ansatz. Moreover, we have checked that, for $h \neq 0$, iPEPS also provides significantly-lower variational energies than the one obtained by the separable-state mean-field ansatz, which typically under-estimates the effect of the transverse field. Future studies may take these results as a starting point, and study the specific scaling relations, shedding light into the universality class of the 90° compass model in a transverse field.

4. Auxiliary-field gap equations at large N

In the following two sections, we use an alternative tool to characterize the phase diagram of the four-Fermi–Wilson model (10). This technique will allow us to connect our discussion of the N-flavoured Chern insulators and the trivial band insulators of Section 2.3 with the ferromagnetic FM_x, FM_y and paramagnetic PM phases discussed in Sections 3.2 and 3.3. As described below, the number of flavours N will play a key role in this endeavour. We note that the inclusion of N flavours permits building QFTs with internal symmetries, as for example the $U(N)$ global symmetry of our four-Fermi QFT (1). One may expect that including more flavours would lead to further complexity and modify the properties of the QFT, as the number of coupled degrees of freedom increases with N. What can be surprising at first sight is that the limit of a very large flavour number $N \to \infty$ can actually turn out to simplify the theory and allow to explore non-perturbative effects in a controlled and well-defined framework.

A paradigm in this regard is the scalar $O(N)$ model, which generalizes the $\lambda_0 \phi^4$ field theory to N flavours interacting through a rotationally-invariant quartic term $\frac{\lambda_0}{N} \left(\sum_{\mathrm{f}} \phi_{\mathrm{f}} \phi_{\mathrm{f}} \right)^2$. Here, the increased number of flavours $N > 1$ changes the physics substantially, as the breakdown of the $O(N)$ symmetry is accompanied by the appearance of $N - 1$ massless excitations above the symmetry-broken groundstate, the Goldstone bosons [199]. In the symmetric phase, the flavour number also changes crucial aspects of this QFT, such as the renormalization-group (RG) fixed points, which yield scaling dimensions and critical exponents that generally depend on N [200,201]. This dependence is a consequence of the increased complexity: Feynman diagrams arising in perturbative RG calculations, the so-called radiative corrections [202], can have different contributions depending on how one decorates the graph with different flavour indexes. In the simplest case, one finds loops where the internal flavour index is summed over yielding a contribution that scales with N, but also other single-flavour loops with exactly the same graph structure that do not scale with N. Although this increases the complexity *a priori*, since different contributions cannot be distinguished by the topological structure of the diagrams, it is also the key for the development of large-N techniques where these QFTs actually become simpler [112]. When this scaling is combined with that of the interaction vertex, which scales with $1/N$, one can group the Feynman diagrams by their order $\mathcal{O}(1/N^\alpha)$, and retain only the leading ones for $\alpha = 0$ in the limit $N \to \infty$, and calculate corrections to this limit systematically for $\alpha \in \{1, 2, \ldots\}$. It is in this particular limit where the

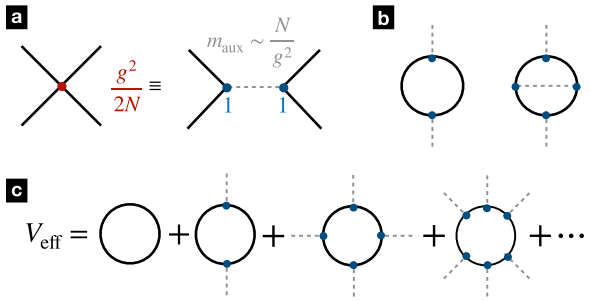

Fig. 11. Auxiliary field and large-N diagrams: **(a)** The four-Fermi vertex $g^2/2N$ (red dot) can be rewritten in terms of an auxiliary field of mass $m_{\text{aux}} \sim N/g^2$ and no kinetic energy that mediates the interaction with new vertices of order $\mathcal{O}(N^0)$ (blue dots). **(b)** 1-particle irreducible diagrams with more internal auxiliary lines, such as the second one, involve extra powers of the inverse auxiliary mass, and thus contribute with higher powers of $1/N$ that can be neglected for $N \to \infty$. **(c)** The effective potential in the large-N limit can be obtained by resumming all the Feynman diagrams obtained by a single fermion loop, and an even number of external auxiliary lines. (For interpretation of the references to colour in this figure legend, the reader is referred to the web version of this article.)

QFT becomes simpler than any finite-N instance. Moreover, these large-N methods allow one to go beyond ordinary perturbation theory in the coupling λ_0, addressing strong-coupling phenomena such as the quantum-mechanical contributions to spontaneous symmetry breaking [203,204].

For QFTs with four-Fermi terms, such as the Gross–Neveu model in (1+1) dimensions [18], the situation gets richer as, in addition to the $U(N)$ flavour symmetry, one also has chiral symmetry. Once again, Feynman diagrams in general depend on N, which can modify a perturbative RG approach [200]. However, the fermionic case introduces further possibilities, as the breakdown of chiral symmetry can occur by the process of dynamical mass generation [15]. In 1+1 dimensions, the vacuum of massless Dirac fermions is unstable towards a scalar condensate, which forms at any non-zero coupling strength $g^2 > 0$. As a consequence, the fermions acquire a mass that depends non-analytically on the coupling strength g^2, and cannot be thus captured to any finite order of perturbation theory [18]. In (2+1) dimensions, a chiral-invariant (3) Gross–Neveu model (1) still displays such a chiral symmetry breaking which, in contrast, takes place at a non-zero coupling strength $g^2 \to g_c^2$. It is in the vicinity of this strong-coupling point where one obtains a renormalizable large-N QFT, allowing for estimates of the scaling dimensions and critical exponents that improve as one increases the order α [21,110].

A convenient starting point for the large-N analysis is the introduction of an auxiliary field with zero kinetic energy and a mass that scales linearly with N. The bare propagator, represented by a dotted line in Fig. 11**(a),** scales with $1/N$ and serves to mediate the four-Fermi terms via new interaction vertices that do not scale with N. Thanks to these auxiliary fields, the Feynman diagrams with a distinct N-scaling can be readily identified, as they are now endowed with a different topological structure. For instance, the leading-order one-particle irreducible diagrams, which cannot be split in two disconnected pieces by cutting an internal line (see Fig. 11**(b)**), must minimize the number of internal propagators of the auxiliary field, as each of these is suppressed by an additional power of $1/N$, yielding sub-dominant terms in the large-N limit. As discussed in more detail below, the leading-order radiative corrections are thus formed by a single fermion loop which, due to the algebraic properties of the gamma matrices, can only be dressed by an even number of external auxiliary lines [112] (see Fig. 11**(c)**). Remarkably, the large-N radiative corrections can be resummed to all orders of the coupling strength g^2, which allows one to address non-perturbative phenomena [112], such as dynamical mass generation, chiral symmetry breaking, and dimensional transmutation in $(1+1)$ dimensions [18].

We note that in the continuum QFT (1), it suffices to introduce a single auxiliary σ field, which acquires a non-zero vacuum expectation value proportional to the scalar condensate and contributes to the fermion mass. This auxiliary σ field is an instance of the so-called Hubbard–Stratonovich fields [205,206], which allow for various mean-field approximations with applications in condensed

matter [207]. From this perspective, one typically needs to explore a variety of possible symmetry-breaking channels, which requires introducing multiple Hubbard–Stratonovich auxiliary fields. In the rest of this section, we use the results from the strong-coupling analysis to guide our choice of auxiliary fields, and show how a large-N method can provide a detailed account of the phase diagram of our four-Fermi–Wilson model (10) by functional-integral techniques. We obtain a set of non-linear equations, the gap equations, the solution of which gives access to the critical lines, as well as the symmetry-broken phases with non-zero order parameters. In the following Section 5, we shall exploit the above resummation of the leading Feynman diagrams to calculate the effective potential, which also gives us access to the symmetric regions, and in particular to a characterization of the correlated QAH phase, and the equivalence of the PM and TBI phases.

4.1. Hamiltonian field theory and gap equations

Let us start by focusing on the canonical partition function $Z = \mathrm{Tr}(\mathrm{e}^{-\beta H})$ of the four-Fermi–Wilson Hamiltonian (10), where $\beta = 1/T$ is the inverse temperature in natural units, and rewrite it as a functional integral in Euclidean time $\tau \in [0, \beta)$ [208]. We use the over-complete basis of fermionic coherent states at each point of the Brillouin zone $\boldsymbol{k} \in \mathrm{BZ}$, and introduce a set of anti-commuting Grassmann vectors $\Psi_{\boldsymbol{k}}(\tau)$, $\Psi^{\star}_{\boldsymbol{k}}(\tau)$, each of which contains 2 spinor and N flavour components, and satisfies anti-periodic boundary conditions in the imaginary-time direction $\Psi_{\boldsymbol{k}}(\tau + \beta) = -\Psi_{\boldsymbol{k}}(\tau)$, $\Psi^{\star}_{\boldsymbol{k}}(\tau + \beta) = -\Psi^{\star}_{\boldsymbol{k}}(\tau)$. The partition function can be expressed as a functional integral over these Grassmann variables

$$Z = \int [\mathrm{d}\Psi^{\star}\mathrm{d}\Psi]\mathrm{e}^{-S_E[\Psi^{\star},\Psi]}, \tag{57}$$

where we have introduced the functional integral measure $[\mathrm{d}\Psi^{\star}\mathrm{d}\Psi]$, and the Euclidean action

$$S_E = \int_0^{\beta} \mathrm{d}\tau \left(\sum_{\boldsymbol{k}\in\mathrm{BZ}} \Psi^{\star}_{\boldsymbol{k}}(\tau)\big(\partial_{\tau} + h_{\boldsymbol{k}}(m)\big)\Psi_{\boldsymbol{k}}(\tau) + V_g[\Psi^{\star}, \Psi] \right). \tag{58}$$

Here, we have used the single-particle Hamiltonian $h_{\boldsymbol{k}}(m)$ of Eq. (13), and introduced $V_g[\Psi^{\star}, \Psi]$ as the expectation value of the four-Fermi interaction (9) in such a coherent-state basis. Let us now describe how to rewrite this interaction in terms of auxiliary fields, using the strong-coupling results as a guide.

First of all, we need to consider the auxiliary σ field which, as discussed above, can attain a non-zero value proportional to the scalar condensate in a continuum QFT

$$\Sigma \propto \langle \overline{\Psi}(\boldsymbol{x})\Psi(\boldsymbol{x})\rangle. \tag{59}$$

Considering the discretized model in the single-flavour $N = 1$ limit, and the bilayer perspective of Fig. 1, this scalar condensate is simply proportional to the magnetization of the orbital spins (30) along the z-axis $\Sigma \propto \langle \tau^z_{\boldsymbol{n}}\rangle$. We know from the previous section that, for any non-zero transverse field $h \neq 0$, this magnetization is always non-vanishing, and there is thus no spontaneous symmetry breaking associated with its non-zero value. From the perspective of relativistic LFTs, the fermion masses introduced by the Wilson-type discretization (7)–(8) are responsible for the non-zero value of the σ field, and the spontaneous condensation is only expected to be recovered in the vicinity of a critical point where a continuum QFT emerges. For the particular choice of gamma matrices (3), this QFT would be endowed with an emergent chiral symmetry, and the formation of the scalar condensate is related to chiral symmetry breaking via dynamical mass generation. On the other hand, for the current choice (2), although chiral symmetry cannot be defined, the emergent QFT will have important connections to the QAH effect and the nature of the topological phase transitions discussed in Section 2.3 as one enters the strong-coupling regime.

As discussed in the previous section, regardless of the absence of chiral symmetry, there are other possible symmetry-breaking channels that can be activated by increasing the interactions of the four-Fermi–Wilson model (10). In the $N = 1$ limit, this occurs due to the spontaneous breakdown of a $\mathbb{Z}_2$ symmetry, and the appearance of the ferromagnetic long-range orders, either along the x-axis

$\langle\tau^x_{\boldsymbol{n}}\rangle$ (44), or the y-axis $\langle\tau^y_{\boldsymbol{n}}\rangle$ (45). In light of Eqs. (2) and (30), these order parameters can be readily generalized to the N-flavour case by introducing two additional auxiliary π fields $\Pi_1(\boldsymbol{x})$, $\Pi_2(\boldsymbol{x})$ and two possible π-condensates

$$\Pi_1 \propto \langle\overline{\Psi}(\boldsymbol{x})(\mathbb{I}_N \otimes \gamma^1)\Psi(\boldsymbol{x})\rangle, \quad \Pi_2 \propto \langle\overline{\Psi}(\boldsymbol{x})(\mathbb{I}_N \otimes \gamma^2)\Psi(\boldsymbol{x})\rangle. \tag{60}$$

Once again, these condensates are not related to the spontaneous breakdown of the continuous internal symmetry $U(N)$ but, instead, to inversion symmetry on the discrete lattice

$$\Psi(\boldsymbol{x}) \mapsto \big(\mathbb{I}_N \otimes \gamma^0\big)\Psi(-\boldsymbol{x}), \quad \forall \boldsymbol{x} \in \Lambda_s. \tag{61}$$

Let us note that this transformation resembles the parity symmetry of Dirac fermions in even-dimensional spacetimes [209], the breakdown of which may occur via the pseudo-scalar condensate $\Pi_5 \propto \langle\overline{\Psi}(\boldsymbol{x})(\mathrm{i}\mathbb{I}_N \otimes \gamma^5)\Psi(\boldsymbol{x})\rangle$ [210,211]. In our case, however, Eq. (61) corresponds to a planar rotation of angle $\theta = \pi$ and, as discussed in Section 6, thus belongs to the Lorentz group of continuous transformations $SO(1,2)$. To define parity in odd-dimensional spacetimes, one can search for a transformation that flips an odd number of spacetime axes, e.g. $\Psi(x_1, x_2) \mapsto (\mathbb{I}_N \otimes \gamma^2)\Psi(x_1, -x_2)$ in our case, such that the Σ and Π_2 condensates are parity-odd while Π_1 is parity-even, which follows from the Clifford algebra fulfilled by the gamma matrices. In contrast, using the inversion symmetry of Eq. (61), the homogeneous scalar condensate (59) is invariant $\Sigma \mapsto \Sigma$, whereas a non-zero value of any of the π condensates (60) breaks it $\Pi_j \mapsto -\Pi_j$, such that the π fields are treated on equal footing.

In comparison to the pseudo-scalar condensate that may arise in chiral-invariant lattice models [210,211], we find that the number of possible symmetry-breaking channels is doubled when chiral symmetry is absent from the outset (2). Moreover, at exact isotropy, any combination of the condensates $\cos\phi\Pi_1 + \sin\phi\Pi_2$ can be stabilized in the groundstate. Let us note that either of these π condensates not only breaks inversion symmetry, but also forbids the recovery of invariance with respect to specific Lorentz boosts in the long-wavelength limit. We shall thus refer to them as Lorentz-breaking condensates. Accordingly, when approaching the critical point from the symmetry-broken phases to recover the continuum QFT, the effective QFT would not be Lorentz-invariant unless we precisely hit the critical point. This would obviously change if we approach the critical point from the symmetry-preserving phase.

Before proceeding with the large-N approximation, let us discuss these auxiliary fields from the perspective of the Hubbard bilayer. Having N flavours is equivalent to stacking N Hubbard bilayers on top of each other, which only get coupled through the quartic Hubbard-type interactions. From the perspective of mean-field theory, the σ field is related to the so-called Hartree decoupling of the interactions, which introduces terms that are proportional to the densities and is thus responsible for a shift of the bare mass in Eq. (66). On the other hand, the π fields include the so-called Fock contributions, since they lead to terms that modify the inter-layer tunnelling, which is equivalent to the exchange spin-flip terms induced by the γ^1 and γ^2 matrices in the language of the orbital spins. Therefore, our large-N formalism is related to a self-consistent Hartree–Fock method in condensed-matter Hubbard-type models, and becomes exact in the limit of an infinite number of bilayers $N \to \infty$.

Once we have identified the relevant auxiliary fields, we should apply a Hubbard–Stratonovich transformation to rewrite the action (58) in terms of them. In Appendix A we show that, except for the isotropic limit $a_1 = a_2$, the two π fields cannot condense simultaneously. We can thus introduce these fields by two separate Hubbard–Stratonovich transformations, and compare the corresponding energies to determine which Π_j condensate corresponds to the groundstate in the event of a spontaneous breakdown of inversion symmetry. We thus consider the transformations of the four-Fermi term

$$(\overline{\Psi}(\boldsymbol{x})\Psi(\boldsymbol{x}))^2 \to \frac{1}{2}\Big((\overline{\Psi}(\boldsymbol{x})\gamma^1\Psi(\boldsymbol{x}))^2 + (\overline{\Psi}(\boldsymbol{x})\Psi(\boldsymbol{x}))^2\Big), \tag{62}$$

$$(\overline{\Psi}(\boldsymbol{x})\Psi(\boldsymbol{x}))^2 \to \frac{1}{2}\Big((\overline{\Psi}(\boldsymbol{x})\gamma^2\Psi(\boldsymbol{x}))^2 + (\overline{\Psi}(\boldsymbol{x})\Psi(\boldsymbol{x}))^2\Big), \tag{63}$$

both of which are exact identities in the single-flavour $N = 1$ limit. In the following calculations, we assume that the lattice translational invariance is preserved in the event of condensation, and thus consider that the auxiliary fields are homogeneous, i.e. $\Sigma(\boldsymbol{x}) = \Sigma$, $\Pi_j(\boldsymbol{x}) = \Pi_j$.

Tied to the condition that, after integrating over these auxiliary fields, the original action (58) must be recovered with the corresponding four-Fermi term (63), the transformed partition function $Z = \int [\mathrm{d}\Psi \mathrm{d}\Psi^\star \mathrm{d}\Sigma \mathrm{d}\Pi_j] \exp(-S_E[\Psi^\star, \Psi, \Sigma, \Pi_j])$ leads to an action that depends on the auxiliary fields

$$S_E = \int_0^\beta \mathrm{d}\tau \left(\frac{NA_s}{g^2} \left(\Sigma^2 + \Pi_j^2\right) + \sum_{\boldsymbol{k}\in \mathrm{BZ}} \Psi_{\boldsymbol{k}}^\star(\tau) \Big(\partial_\tau + h_{\boldsymbol{k}}(m + \Sigma, \Pi_j) \Big) \Psi_{\boldsymbol{k}}(\tau) \right), \tag{64}$$

where the single-particle Hamiltonian (13) gets modified to

$$h_{\boldsymbol{k}}(m) \to h_{\boldsymbol{k}}(m + \Sigma, \Pi_j) = \mathbb{I}_N \otimes \big(\boldsymbol{d}_{\boldsymbol{k}}(m + \Sigma, \Pi_j) \cdot \boldsymbol{\sigma} \big). \tag{65}$$

Here, the vector (14) whose winding is related to the Chern number of the QAH phase (20), also gets modified $\boldsymbol{d}_{\boldsymbol{k}}(m) \to \boldsymbol{d}_{\boldsymbol{k}}(m + \Sigma, \Pi_j)$ due to the presence of the auxiliary field

$$\boldsymbol{d}_{\boldsymbol{k}}(m + \Sigma, \Pi_j) = \boldsymbol{d}_{\boldsymbol{k}}(m) + \Pi_j \boldsymbol{e}_j + \Sigma \boldsymbol{e}_3, \tag{66}$$

where we remark that the two cases $j = 1, 2$ are considered separately since, as shown in Appendix A, the π fields do not condense simultaneously for generic anisotropies.

Since we are interested in quantum phase transitions, we consider the zero-temperature limit in which $\tau \in [0, \infty)$. By using a Fourier transform in imaginary time, we introduce the so-called Matsubara frequencies $\omega_{n_0} = \frac{(2n_0+1)\pi}{\beta}$ with $n_0 \in \mathbb{Z}$, which become continuous variables in this limit, spanning the range $\omega \in (-\infty, \infty)$. Performing a series of Gaussian integrals over the Grassmann variables [208], the Euclidean action can be expressed as $S_E = \beta A_s N \mathrm{s}_E$, where the action per unit 'volume' and fermion flavour is

$$\mathrm{s}_E = \frac{1}{g^2} \left(\Sigma^2 + \Pi_j^2 \right) - \int_{\omega, \boldsymbol{k}} \log\big(\omega^2 + \epsilon_{\boldsymbol{k}}(m + \Sigma, \Pi_j)^2 \big). \tag{67}$$

Here, we have introduced $\int_{\omega,\boldsymbol{k}} = \int_\omega \int_{\boldsymbol{k}} = \int_{\mathbb{R}} \frac{\mathrm{d}\omega}{2\pi} \int_{\mathrm{BZ}} \frac{\mathrm{d}^2 k}{4\pi^2}$, and the dispersion relation modified by the auxiliary fields

$$\epsilon_{\boldsymbol{k}}(m + \sigma, \Pi_j) = \| \boldsymbol{d}_{\boldsymbol{k}}(m + \Sigma, \Pi_j) \| . \tag{68}$$

We thus observe that the Euclidean action is proportional to the flavour number, which plays the role of an inverse Planck's constant $\hbar_{\mathrm{eff}} \propto 1/N$. Accordingly, the large-N limit implies $\hbar_{\mathrm{eff}} \to 0$, such that the quantum fluctuations of the auxiliary fields are suppressed, and the partition function can be approximated by its saddle point, and determined by

$$\left. \frac{\partial \mathrm{s}_E}{\partial \Sigma} \right|_{\Sigma, \Pi_j} = \left. \frac{\partial \mathrm{s}_E}{\partial \Pi_j} \right|_{\Sigma, \Pi_j} = 0. \tag{69}$$

These saddle-point equations lead to the so-called gap equations, a system of non-linear equations which, upon using contour-integration over the Matsubara frequencies, read

$$\frac{\Sigma}{g^2} = \frac{1}{2} \int_{\boldsymbol{k}} \frac{m + \Sigma + m_W(\boldsymbol{k})}{\epsilon_{\boldsymbol{k}}(m + \Sigma, \Pi_j)}, \tag{70}$$

$$\frac{\Pi_j}{g^2} = \frac{1}{2} \int_{\boldsymbol{k}} \frac{\frac{1}{a_j} \sin(k_j a_j) + \Pi_j}{\epsilon_{\boldsymbol{k}}(m + \Sigma, \Pi_j)}, \tag{71}$$

where the contribution of the Wilson term (7) to the mass is encoded in the following expression

$$m_W(\boldsymbol{k}) = \frac{1}{a_1} \Big(1 - \cos(k_1 a_1) \Big) + \frac{1}{a_2} \Big(1 - \cos(k_2 a_2) \Big). \tag{72}$$

In this section and the following one, the main goal is to determine the phase boundary separating the various phases of matter that have been discussed so far, namely the QAH, TBI, FM_x,

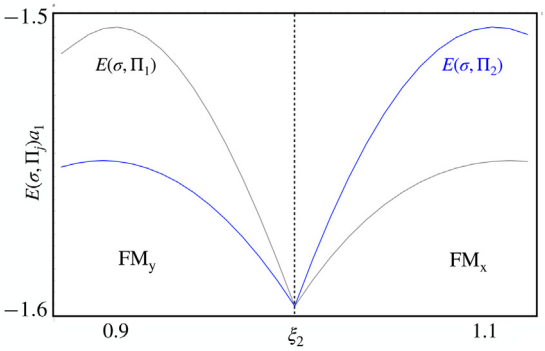

Fig. 12. Preferred Lorentz-breaking channel: The groundstate energies (73) for the two possible symmetry-breaking channels are represented as a function of the spatial anisotropy $\xi_2 = a_1/a_2$ for $ma_1 = -2$ and $g^2/a_1 = 5$. For $a_1 > a_2$, the Π_1 condensate is preferred, whereas for $a_2 > a_1$, the Π_2 condensate dominates. These correspond, respectively, to the FM$_x$ and FM$_y$ phases identified in the strong-coupling limit.

FM$_y$ and PM phases. As will be discussed below, the TBI and PM phases are actually adiabatically connected, and can thus be described as different limits of the same phase. To determine the critical lines delimiting the ferromagnetic phases, we would need to find the points where the above equations are fulfilled, and the π fields go to zero $\Pi_j = 0$ starting from the corresponding symmetry-broken phases. Note that, in practice, one divides Eq. (71) by the corresponding value of the Π_j condensate, such that there are divergences associated to the $\Pi_j = 0$ point. However, one can get as close to this point as required by the accuracy with which the critical points are to be determined. In order to draw the $(ma_1, \xi_2, g^2/a_1)$ phase diagram in analogy to Fig. 6, we perform the integrals that appear in the gap equations numerically, and vary the vacuum expectation values of the auxiliary fields Σ, Π_j until the above equations are fulfilled. Since we always get the combination $M = m + \Sigma$ in the equations, we start by assigning a value to M for a given coupling strength g^2 and lattice anisotropy $\xi_2 = a_1/a_2$, and then solve the self-consistent equations (71) to find the values of Π_j.

Once this is done, we can solve Eq. (70) to find the scalar condensate Σ, and finally extract the corresponding mass m. Note however that we have two potential solutions $(\Pi_1, 0)$ and $(0, \Pi_2)$, and we must determine which of the two possible π-condensates occurs depending on the specific anisotropy, i.e. $a_1 > a_2$ or $a_2 > a_1$. The preferred symmetry-breaking channel can be determined by comparing the two groundstate energies $j \in \{1, 2\}$ per unit area and flavour number at a certain point in the $(ma_1, \xi_2, g^2/a_1)$ parameter space

$$E(\sigma, \Pi_j) = \frac{1}{g^2}\left(\Sigma^2 + \Pi_j^2\right) - \int_{\boldsymbol{k}} \mathrm{d}^2k \epsilon_{\boldsymbol{k}}(m + \Sigma, \Pi_j). \tag{73}$$

This energy consists of the single-particle terms integrated over the Brillouin zone, and thus assumes a half-filled system with homogeneous auxiliary-field terms. By finding the two solutions for a chosen anisotropy, one can evaluate equation (73) numerically in both cases, and figure out which channel has the lower groundstate energy. We note that this procedure is non-trivial since the $(ma_1, \xi_2, g^2/a_1)$ point of parameter space is not completely set from the start, but found recursively from the numerical routine just discussed. The numerical comparison of both channels requires an exhaustive numerical analysis to find sufficient solutions to densely cover the parameter space, which can then be compared. As shown in Fig. 12, we have found that the dominant order parameter is $\Pi_1 \propto \langle\overline{\Psi}(\boldsymbol{x})(\mathbb{I}_N \otimes \gamma^1)\Psi(\boldsymbol{x})\rangle$ if $a_2 < a_1$, and $\Pi_2 \propto \langle\overline{\Psi}(\boldsymbol{x})(\mathbb{I}_N \otimes \gamma^2)\Psi(\boldsymbol{x})\rangle$ if $a_2 > a_1$, which is consistent with the results found for the variational mean-field and iPEPs methods applied to the quantum compass model in the strong-coupling and single-flavour regimes.

Let us now present a detailed discussion of our findings by analysing the two exemplary plots of the critical lines presented in Fig. 13, which explore the role of interactions along the two vertical

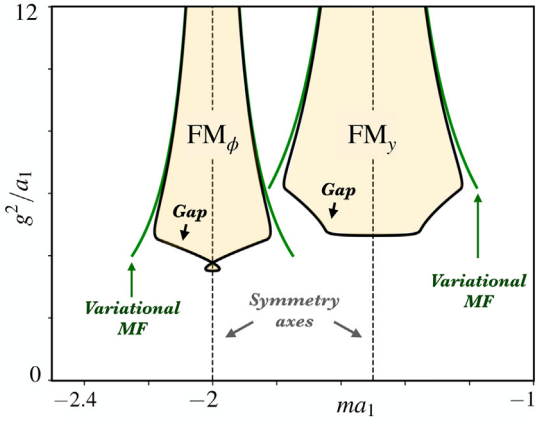

Fig. 13. Phase diagram with Lorentz-breaking condensates: The left figure represents the critical points predicted by the large-N calculation (black), and those obtained by the variational mean-field ansatz (green), both of which display a vertical symmetry line at $ma_1 = -2$ for the isotropic case $\xi_2 = 1$. The right figure represents the critical points in the anisotropic case $\xi_2 = 0.5$ with the vertical symmetry line at $ma_1 = -1.5$. (For interpretation of the references to colour in this figure legend, the reader is referred to the web version of this article.)

planes of Fig. 2. In these plots, the black solid lines correspond to the critical points obtained from the solution of the gap Eqs. (70)–(71). The region inside this black line represents the inversion-broken phases. The left black solid line in Fig. 13 corresponds to the isotropic case $a_1 = a_2$, where no comparison is required as both equations–(71) for $j = 1, 2$ are equivalent. In close similarity to the variational compass-model result, this point is special in the sense that we cannot determine which linear combination $\cos\phi\Pi_1 + \sin\phi\Pi_2$ is the correct order parameter, which is the situation found in Eqs. (37)–(38) by setting the exchange couplings (32) to $J_x = J_y$ for equal $a_1 = a_2$. This thus corresponds to the large-N version of the FM_ϕ phase. In contrast, the right black solid line of Fig. 13 represents the critical line for lattice spacings $a_1 = a_2/2$, where we have found that the enclosed region hosts a non-zero value of the Π_2 condensate, energetically preferred with respect to the Π_1 condensate (see Fig. 12). As we keep on decreasing the ratio $\xi_2 = a_1/a_2$, this region moves progressively to the upper right, such that the appearance of the inversion-broken regions occurs for smaller absolute values of the bare mass and larger interaction strengths. Although not shown in this figure, for opposite anisotropies $a_2 < a_1$, this behaviour is reversed, as we have found that the symmetry-broken Π_1 condensates move to the left, and thus seek larger absolute values of the bare mass and smaller interaction strengths.

We note that both ordered phases reflect mirror symmetry of the gap equations around the symmetry axis $m = -\frac{1}{a_1} - \frac{1}{a_2}$, which is depicted by a dashed line. In the language of the strong-coupling compass model (32), this symmetry corresponds to the vanishing of the transverse field $h = 0$, which is achieved within the symmetry plane of Fig. 6. We note that the σ field and, with it, the scalar condensate vanish along this symmetry line $\langle\overline{\Psi}\Psi\rangle \propto \Sigma = 0$. As discussed in more detail below, this cancels the additive mass renormalizations arising from the fermion doublers. This feature is not a large-N artefact, but actually connects to the so-called central-branch Wilson fermions, which have interesting implications for Monte Carlo studies of lattice gauge theories [212,213].

In Fig. 13, we also represent in green solid lines the critical points (46) obtained by the variational mean-field ansatz of the 90° compass model in a transverse field (31) with microscopic parameters (32). It is quite remarkable to see that these two predictions match so well as one increases the interactions, since they emerge from completely different mean-field perspectives. In order to compare them, let us rewrite the strong-coupling 90° compass model (31) as an effective action that depends solely on the auxiliary fields. Considering the corresponding Euler–Lagrange

equations

$$\sigma(\boldsymbol{x}) = -\frac{g^2}{2}\overline{\Psi}(\boldsymbol{x})\Psi(\boldsymbol{x}), \quad \pi_j(\boldsymbol{x}) = -\frac{g^2}{2}\overline{\Psi}(\boldsymbol{x})\gamma^j\Psi(\boldsymbol{x}), \tag{74}$$

the compass Hamiltonian leads to an action with nearest-neighbour couplings

$$S_{\text{eff}} = \int \mathrm{d}x^0 a_1 a_2 \sum_{\boldsymbol{x}\in\Lambda_s} \Big(\tilde{J}_1 \pi_1(\boldsymbol{x})\pi_1(\boldsymbol{x}+a_2\boldsymbol{e}_2) + \tilde{J}_2 \pi_2(\boldsymbol{x})\pi_2(\boldsymbol{x}+a_1\boldsymbol{e}_1) + h\sigma(\boldsymbol{x}) \Big), \tag{75}$$

where we have introduced the adimensional nearest-neighbour couplings for the π fields $\tilde{J}_1 = (a_1/g^2)^2$ and $\tilde{J}_2 = (a_2/g^2)^2$, whereas the coupling h to the σ field has the dimension of mass and corresponds directly to the transverse field in Eq. (32). This action clearly differs from the effective Euclidean action obtained in the large-N approximation after integrating over the fermionic fields (67). To compare both expressions on equal footing, we note that the real-space version of Eq. (67) would be expressed in terms of the logarithm of a fluctuation determinant, which is highly non-local in contrast to Eq. (75). On other hand, the Euler–Lagrange constraints (74) together with the Gutzwiller projector onto singly-occupied sites mentioned below Eq. (32), imply that the σ and π fields in Eq. (75) are not independent, but rather constrained to

$$\sigma^2(\boldsymbol{x}) + \pi_1^2(\boldsymbol{x}) + \pi_2^2(\boldsymbol{x}) = \left(\frac{g^2}{a_1 a_2}\frac{1}{2}\boldsymbol{\tau}_n\right)^2 = \frac{3}{4}\left(\frac{g^2}{a_1 a_2}\right)^2. \tag{76}$$

A simple rescaling of these auxiliary fields shows that, for the compass model, they are constrained to lie on the unit sphere S_2. Note that this type of strong-coupling constraint also arises in the aforementioned $O(N)$ models [200,201], which in the case of $N = 3$ flavours leads to the $O(3)$ non-linear sigma model as one takes the strong-coupling limit $\lambda_0 \to \infty$. By contrast, the compass action (75) can be understood as an anisotropic discretized version of a non-linear sigma model with a $\mathbb{Z}_2$ inversion symmetry $(\sigma(\boldsymbol{x}), \boldsymbol{\pi}(\boldsymbol{x})) \mapsto (\sigma(-\boldsymbol{x}), -\boldsymbol{\pi}(\boldsymbol{x}))$ instead of the continuous $O(3)$ symmetry. This is a generalization of the rotationally-invariant Heisenberg spin model, which is known to be discretizations of the $O(3)$ non-linear sigma model [214,215].

The agreement of these two different mean-field methods serves as a partial benchmark of both approaches, and hints to the validity of the conclusions drawn from Fig. 13: the non-interacting QAH and TBI phases of Section 2.3 will eventually disappear in favour of the symmetry-broken ferromagnetic phases or the paramagnetic phases of Sections 3.2 and 3.3. The solution of the gap equations tells us precisely for which bare parameters the spontaneous breakdown of inversion symmetry, and the formation of the condensates, will take place. As shown in the figure, we can thus extend the strong-coupling predictions to the regime of intermediate interactions, and find the whole extent of the critical line that surrounds the orbital FM_x and FM_y phases. Additionally, since there is no critical line that separates the orbital PM and the TBI, we can conclude that both states are limiting cases of the same phase.

Let us note that, in contrast to our previous results for the Gross–Neveu–Wilson model in (1+1) dimensions [131], the critical lines obtained from the gap equations do not extend towards the region of low interactions $g^2/a_1 \approx 0$, where the weakly-correlated QAH phase is expected to be. Therefore, we cannot use them to delimit the regions with different topological phases characterized by opposite Chern numbers (23), nor the transitions to the disordered PM or the trivial band insulating TBI phases. In order to overcome these limitations, we need to explore regions of the phase diagram where the π fields are zero, and estimate the topological invariant for this large-N approximation. We will show in Section 5 that the effective potential [203,204] plays a key role in this regard. Moreover, it will allow us to explore the small lobe that forms in the symmetry-broken region around the symmetry axis for $a_1 = a_2$ which, although not shown in the figure, persists for small spatial anisotropies $a_1 \approx a_2$. The effective potential will allow us to explore this region further, and connect it to a first-order phase transition rather than a second-order one.

However, the effective potential is most naturally formulated for a Euclidean lattice where imaginary time is also discretized. In the following subsection, in order to know how to recover the

continuum-time limit from this Euclidean-lattice formulation, we will analyse the results of the gap equations for a Euclidean lattice, and show that there can be additional additive renormalizations. These contributions must be carefully accounted for if one aims to describe the physics of a correlated QAH effect, which is ultimately defined in the continuum-time limit. Equipped with these results, we will be able to formulate in Section 5 a description for the effective potential that allows us to fully characterize the phase diagram.

4.2. Large-N gap equations on the Euclidean lattice

In the LFT community, the discretization is an artificial scaffolding for the fields that serves to regularize the QFT, but has no physical reality. Accordingly, the imaginary time can also be discretized, such that spacetime coordinates are treated on equal footing [19,20]. In the present context, the rectangular spatial lattice (5) must be upgraded to include the discretized time with yet another lattice spacing. This leads to a simple orthorhombic Bravais lattice defined by

$$\Lambda_E = \{(n_0 a_0, n_1 a_1, n_2 a_2) : n_\alpha \in \mathbb{Z}_{N_\alpha},\ \forall \alpha \in \{0, 1, 2\}\} \tag{77}$$

where N_α is the number of sites along the α-axis with lattice spacing a_α, such that the Euclidean 'volume' is $Q = \prod_\alpha N_\alpha a_\alpha$. We note that higher-dimensional versions of these anisotropic lattices have been exploited in the context of lattice gauge theories. If one is interested in the time-continuum limit and the connection to Hamiltonian field theories, as in our work, the temporal anisotropy is mandatory [216,217]. Moreover, using a smaller temporal lattice spacing sometimes allows for a higher precision in Monte Carlo calculations [218–223]. Interestingly, one can also get improvements by exploiting the anisotropy along the spatial directions [224]. In the context of the domain-wall-fermion approach [51], one of the spatial directions is considered as an auxiliary dimension, such that a pair of distant domain-wall profiles of the bare mass allows one to recover a QFT of chiral fermions for anisotropic volumes in which the wall separation is sufficiently large, which can be exploited for studies on chiral-invariant four-Fermi models [225–227]. If the anisotropy occurs at the level of the lattice spacings rather than the volume, one can also formulate domain-wall fermions by abruptly changing the lattice spacing values in a particular location of the auxiliary dimension [135].

A possible advantage of formulating the four-Fermi–Wilson model with a discrete time is that future studies may use the extensive LFT machinery based on Monte Carlo simulations to corroborate our predictions beyond the large-N or strong-coupling limits. Despite the infamous sign problem for fermions, which plagues many Monte Carlo simulations, unless one is interested in doping our system above/below half filling, the Monte Carlo update schemes should give reliable results. However, one should be careful with the interpretation of these results in the context of QAH phases and the phase diagram of topological materials. Whereas the spatial discretization is imposed by the underlying crystal, the time discretization is a computational artifact, and the physics should be extracted by taking a continuum-time limit. This limit is not recovered by simply sending the corresponding lattice spacing $a_0 \to 0$, as the time discretization introduces spurious (time)doublers [20]. These will affect the theory, as they carry their own Wilson masses, such that one would expect the topological invariant (21) to be modified if this continuum-time limit is not considered carefully. As will be shown in this section, in order to recover the results of the continuum-time gap Eqs. (70) and (71), there are additive renormalizations that must be carefully considered.

Let us start by formulating the problem on the Euclidean cubic lattice (77). Here, we use fermionic coherent states and Grassmann vectors $\Psi_{\boldsymbol{x}}, \overline{\Psi}_{\boldsymbol{x}}$ for all Euclidean spacetime points $\boldsymbol{x} \in \Lambda_E$, each containing both flavour and spinor components, and respecting periodic (antiperiodic) boundary conditions along the spatial (time) directions. The partition function can be expressed by a functional integral $Z = \int [\mathrm{d}\Psi^\star \mathrm{d}\Psi] e^{-S_E[\Psi^\star, \Psi]}$ with the following Euclidean action

$$S_E[\Psi^\star, \Psi] = a_0 a_1 a_2 \left(S_E^0[\Psi^\star, \Psi] + V_g[\Psi^\star, \Psi] \right). \tag{78}$$

The free Wilsonian action in the Euclidean lattice reads

$$S_E^0[\Psi^\star,\Psi] = \sum_{\boldsymbol{x}\in\Lambda_E}\overline{\Psi}_{\boldsymbol{x}}\Big(m+\sum_\alpha\frac{1}{a_\alpha}\Big)\Psi_{\boldsymbol{x}} + \sum_{\boldsymbol{x}\in\Lambda_E}\sum_\alpha\sum_{s=\pm1}\overline{\Psi}_{\boldsymbol{x}}\left(\frac{s(\mathbb{I}_N\otimes\tilde{\gamma}_\alpha)}{2a_\alpha}-\frac{1}{2a_\alpha}\right)\Psi_{\boldsymbol{x}+sa_\alpha\boldsymbol{e}_\alpha}, \tag{79}$$

where the Euclidean gamma matrices are

$$\tilde{\gamma}_0=\gamma^0=\sigma^z,\quad \tilde{\gamma}_1=-\mathrm{i}\gamma^1=\sigma^y,\quad \tilde{\gamma}_2=-\mathrm{i}\gamma^2=-\sigma^x, \tag{80}$$

and satisfy Clifford's algebra $\{\tilde{\gamma}_\alpha,\tilde{\gamma}_\beta\}=2\delta_{\alpha\beta}$ for the Euclidean metric $\delta=\mathrm{diag}(1,1,1)$. In order to introduce the auxiliary fields, we consider the results of the previous section, and only consider a single π-channel. In the following, all calculations are presented for the $\tilde{\gamma}_2$ interaction corresponding to the Π_2 condensate, as this is the symmetry-breaking channel for $\xi_2<1$. Note, however, that there is no conceptual difference for the calculations for the $\tilde{\gamma}_1$ channel. The four-Fermi term on the Euclidean lattice reads

$$V_g[\Psi^\star,\Psi]=\frac{-g^2}{4N}\sum_{\boldsymbol{x}\in\Lambda_E}\left((\overline{\Psi}_{\boldsymbol{x}}\Psi_{\boldsymbol{x}})^2+(\overline{\Psi}_{\boldsymbol{x}}\mathrm{i}\tilde{\gamma}_2\Psi_{\boldsymbol{x}})^2\right). \tag{81}$$

We now formulate this problem using dimensionless fields $\tilde{\Psi}_{\boldsymbol{x}}$, which can be defined as

$$\Psi_{\boldsymbol{x}}=(a_0a_1+a_1a_2+a_0a_2)^{-\frac{1}{2}}\,\tilde{\Psi}_{\boldsymbol{x}}, \tag{82}$$

and likewise for the adjoints $\overline{\tilde{\Psi}}_{\boldsymbol{x}}$. This makes direct contact with the standard formulations based on Wilson fermions in LFTs [20,228]. Similar to the continuous-time field theory (58), the quadratic terms can be diagonalized by going to $\boldsymbol{k}$-space, $S_E^0=\sum_{\boldsymbol{k}}\overline{\tilde{\Psi}}_{\boldsymbol{k}}S_{\boldsymbol{k}}^0(\tilde{m})\tilde{\Psi}_{\boldsymbol{k}}$, where

$$S_{\boldsymbol{k}}^0(\tilde{m})=\mathbb{I}_N\otimes\left(\tilde{m}+1-\sum_\alpha 2\kappa_\alpha\mathrm{e}^{-\mathrm{i}k_\alpha a_\alpha\tilde{\gamma}_\alpha}\right). \tag{83}$$

Here, we introduced the dimensionless mass and tunnellings

$$\tilde{m}=\frac{ma_1}{1+\xi_1+\xi_2},\quad \kappa_\alpha=\frac{a_1}{2a_\alpha}\frac{1}{(1+\xi_1+\xi_2)}, \tag{84}$$

which, in addition to the spatial anisotropy ξ_2 defined in Eq. (22), also depend on the temporal anisotropy

$$\xi_1=\frac{a_0}{a_1}. \tag{85}$$

In addition, due to the anti-periodicity in the time direction, the momenta $\boldsymbol{k}=(k_0,k_1,k_2)^{\mathrm{t}}$ in the Brillouin zone are

$$k_0=-\frac{\pi}{a_0}+\frac{2\pi(n_0+\frac{1}{2})}{N_0a_0},\quad k_j=-\frac{\pi}{a_j}+\frac{2\pi n_j}{N_ja_j}, \tag{86}$$

where we recall that $j\in\{1,2\}$, and $n_\alpha\in\mathbb{Z}_{N_\alpha}$.

Following the previous section, we can introduce dimensionless versions of the auxiliary Hubbard–Stratonovich fields $\tilde{\Sigma}$, $\tilde{\Pi}_2$. The action corresponding to the partition function $Z=\int\mathrm{d}\overline{\tilde{\Psi}}\mathrm{d}\tilde{\Psi}\mathrm{d}\tilde{\Sigma}\mathrm{d}\tilde{\Pi}_2\exp(-S_E[\overline{\tilde{\Psi}},\tilde{\Psi},\tilde{\Sigma},\tilde{\Pi}_2])$ now reads

$$S_E=N\frac{\tilde{Q}}{\tilde{g}^2}\left(\tilde{\Sigma}^2+\tilde{\Pi}_2^2\right)+\sum_{\boldsymbol{k}}\overline{\tilde{\Psi}}_{\boldsymbol{k}}S_{\boldsymbol{k}}^0(\tilde{m}+\tilde{\Sigma},\tilde{\Pi}_2)\tilde{\Psi}_{\boldsymbol{k}}, \tag{87}$$

where we have assumed homogeneous auxiliary fields, and introduced the dimensionless volume and coupling strength

$$\tilde{Q} = N_0 N_1 N_2, \quad \tilde{g}^2 = \frac{g^2}{a_1} \frac{\xi_1 \xi_2}{(1+\xi_1+\xi_2)^2}. \tag{88}$$

Additionally, in analogy to the continuum-time case in Eqs. (64) and (66), the free action in momentum space (83) gets modified by the presence of the auxiliary fields to

$$S^0_{\boldsymbol{k}}(\tilde{m}+\tilde{\Sigma}, \tilde{\Pi}_2) = S^0_{\boldsymbol{k}}(\tilde{m}) + \mathbb{I}_N \otimes (\tilde{\Sigma} + \tilde{\Pi}_2 \tilde{\gamma}_2). \tag{89}$$

One now proceeds by integrating out the fermions to find an effective action for the auxiliary fields $Z = \int d\tilde{\Sigma} d\tilde{\Pi}_2 \; e^{-N\tilde{Q} \mathrm{s}_E[\tilde{\Sigma}, \tilde{\Pi}_2]}$, where the action per unit volume and flavour number is

$$\mathrm{s}_E[\tilde{\Sigma}, \tilde{\Pi}_2] = \frac{1}{\tilde{g}^2}(\tilde{\Sigma}^2 + \tilde{\Pi}_2^2) - \frac{1}{\tilde{Q}} \sum_{\boldsymbol{k}} \log\left(\tilde{\mathrm{s}}^2_{\boldsymbol{k}}(\tilde{m}+\tilde{\Sigma}, \tilde{\Pi}_2)\right). \tag{90}$$

In this expression, we have introduced the function

$$\begin{aligned} \tilde{\mathrm{s}}^2_{\boldsymbol{k}}(\tilde{m}+\tilde{\Sigma}, \tilde{\Pi}_2) = &\left(\tilde{m} + \tilde{\Sigma} + \tilde{m}_E(\boldsymbol{k})\right)^2 \\ &+ \sum_\alpha \left(2\kappa_\alpha \sin(k_\alpha a_\alpha) + \tilde{\Pi}_\alpha \delta_{\alpha,2}\right)^2, \end{aligned} \tag{91}$$

and the dimensionless Euclidean version of the Wilson-term contribution to the mass in Eq. (72), namely

$$\tilde{m}_E(\boldsymbol{k}) = 1 - \sum_\alpha 2\kappa_\alpha \cos(k_\alpha a_\alpha). \tag{92}$$

Let us also note that for the $\tilde{\gamma}_1$ channel, one simply changes $\delta_{\alpha,2} \to \delta_{\alpha,1}$ in Eq. (91).

As occurred for continuous time, the flavour number N plays the role of an inverse Planck's constant $h_{\mathrm{eff}} \propto 1/N$, and the large-$N$ limit is controlled by the semi-classical limit where the auxiliary fields do not fluctuate around the saddle-point configurations $h_{\mathrm{eff}} \to 0$. The gap equations corresponding to this Euclidean saddle point are

$$\frac{\tilde{\Sigma}}{\tilde{g}^2} = \frac{1}{\tilde{Q}} \sum_{\boldsymbol{k}} \frac{\tilde{m} + \tilde{\Sigma} + \tilde{m}_E(\boldsymbol{k})}{\tilde{\mathrm{s}}^2_{\boldsymbol{k}}(\tilde{m}+\tilde{\Sigma}, \tilde{\Pi}_2)}, \tag{93}$$

$$\frac{\tilde{\Pi}_2}{\tilde{g}^2} = \frac{1}{\tilde{Q}} \sum_{\boldsymbol{k}} \frac{2\kappa_2 \sin(k_2 a_2) + \tilde{\Pi}_2}{\tilde{\mathrm{s}}^2_{\boldsymbol{k}}(\tilde{m}+\tilde{\Sigma}, \tilde{\Pi}_2)}. \tag{94}$$

Note that the structure resembles that of Eqs. (70) and (71), allowing us to use the same algorithm for their numerical solution, albeit having an extra mode sum for the time-like direction stemming from the Euclidean discretization. In the continuum-time case, this mode sum would correspond to the integration over the Matsubara frequencies, which was performed analytically to arrive at Eqs. (70) and (71).

4.3. Time doublers and mass renormalizations

As advanced at the beginning of the previous subsection, the spurious time doublers must be carefully accounted for in order to recover the correct phase diagram in the continuum-time limit. This situation was first noted for the (1+1) Gross–Neveu model with a Wilson-type discretization [131]. In the present context, by inspection of Eq. (83), one can readily see that the expansions around $k_0 \in \{0, \pi/a_0\}$ yield long-wavelength actions that resemble those of a continuum massive Dirac fermion. Parallelling the discussion around of the long-wavelength Hamiltonian QFT (15),

there are points in $\boldsymbol{k}$-space, $\boldsymbol{K}_{\boldsymbol{n}_d} = (\pi n_{d,0}/a_0, \pi n_{d,1}/a_1, \pi n_{d,2}/a_2)$ for $\boldsymbol{n}_d = (n_{d,0}, n_{d,1}, n_{d,2}) \in \{0,1\}\times\{0,1\}\times\{0,1\}$, around which we can define a set of Dirac spinors $\{\Psi_{\boldsymbol{n}_d}(\boldsymbol{k})\}_{\boldsymbol{n}_d}$ with N flavours governed by the long-wavelength Euclidean action

$$S_F = \int \frac{\mathrm{d}^3k}{(2\pi)^3} \sum_{\boldsymbol{n}_d} \overline{\Psi}_{\boldsymbol{n}_d}(\boldsymbol{k}) \left(\mathrm{i}\left(\mathbb{I}_N \otimes \tilde{\gamma}^{\mu}_{\boldsymbol{n}_d}\right)k_\mu + m_{\boldsymbol{n}_d}\right) \Psi_{\boldsymbol{n}_d}(\boldsymbol{k}). \tag{95}$$

Here, the repeated-index sum is performed with respect to the Euclidean metric, and the Euclidean gamma matrices for each Dirac fermion are labelled by $\boldsymbol{n}_d \in \mathbb{Z}_2^3$ and read

$$\tilde{\gamma}^0_{\boldsymbol{n}_d} = (-1)^{n_{d,0}}\tilde{\gamma}_0, \quad \tilde{\gamma}^1_{\boldsymbol{n}_d} = (-1)^{n_{d,1}}\tilde{\gamma}_1, \quad \tilde{\gamma}^2_{\boldsymbol{n}_d} = (-1)^{n_{d,2}}\tilde{\gamma}_2, \tag{96}$$

whereas the corresponding Euclidean Wilson masses are

$$m_{\boldsymbol{n}_d} = m + \frac{2n_{d,0}}{a_0} + \frac{2n_{d,1}}{a_1} + \frac{2n_{d,2}}{a_2}. \tag{97}$$

As we can see, in addition to the fermion doublers for $n_{d,0} = 0$, which correspond precisely to the physical spatial doublers obtained in the long-wavelength Hamiltonian QFT from the model defined on the physical lattice (15), we get extra doublers at $n_{d,0} = 1$, which are an artifact of the discretization of time, and we refer to them as spurious time doublers.

Let us now discuss how these time doublers affect the phase diagram, and how one can recover the correct continuous-time limit. Although one may expect that sending $a_0 \to 0$ makes these spurious doublers very massive (97), such that they have no effect on the low-energy physics, it turns out that they can induce additive renormalizations that do not vanish as we approach such a continuous-time limit. As detailed in Appendix B, this renormalization can be obtained by comparing the gap equations of the discrete-time Euclidean formulation, in the limit $a_0 \to 0$, with those of the Hamiltonian approach that are directly derived for continuous times.

In particular, we find that the gap equation for the Lorentz-breaking Π_j condensates become equal in this limit, but those of the scalar Σ condensate differ by an additive term that scales with the coupling strength g^2 and does not vanish when $a_0 \to 0$. As discussed in the Appendix, such a term can be identified with the contribution of the spurious time doublers at $n_{d,0} = 1$, and leads to an additional shift of the bare mass. Hence, if we want to recover the correct phase diagram of the model by solving the dimensionless version of the Euclidean-lattice gap equations in Eqs. (93)–(94), we need to combine this renormalization with the rescalings of Eqs. (84) and (88). This can be summarized in the redefinition of the phase-diagram axes

$$\begin{aligned} \frac{g^2}{a_1} &= \frac{(1+\xi_1+\xi_2)^2}{\xi_1\xi_2}\tilde{g}^2, \\ ma_1 &= (1+\xi_1+\xi_2)\tilde{m} + \frac{(1+\xi_1+\xi_2)^2}{2\xi_1}\tilde{g}^2. \end{aligned} \tag{98}$$

Likewise, the condensates from the Hamiltonian and Euclidean-lattice approached are connected as follows $\Sigma a_1 = (1+\xi_1+\xi_2)\tilde{\Sigma}$ and $\Pi_2 a_2 = (1+\xi_1+\xi_2)\tilde{\Pi}_2$.

In summary, we see that discretization of the time-like direction introduces spurious doublers that would lead to a modified phase diagram if left unnoticed. This is not so important for LFTs, as one typically concentrates on the properties of the continuum QFT that arises around the critical line, but its specific location in terms of the bare parameters is not of relevance. However, for the application of this method to understand the phase diagram of an interacting QAH phase, e.g. understanding the robustness of the Chern insulator to interactions, it is crucial to keep track of these renormalization effects. In Fig. 14, we represent the phase diagram obtained by solving the discrete-time gap Eqs. (93)–(94) using the re-scalings and renormalizations of Eq. (98). We explore different temporal and spatial anisotropies $\xi_1 = \{10, 20, 40, 64\}$, $\xi_2 = 1$ (left panel), and $\xi_1 = \{20, 40, 64\}$, $\xi_2 = 0.5$ (right panel). Note that the time-continuum limit corresponds to $\xi_1 = a_1/a_0 \to \infty$, while the spatial anisotropies translate into $a_1 = a_2$ (Fig. 14**(a)**) and $a_1 < a_2$ (Fig. 14**(b)**). The corresponding critical lines are depicted by dashed lines, where the grey scale becomes darker for increasing temporal anisotropy. The black solid lines correspond to the results

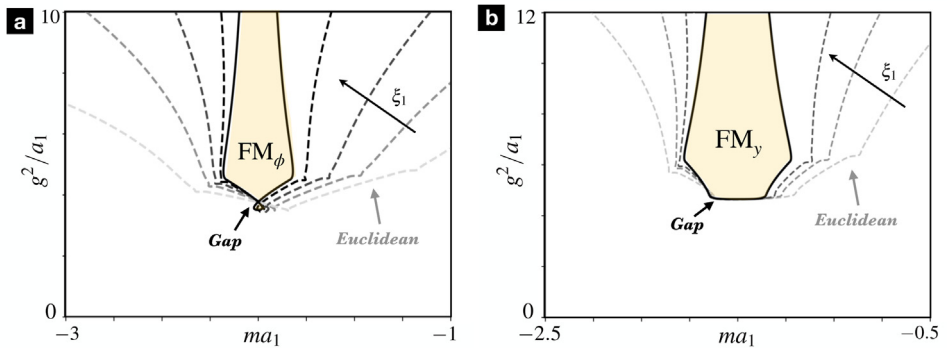

Fig. 14. Phase diagram with Lorentz-breaking condensates on the Euclidean lattice: The critical lines obtained by the solution of the large-N gap Eqs. (70) and (71) in continuous time (black solid line) and those in Eqs. (93)–(94) for discrete time (dashed lines with grey scale). The later require using the rescalings and renormalizations of Eq. (98), and correspond to temporal anisotropies $\xi_1 = \{10, 20, 40, 64\}$. In **(a)** we present the results for $\xi_2 = 1$, whereas **(b)** corresponds to $\xi_2 = 0.5$. In both cases, as the temporal anisotropy increases, the discrete-time critical lines tend towards the continuum ones, and we expect a perfect agreement for $\xi_1 \to \infty$.

depicted in Fig. 13, and thus to the numerical solution of the Hamiltonian-field theory gap Eqs. (70) and (71), which have no contribution from spurious time doublers. Both figures show how the results obtained from the Euclidean-lattice formulation with a discrete time, and both dimensionless fields and couplings, converge to the time-continuum phase diagram as one increases the temporal anisotropy $\xi_1 \to \infty$.

The advantage of the Euclidean-lattice formulation is now two-fold. On the one hand, Monte Carlo techniques developed in the LFT community that employ Wilson fermions in the fermionic sector of QCD could be readily applied to go beyond the current gap equations, provided that one takes the lesson learned from the parameter rescaling and renormalizations (98). On the other hand, we can use the Euclidean-lattice formalism to calculate the effective potential, as discussed in the following section and, by virtue of the relations (98), also explore the regions of the phase diagram where the correlated QAH phase is expected to be found.

5. Effective potential and large-N Chern insulators

As briefly discussed in the introduction of Section 4, the large-N radiative corrections of four-Fermi QFTs can be represented by a collection of one-particle irreducible (1PI) amputated diagrams composed of a single fermion loop and an even number of external auxiliary lines (see Fig. 11), all of which have zero external momenta and no external fermion lines, i.e. amputated. This type of Feynman diagrams appears naturally in the context of the so-called effective action S_{eff}, which acts as the generating functional of proper vertex functions, defined as the inverse of the dressed n-point propagators [209]. For instance, the 2-point vertex function contains all the non-perturbative information encoded in the self-energy $\Sigma_s(\boldsymbol{k})$, which will play a key role in the description of correlation effects in the QAH phases. Let us now discuss why these are the relevant diagrams in the large-N limit, and how they can be resummed to obtain the effective potential.

In general, the effective action $S_{\text{eff}}[\varphi_c(x)]$ is a functional of the symmetry-breaking order parameter, which can be seen as a classical field $\varphi_c(x)$. In the context of chiral-invariant four-Fermi QFTs, this order parameter is the aforementioned scalar condensate (59), which we recall is proportional to the vacuum expectation value of the $\sigma(x)$ field playing the role of $\varphi_c(x)$. In a translationally-invariant situation $\partial_\mu \varphi_c(x) = 0$, analogous to the case $\sigma(x) = \Sigma, \ \forall x$ explored in the previous section, this effective action can be expressed as the spacetime integral of an effective potential $S_{\text{eff}}[\Sigma] = \int \mathrm{d}^D x V_{\text{eff}}(\Sigma)$. We note that, by going to momentum space, this effective action can only generate vertex functions with zero external momentum. Accordingly, the effective action

for a translationally-invariant classical field is built from all the amputated 1PI Feynman diagrams evaluated at zero external momentum. These diagrams allow one to understand how the radiative corrections of a purely quantum-mechanical origin affect the process of spontaneous symmetry breaking in scalar QFTs [202,229]. Moreover, the effective potential also allows to go beyond perturbation theory, providing a neat instance of large-N methods [112,203].

The standard discussion of the effective potential for four-Fermi QFTs [112] must be reconsidered in our case (10), as we have already argued that, for our choice of gamma matrices (2), chiral symmetry is absent from the outset. In fact, we have also noted that, except for the specific couplings corresponding to the symmetry line of Fig. 13, the σ field displays a non-zero vacuum expectation value that is not connected to any spontaneous symmetry breaking. Therefore, the $\sigma(x)$ field cannot play the role of the classical field $\varphi_c(x)$ in our case. On the other hand, as discussed in the previous section, there are two alternative symmetry-breaking channels in which inversion (61), instead of chirality (4), is the symmetry that is actually broken at the phase transition. We recall that these channels were activated by non-zero values of the auxiliary π fields (60) rather than the σ field (59). From this perspective, we need to revisit the discussion of the resummation of the leading-order Feynman diagrams to obtain an adequate effective potential. In this subsection, we present the details corresponding to the $\tilde{\Pi}_2$ channel, giving a detailed account of the effective potential $V_{\text{eff}}(\tilde{\Pi}_2)$ in the large-N limit, although we also note that the calculations for the $\tilde{\Pi}_1$ channel are completely analogous. Armed with this effective potential, we can now explore the regions where inversion symmetry remains intact, and use the effective potential to characterize the extent of the QAH phase as interactions are increased.

5.1. Fermion condensates and the effective potential

Let us consider the anisotropic regime $a_1 < a_2$, which allows us to focus on a single Lorentz-breaking field $\tilde{\Pi}_2$. We recall that, by introducing the auxiliary field via a Hubbard–Stratonovich transformation, one sees that the field does not have kinetic energy and is subjected to a classical potential

$$V_{\text{cl}}(\tilde{\Pi}_2) = \frac{N}{2\tilde{g}^2}\tilde{\Pi}_2^2. \tag{99}$$

This expression accounts for the $\tilde{g}^2/N$ scaling of the auxiliary-field lines/propagators mentioned in the introduction of Section 4. In the present subsection, we use the adimensional formulation of the model (87), so that all adimensional quantities appear with a tilde, and we should apply the required rescalings and renormalizations in Eq. (98) at the end.

At the classical level, this potential (99) finds its minimum at $\tilde{\Pi}_{2,c} = 0$, such that there is no spontaneous breakdown of inversion symmetry. However, this is not the full picture, as one should also introduce quantum-mechanical corrections, leading to the full effective potential

$$V_{\text{eff}}(\tilde{\Pi}_2) = V_{\text{cl}}(\tilde{\Pi}_2) + \delta V_{\text{q}}(\tilde{\Pi}_2) \tag{100}$$

In the $N \to \infty$ limit, these quantum corrections $\delta V_{\text{q}}(\tilde{\Pi}_2)$ correspond to all of the amputated 1PI diagrams at zero external momentum which, after introducing the auxiliary field (see Fig. 11), can be constructed by combining fermion loops and auxiliary $\tilde{\Pi}_2$ lines. Note we can decorate these diagrams with any number of external auxiliary lines and still obtain contributions to the vertex functions with zero external momentum. These external lines must be connected to a fermion loop via the coupling term $\tilde{\Pi}_2(\tilde{\bar{\Psi}}\tilde{\gamma}_2\tilde{\Psi})$, which does not scale with $1/N$ in comparison to the original four-Fermi term (9). We can thus introduce an arbitrary number of external auxiliary fields without altering the scaling $\mathcal{O}(N^\alpha)$ of the specific order α in a large-N expansion. On the contrary, inserting internal auxiliary lines, as in Fig. 11**(b)**, is penalized by an extra $1/N$ scaling for each auxiliary-field propagator, as the mass of this auxiliary field scales with N (see Fig. 11**(a)**). Likewise, since extra fermion loops can only be introduced in 1PI diagrams by means of additional internal lines of the auxiliary field, they will also give sub-leading contributions. The leading-order contribution in the $N \to \infty$ limit can thus be obtained by resumming the series of Feynman diagrams with a single fermion loop and increasing numbers of external auxiliary lines (see Fig. 11**(c)**).

In Appendix C we show how, in analogy to the chiral-invariant case, one only needs to decorate this single fermion loop with even numbers of external auxiliary lines. These large-N diagrams contribute to the effective potential as

$$\delta V_{\mathrm{q}}(\tilde{\Pi}_2) = N \sum_{n=1}^{\infty} \frac{1}{2n} \int_{\boldsymbol{p}} \mathrm{Tr} \left(-\mathrm{i}\tilde{\gamma}_2 \frac{\tilde{\Pi}_2}{(\mathrm{i}\not{p} + \tilde{m}(\boldsymbol{k}))} \right)^{2n}, \tag{101}$$

where we have introduced $\not{p} = \tilde{\gamma}^{\alpha} p_{\alpha}$, and

$$p_{\alpha} = 2\kappa_{\alpha} \sin k_{\alpha}, \quad \tilde{m}(\boldsymbol{k}) = \tilde{m} + \tilde{\Sigma} + \tilde{m}_E(\boldsymbol{k}), \tag{102}$$

where $\tilde{m}_E(\boldsymbol{k})$ is the Euclidean Wilson-type contribution to the mass that already appeared in Eq. (92). For a continuum QFT, p_{α} would be the Euclidean momentum with an ultra-violet cutoff, e.g. $p \leq \Lambda_{\mathrm{c}}$, and $\tilde{m}$ the adimensional bare mass. We also note that the repeated-index summation is performed using the Euclidean metric, and we use a mode-sum discretization of the integral $\int_{\boldsymbol{p}} = \frac{1}{\tilde{\Omega}} \sum_{\boldsymbol{k}}$ over the reciprocal BZ (86).

In addition to these straightforward differences due to the lattice regularization, the above expression (101) differs from the standard effective potential of continuum QFTs like Eq. (1) by the appearance of the $\tilde{\gamma}_2$ matrix. As discussed in Appendix C, this complicates considerably the resummation method with respect to the standard calculations [112], and leads to new quantum-mechanical sources of radiative corrections $\delta V_{\mathrm{q}}(\tilde{\Pi}_2) = \delta V_{\mathrm{q},1}(\tilde{\Pi}_2) + \delta V_{\mathrm{q},2}(\tilde{\Pi}_2)$, which will play a key role below. In addition to the standard contribution

$$\delta V_{\mathrm{q},1}(\tilde{\Pi}_2) = -N \int_{\boldsymbol{p}} \log \left(1 + \frac{\tilde{\Pi}_2^2}{p^2 + \tilde{m}^2(\boldsymbol{k})} \right), \tag{103}$$

which is also found for chiral invariant QFTs in the continuum by simply letting $\tilde{\Pi}_2 \to \tilde{\Sigma}$ [112], we find that the new Lorentz-breaking channel has new radiative corrections given by

$$\delta V_{\mathrm{q},2}(\tilde{\Pi}_2) = -\frac{N}{2} \int_{\boldsymbol{p}} \log \left(1 - \frac{4p_2^2 \tilde{\Pi}_2^2}{\left(p^2 + \tilde{m}^2(\boldsymbol{k}) + \tilde{\Pi}_2^2\right)^2} \right). \tag{104}$$

Let us now connect to our discussion of the gap equations in Section 4. Note that both the classical and quantum contributions to the effective potential scale with N at this leading order, such that an effective Planck's constant $\hbar_{\mathrm{eff}} \propto 1/N$ shall vanish in the large-N limit. Accordingly, the leading-order solution is found by searching for the minima of $V_{\mathrm{eff}}(\tilde{\Pi}_2)$ at different points in the $(\tilde{m}, \tilde{g}^2)$-plane. With respect to the classical case (99), which only allows for a zero Lorentz-breaking condensate, the quantum corrections can lead to new minima in which a non-zero value of $\tilde{\Pi}_2$ develops. Although not apparent at first sight, these minima correspond to the saddle points of the action per unit volume and number of flavours $\mathrm{s}_E[\tilde{\Sigma}, \tilde{\Pi}_2]$ introduced in Eqs. (90)–(91), which was obtained by integrating over the fermionic Grassmann variables after the Hubbard–Stratonovich transformation, and led to the previous gap Eqs. (93)–(94). Although not directly apparent in Eqs. (90)–(91), the action $\mathrm{s}_E[\tilde{\Sigma}, \tilde{\Pi}_2]$ is invariant under the transformation $\tilde{\Pi}_2 \to -\tilde{\Pi}_2$, which can be seen by making $\boldsymbol{k}_2 \to -\boldsymbol{k}_2$ in the momentum integrals, and thus amounts to inversion symmetry (61). Using the notation of the present Eq. (102), we could rewrite this action as

$$\begin{aligned} \mathrm{s}_E[\tilde{\Sigma}, \tilde{\Pi}_2] &= \tfrac{1}{2} \left(\mathrm{s}_E[\tilde{\Sigma}, \tilde{\Pi}_2] + \mathrm{s}_E[\tilde{\Sigma}, -\tilde{\Pi}_2] \right) = \tfrac{1}{\tilde{g}^2} \left(\tilde{\Sigma}^2 + \tilde{\Pi}_2^2 \right) \\ &+ \tfrac{1}{2} \int_{\boldsymbol{p}} \log \left[\left(p_+^2 + \tilde{m}^2(\boldsymbol{k}) \right) \left(p_-^2 + \tilde{m}^2(\boldsymbol{k}) \right) \right] \end{aligned} \tag{105}$$

where we have introduced the displaced momenta $p_{\pm} = (p_0, p_1, p_2 \pm \tilde{\Pi}_2)$. Using the properties of the logarithm, one can then express the effective potential with the radiative corrections of Eqs. (103) and (104) as

$$V_{\mathrm{eff}}(\tilde{\Pi}_2) = N(\mathrm{s}_E[\tilde{\Sigma}, \tilde{\Pi}_2] - \mathrm{s}_E[\tilde{\Sigma}, 0]) \tag{106}$$

where we subtract $\mathrm{s}_E[\tilde{\Sigma}, 0] = \tilde{\Sigma}^2/\tilde{g}^2 - \int_{\boldsymbol{p}} \log \left(p^2 + \tilde{m}^2(\boldsymbol{k}) \right)$. Since this last term does not depend on the symmetry-breaking order parameter $\tilde{\Pi}_2$, this subtraction does not modify the position of the

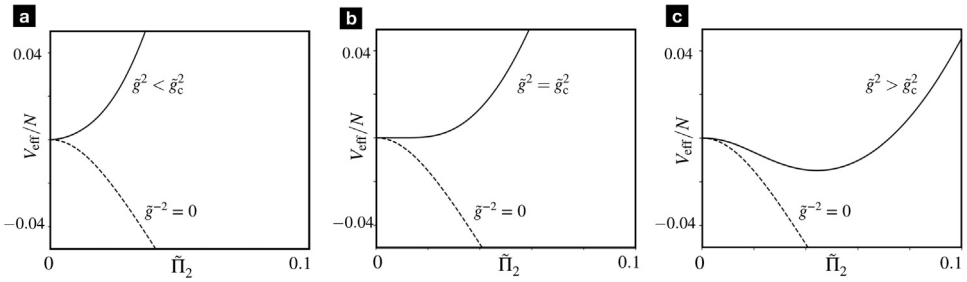

Fig. 15. Effective potential and the spontaneous breakdown of inversion symmetry: We represent the numerical values of $V_{\text{eff}}(\tilde{\Pi}_2)$ obtained by evaluating Eq. (107) for different couplings $\tilde{g}^2$ (solid line) and the isolated quantum corrections labelled by $\tilde{g}^{-2} = 0$ (dashed line). **(a)** For $\tilde{g}^2 < \tilde{g}_c^2$, the minimum occurs for $\tilde{\Pi}_2 = 0$. **(b)** For $\tilde{g} = \tilde{g}_c$, the effective potential changes from a quadratic to a quartic dependence for small values of the symmetry-breaking $\tilde{\Pi}_2$ field. **(c)** For $\tilde{g}^2 > \tilde{g}_c^2$, a minimum with non-zero value of $\tilde{\Pi}_2$ appears, signalling the breakdown of inversion symmetry.

minima, and the current diagrammatic derivation (103)–(104) and the effective action obtained by integrating out the fermions (90)–(91) are thus consistent. The diagrammatic derivation, however, separates novel quantum corrections (104) from those appearing in chiral-invariant QFTs (103), and thus allows to identify new effects that can be brought up by these radiative corrections. As explored below in Section 5.3, an important consequence of these additional radiative corrections is both to displace critical lines, and moreover to change the nature of the inversion-breaking phase transition in the neighbourhood of the line of symmetry $ma_1 = -2$ from second to first order.

It is important to stress that the effective potential (100) provides similar information to the gap Eqs. (93)–(94), while not being restricted to a non-zero value of $\tilde{\Pi}_2$. This will be crucial to explore the full phase diagram of the model. Let us now describe our numerical method to obtain the minima of the effective potentials, which can be explicitly written as

$$\begin{aligned}\frac{V_{\text{eff}}(\tilde{\Pi}_2)}{N} = \frac{\tilde{\Pi}_2^2}{2\tilde{g}^2} - \frac{1}{\tilde{Q}}\sum_{\boldsymbol{k}}\log\left[1 + \frac{\tilde{\Pi}_2^2}{\tilde{m}^2(\boldsymbol{k}) + \sum_\alpha 4\kappa_\alpha^2 \sin^2(k_\alpha a_\alpha)}\right] \\ - \frac{1}{2\tilde{Q}}\sum_{\boldsymbol{k}}\log\left[1 - \frac{16\kappa_2^2 \sin^2(k_2 a_2)\tilde{\Pi}_2^2}{\left(\tilde{m}^2(\boldsymbol{k}) + \sum_\alpha 4\kappa_\alpha^2 \sin^2(k_\alpha a_\alpha) + \tilde{\Pi}_2^2\right)^2}\right].\end{aligned} \tag{107}$$

As occurred for the gap equation (94), the effective potential only depends on the combination of parameters $M = \tilde{m} + \tilde{\Sigma}$, as one readily finds by inspecting Eq. (102). We can thus fix the value of M, evaluate the mode sums of Eq. (107) for a given lattice volume $\tilde{Q}$, and use a numerical minimization algorithm to find the value of the Lorentz-breaking condensate $\tilde{\Pi}_2$. In Fig. 15, we represent the effective potential as a function of the Lorentz-breaking condensate for three different values of the adimensional coupling strength $\tilde{g}^2$, after fixing $M = -1.8$. Since the potential is symmetric under $\tilde{\Pi}_2 \to -\tilde{\Pi}_2$, we only represent it for positive-valued condensates. In all three figures, we represent with a dashed line the quantum corrections in Eqs. (103)–(104), which are labelled as $\tilde{g}^{-2} = 0$. When adding these radiative corrections to the classical potential, we observe three different regimes. In Fig. 15**(a)**, we observe that the effective potential has single minimum at $\tilde{\Pi}_2 = 0$, such that the discrete inversion symmetry is preserved. As we keep on increasing the coupling $\tilde{g}^2$, the curvature of the potential changes in Fig. 15**(b)**, until the potential develops a double-well structure with a minimum at a non-zero value of the condensate, corresponding the spontaneous breakdown of inversion symmetry (see Fig. 15**(c)**). We can thus identify a critical interaction $\tilde{g}_c^2$, which defines a critical point and indicates the location of the phase boundary.

According to our previous discussion, this critical point must coincide with the corresponding point on the phase boundary predicted by our numerical solution of the gap Eqs. (93)–(94). In order to compare both methods, we need to extract the bare mass $\tilde{m}$, which can be determined by plugging the value of the minimum $\tilde{\Pi}_2$ into Eq. (93), and then solving it numerically to

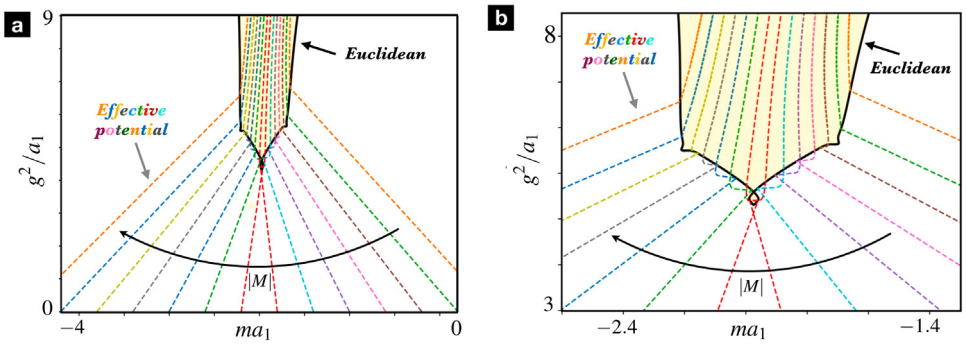

Fig. 16. Phase diagram predicted by the large-N effective potential: **(a)** We represent in dashed coloured lines the constant-M trajectories describing the bare parameters $(ma_1, g^2/a_1)$ where one obtains a minimum of the potential (107) for a fixed value of $M = \tilde{m} + \tilde{\Sigma}$, but varying bare parameters. In a black solid line, the results based on the discrete-time gap Eqs. (93)–(94) for the same temporal anisotropy $\xi_1 = 64$ are presented. **(b)** Zoom into the trajectories shown in **(a)**, which shows the kinks of the dashed coloured lines precisely at the critical line where the inversion-breaking condensate forms. For this spatial isotropic case $\xi_2 = 1$, this condensate corresponds to the orbital FM_ϕ phase.

find the value of the scalar condensate $\tilde{\Sigma}$, after which one simply subtracts $\tilde{m} = M - \tilde{\Sigma}$. By repeating this algorithm for different couplings $\tilde{g}^2$ one can draw trajectories of constant M in the $(ma_1, g^2/a_1)$-plane, remembering that the dimensionless couplings have to be rescaled and renormalized according to Eq. (98). Each of the trajectories can be labelled by the input parameter M, which corresponds physically to the bare mass $\tilde{m}$ at zero coupling $\tilde{g}^2 = 0$, since the scalar condensate can only become non-zero as one switches on the interactions. For $a_1 > a_2$, the numerical routine is similar, but we need to exchange $\tilde{\Pi}_2, p_2\tilde{\Pi}_2 \to \tilde{\Pi}_1, p_1\tilde{\Pi}_1$ in Eqs. (103)–(104). For $a_1 = a_2$, both corrections give the same result, signalling that the symmetry-breaking can occur for any linear combination $\cos\phi\tilde{\Pi}_1 + \sin\phi\tilde{\Pi}_2$.

In Fig. 16**(a)**, some of these trajectories are plotted for the isotropic case $a_1 = a_2$, using dashed lines with different colours for the different values of M. In this figure, we also plot with a solid black line the critical points predicted by the solution of the gap Eqs. (93)–(94) for the same volume $\tilde{Q}$. The structure of the trajectories is clear, they are straight lines until hitting the critical line, where they bend backwards before entering the symmetry-broken phase. By zooming into the critical region, as presented in Fig. 16**(b)**, this bending becomes clearer, and one sees that it is actually preceded by a kink that coincides exactly with the parameters where $V_{\mathrm{eff}}(\tilde{\Pi}_2)$ develops a non-zero condensate $\Pi_2 > 0$. By inspecting Eq. (93) in light of the function (91), it is clear that the spontaneous formation of a non-zero condensate $\tilde{\Pi}_2$ results in a decreased value of the $|\tilde{\Sigma}|$, such that $\tilde{m}$ changes abruptly from increasing(decreasing) with $\tilde{g}^2$ into decreasing (increasing), depending on the side of the symmetry axis at $\tilde{m} = -2$ in which the trajectory resides. Therefore, the kink can be directly associated with the spontaneous breakdown of inversion symmetry, which allows us to identify the critical line delimiting the $\tilde{\Pi}_2$ condensate. As shown in this figure, this critical line agrees perfectly with the solutions predicted by the gap equations, which serves as a benchmark of our numerical method for the effective potential. Once the validity has been demonstrated, we can now exploit the effective potential to get insights in the symmetry-preserved region, going beyond the information that can be extracted from the gap equations.

5.2. Scalar condensate and topological invariants

In the subsection above, we have seen how the effective potential can be used to determine the Lorentz-breaking condensate which, as argued previously, is the large-N version of the orbital ferromagnet FM_ϕ in the isotropic case $a_1 = a_2$. In contrast to the gap equations, however, we can also explore regions of parameter space where this condensate is zero. We have also noted that the effective action, obtained by the spacetime integral of the effective potential, serves as the

generating functional of any n-point proper vertex functions [209]. In this section, we focus on the 2-point function in momentum space $\Gamma^{(2)}(\boldsymbol{p})$, which contain information about all the intermediate scattering processes in which particle–antiparticle pairs are virtually created, and can be expressed by a sum of 1PI diagrams leading to the self energy $\tilde{\Sigma}_s(p)$. From the perspective of Euclidean QFTs of Dirac fermions in the continuum, the 2-point proper vertex is the inverse of the dressed Euclidean propagator $\Gamma^{(2)}(p) = \mathrm{i}\not{p} + m + \tilde{\Sigma}_s(p)$. Within the realm of the large-N approximation, the self energy is easily expressed in terms of the condensates as

$$\Sigma_s(p) = \left(\Sigma + \gamma^1 \Pi_1 + \gamma^2 \Pi^2\right)\delta^3(p), \tag{108}$$

where the homogeneity of the condensates is responsible for the momentum independence of the self energy.

In order to make a connection of these concepts with the topological characterization of the QAH phase, we need to rephrase this discussion in the context of condensed matter, where one defines the Euclidean-time single-particle Green's function in terms of the creation-annihilation operators $G(x_1 - x_2) = \langle \mathscr{T}\{\Psi^\dagger(x_1)\Psi(x_2)\}\rangle$ for two spacetime points $x_1 = (\mathrm{i}t_1, \boldsymbol{x}_1)$, and $x_2 = (\mathrm{i}t_2, \boldsymbol{x}_2)$. In a translationally-invariant setting, one can perform Fourier and Matsubara transforms to spatial-momentum $\boldsymbol{k} = (k_1, k_2)$ and frequency $k_0 = \omega$ representations [207,208], such that the inverse Green's function can be expressed as

$$G^{-1}(\mathrm{i}k_0, \boldsymbol{k}) = \mathrm{i}k_0 - h_{\boldsymbol{k}} + \Sigma_s(\mathrm{i}k_0, \boldsymbol{k}), \tag{109}$$

where $h_{\boldsymbol{k}}$ is the single-particle Hamiltonian, like Eq. (13) in our case, and $\Sigma_s(\mathrm{i}k_0, \boldsymbol{k})$ is also called the self energy. Within the large-N approximation, it can be readily connected to Eq. (108) by simple algebra

$$\Sigma_s(\mathrm{i}k_0, \boldsymbol{k}) = \mathbb{I}_N \otimes \left(\gamma^0 \Sigma + \gamma^0\gamma^1 \Pi_1 + \gamma^0\gamma^2 \Pi_2\right)\delta^3(k), \tag{110}$$

which results from the different definition of the propagator (Green's function) in terms of the adjoint (creation) operator.

As advanced in the introduction, topological invariants such as the Chern numbers (20) can be generalized to the many-body case by means of these Green's functions [64,65]. As discussed in [66–70], the static part of the self-energy $\Sigma_s(0, \boldsymbol{k})$ plays a key role in this topological characterization, as it offers a practical route for the calculation of topological invariants beyond the non-interacting limit. Focusing on the inversion-symmetric phase, where we only have a non-zero value of the scalar condensate, we can define the so-called topological Hamiltonian that contains these static contributions

$$h_t = h_{\boldsymbol{k}}(m) + \Sigma_s(0, \boldsymbol{k}) = h_{\boldsymbol{k}}(m) + \gamma^0 \Sigma. \tag{111}$$

It is then a simple matter to realize that the calculation of the Chern number in Eq. (20) can be repeated with the bare mass being renormalized by the static self energy, i.e. $m + \Sigma$, which changes the mapping from the torus onto the unit sphere in Eq. (14) by $\boldsymbol{d}_{\boldsymbol{k}}(m) \to \boldsymbol{d}_{\boldsymbol{k}}(m) + \Sigma \boldsymbol{e}_3$. Following the same calculation, the topological invariant in the presence of interactions is given by

$$N_{\mathrm{Ch}}(g^2) = \frac{N}{2} \sum_{\boldsymbol{n}_d} (-1)^{(n_{d,1}+n_{d,2})} \mathrm{sign}(M_{n_d}), \tag{112}$$

where we have introduced the masses of the spatial doublers renormalized by the scalar condensate

$$M_{\boldsymbol{n}_d} = m + \Sigma + \frac{2n_{d,1}}{a_1} + \frac{2n_{d,2}}{a_2}, \tag{113}$$

and we recall that $\boldsymbol{n}_d = (n_{d,1}, n_{d,2}) \in \{0, 1\} \times \{0, 1\}$.

Note that on a Euclidean lattice, the discretization of the time axis introduces the spurious time doublers previously discussed. However, if we take the limit $a_0 \to 0$ with the appropriate rescaling and renormalization of the bare couplings (98), the model reduces to a two-dimensional large-N Chern insulator, and these spurious time doublers have no influence on the long wavelength physics.

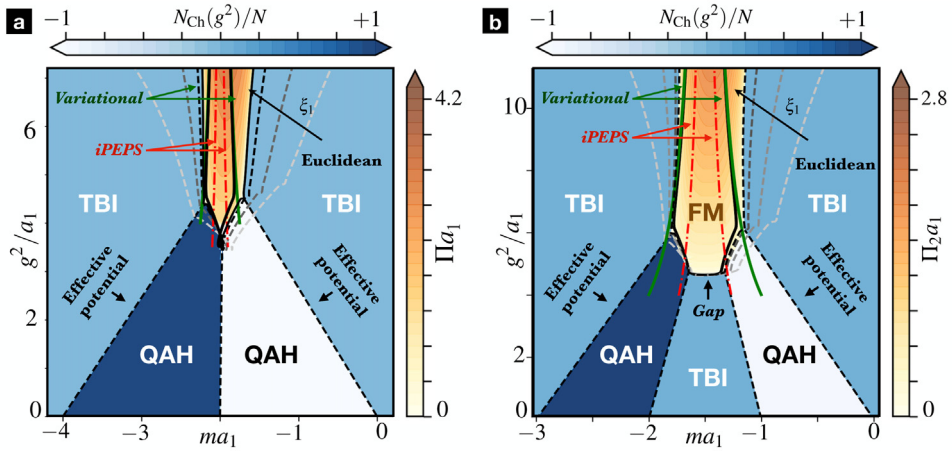

Fig. 17. Full phase diagram with correlated large-N QAH phases: We represent, on a blue scale, a contour plot of the topological invariant in Eq. (112) that allows to locate the correlated QAH phase, and the phase transition to topologically-trivial phases. We also include for comparison, all of the results of the previous sections. The large-N calculations of the continuum-time gap Eqs. (70) and (71) obtained via a Hamiltonian field theory for a single channel, are represented by a solid black line. The discrete-time gap Eqs. (93)–(94) obtained via a Euclidean field theory are represented by dashed lines in a grey scale of increasing temporal anisotropy. The orange-scale contour plot of the symmetry-broken region is obtained by varying the non-zero value of the condensate in those gap equations. The green line shows the critical points (46) predicted by the variational mean-field ansatz in the compass model that emerges at strong couplings. The red dashed–dotted lines correspond to the critical points obtained by the iPEPS variational ansatz of the same compass model. (For interpretation of the references to colour in this figure legend, the reader is referred to the web version of this article.)

In particular, given the discussion of the previous section, these time doublers have a mass with a contribution on the order of $1/a_0$, which becomes very large in the time-continuum limit and is responsible for the fact that the Wilson masses of these spurious time doublers always carry the same sign. As a consequence, not only do they lie at very high energies and thus not appear in the long wavelength limit, but also their contribution to the topological invariant vanishes exactly since we have an even number of them, i.e. 4, giving cancelling contributions to the Chern number.

With these formulas at hand, the previous numerical algorithm that calculates the trajectories displayed in Fig. 16 is very useful, as the input parameter is the renormalized mass $M = \tilde{m} + \tilde{\Sigma}$. This means that one can assign a constant topological invariant to each of these trajectories using Eq. (112), and delimit the phase boundaries separating correlated QAH phases from trivial band insulators within the symmetry-preserved region. In Fig. 17, all of the predictions for the phase diagram are presented together for temporal anisotropy $\xi_1 = 64$, and two spatial anisotropy ratios, namely $\xi_2 = 1$ for Fig. 17**(a)** and $\xi_2 = 0.5$ for Fig. 17 **(b)**. These two anisotropy values correspond to the shaded planes of parameter space depicted in Fig. 2. The blue-scale contour plot was created by generating a dense set of trajectories like those presented in Fig. 16 for different values of M along the x-axis, and then calculating their topological invariant with Eq. (112).

Let us start by focusing on Fig. 17**(a)**, recalling that the topological invariant of the non-interacting QAH effect (23) changes when the mass of an odd number of spatial doublers is inverted, which occurs at $m\,a_1 \in \{0, -2, -4\}$ in the isotropic case $a_1 = a_2$. For the large temporal anisotropies used, the spurious time doublers with masses proportional to $1/a_0$ would lead to additional phase transitions for very large negative values of the bare mass, eventually disappearing completely from the phase diagram when $\xi_1 \to \infty$. This reflects Wilson's idea of turning the doublers into very heavy fermions that do not contribute significantly to the relevant physics. Let us note that, since M collapses to m in the non-interacting limit $g^2 = 0$, as the scalar condensate vanishes $\Sigma = 0$, the trajectories for input values $Ma_1 \in \{0, -2, -4\}$ (black dashed lines in the figure) turn out to be the ones that separate the correlated topological phases with $N_{\mathrm{Ch}}(g^2) = \pm N$ from the trivial band

insulators with a vanishing Chern number as one increases the interactions g^2. Remarkably, we find that these critical lines touch exactly the corners of the solid black line, which represents our numerical solution of the gap equations obtained via the Hamiltonian formalism. For completeness, we also represent with dashed grey-scale lines the results obtained by solving the gap equations in an Euclidean lattice, as one increases the temporal anisotropy towards $\xi_1 = 64$. According to these results, the lines of topological phase transitions meet the line of the symmetry-breaking phase transition, above which the π condensate forms and inversion symmetry is spontaneously broken. Regarding the latter, an orange-scale contour plot was added, which was created by solving the gap equations for different non-zero values of Π_2, bearing in mind that the π condensate can actually be any linear combination of the Π_1 and Π_2 fields in this isotropic limit. The resulting lines of constant values of this condensate retreat to the interior of the phase boundary with increasing Π_2, which could be found out by analysing the scaling of the condensation of the Π_2-field. Let us finally note that the green solid line depicts the critical lines obtained by the variational mean-field calculation of the compass model (46), whereas the red dashed–dotted line is obtained by solving the compass model using the iPEPS variational algorithm for $J_x = J_y$.

In Fig. 17**(b)**, which corresponds to the spatial anisotropy $\xi_2 = 0.5$, a trivial phase arises separating the two correlated QAH phases that have an underlying large-N Chern insulator. The trajectories that correspond to these topological phase transitions, represented again using dashed black lines, are obtained by setting $Ma_1 \in \{0, -1, -2, -3\}$, which connect to critical points for the non-interacting Chern number (23) for $ma_1 \in \{0, -1, -2, -3\}$ as $g^2 \to 0$, as displayed in Fig. 2. The behaviour is very similar to that found in the isotropic case with the novelty that a trivial band insulator now separates the two correlated QAH phases all the way up to the region where the Lorentz-breaking condensate appears. Once again, the critical lines that mark these topological phase transitions extend as straight lines as the interactions g^2 are increased, until they meet the symmetry-breaking critical line precisely at four symmetric corners. In this figure, we also depicted in a red dashed–dotted line the results obtained by solving the compass model using the iPEPS variational algorithm for $J_x = J_y/4$. We see that the region of a non-zero Lorentz-breaking condensate shrinks with respect to the mean-field-type methods, which is a general feature of the latter since the role of super-exchange interactions is typically overestimated, leading to larger regions with magnetic long-range orderings than those predicted by other methods that can better with correlations. The unification of the results exhibits a coherent picture showing that the methods used have been consistent, and can be applied to other similar models.

5.3. First- and second-order phase transitions

As advanced at the end of Section 4.1, the small lobe containing a Lorentz-breaking condensate in the isotropic limit $a_1 = a_2$ (see Figs. 13**(a)** and 14**(a)**) actually persists for weak spatial anisotropies $\xi_2 \approx 1$. As argued in this section, thanks to the formulation based on the effective potential, we can identify the additional radiative corrections (104) as the underlying source of this lobe structure. In Fig. 18, we represent various non-zero values of the Π_2 condensate as a function of the bare parameters $ma_1, g^2/a_1$. The Lorentz-breaking condensate in red is obtained by solving the gap equations that correspond to an effective potential that only considers the radiative corrections common to chiral-invariant theories (103). The blue surface represents the Π_2 condensate when the new radiative corrections (104) are also considered. By comparing both plots, one readily sees that the loop-structure disappears if these novel radiative corrections (104) are not accounted for. Moreover, as one increases the value of the Lorentz-breaking Π_2 condensate, the symmetry-broken phase in blue extends to a larger area in the $(ma_1, g^2/a_1)$ sections until the lobe eventually disappears. In the following, we present a more in-depth study of this re-entrant region via the effective potential, and show that the order of the phase transition can change from second to first order.

Let us now discuss how the effective potential can yield information on the nature of the inversion-breaking phase transition, which we will illustrate for the isotropic case $\xi_2 = 1$ so that the broken phase is labelled FM_ϕ, and the condensate for any particular ϕ will be labelled as Π. Fig. 19 plots $V_{\mathrm{eff}}(\Pi)$ for mass values $1.5 < -ma_1 < 2.5$, corresponding to trajectories similar

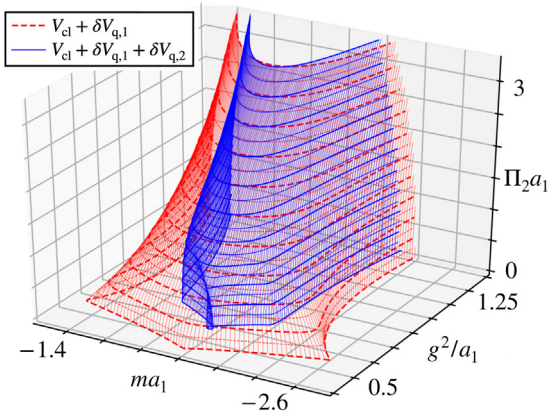

Fig. 18. Comparison of Lorentz-breaking condensates: The red (blue) surfaces represent the Lorentz-breaking condensates as a function of $(ma_1, g^2/a_1)$ for $\xi_2 = 1$, which are obtained by solving the gap equations corresponding to the effective potential with radiative corrections in Eq. (103) (Eqs. (103)–(104)). (For interpretation of the references to colour in this figure legend, the reader is referred to the web version of this article.)

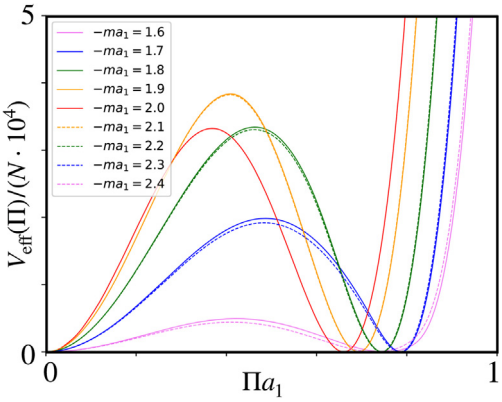

Fig. 19. Critical effective potential near the line of symmetry: $V_{\text{eff}}(\Pi)$ is plotted for $\xi_1 = 64$, $\xi_2 = 1$ for selected values $1.5 < -ma_1 < 2.5$ corresponding to constant-M trajectories intersecting the lobe shown in Fig. 16. Colours have been chosen to emphasize the symmetry under $ma_1 \mapsto -ma_1 - 4$ expected to become exact as $\xi_1 \to \infty$.

to those shown in Fig. 16, but focusing only on those that intersect the lobe of the gap-equation solution. In each case, the coupling is tuned to the critical value $g_c^2(m)$ yielding two degenerate minima of the effective potential. As shown in Fig. 19, at this point, groundstates with two distinct condensates $\Pi = 0$ and $\Pi \neq 0$ co-exist. This contrasts the behaviour presented in Fig. 15 where, recalling the symmetry $\Pi \to -\Pi$, the effective potential changes from a single- to a double-well structure. This is the standard scenario for a second-order phase transition, whereby condensates with a different value of $|\Pi|$ never co-exist. On the contrary, within the current range of bare masses $1.5 < -ma_1 < 2.5$, the inversion-breaking transition is first-order. In this figure, we use solid and dashed lines with the same colours to emphasize that, to very good approximation, the effective potentials calculated for ma_1 and $-ma_1 - 4$ are equal; this symmetry should become exact in the time-continuum limit $\xi_1 \to \infty$. It is also apparent that the strength of the first-order transition defined by the barrier height separating the two minima at $\Pi = 0$ and $\Pi \neq 0$, which corresponds physically to the interface tension, initially grows as m approaches the line of symmetry $ma_1 = -2$,

where Σ vanishes from either direction, but then dips so that the barrier height at the symmetric point actually lies in a local minimum.

As discussed above, the constant-M trajectories shown in Fig. 16 exhibit a sharp kink precisely at the critical $g_c^2(m)$. However, a closer inspection of the figure reveals that this kink actually occurs within the symmetric phase, and thus *before* the phase boundary predicted by the gap Eqs. (93)–(94) is reached. In the neighbourhood of the lobe, therefore, the gap equation is not finding the true transition, but rather tracing the locus of a local minimum of V_{eff}. By contrast, in the regions $0 < -ma_1 < 1.5$, $2.5 < -ma_1 < 4$, $V_{\text{eff}}(\Pi)$ has a unique minimum for all g^2. Accordingly, there is no discontinuity in the value of the condensate $\Pi(g^2)|_{V_{\text{eff}}=V_{min}}$, which is consistent with a continuous second-order phase transition. In this case, the constant-M trajectory kinks of Fig. 16 lie precisely on top of the phase boundary predicted by the gap equations. Following the kink, the trajectory apparently remains for a while in the symmetric phase before curving upwards; however it can be shown that in this region the surface generated by contours of constant Π in the broken phase actually curves back to overhang the symmetric phase (this can just be discerned in Fig. 18). Every point in the phase diagram lying beneath the overhang is therefore intersected by two constant-M trajectories, one corresponding to $\Pi = 0$ and the other to $\Pi \neq 0$, in apparent contradiction with the predicted second-order nature of the transition, it will require a more refined calculation of the full effective potential $V_{\text{eff}}(\Sigma, \Pi)$, i.e. including loops with scalar auxiliary legs, to resolve this ambiguity; indeed, such a calculation will inevitably be needed to examine the nature of the topological phase transitions between the QAH and TBI phases shown in Fig. 17.

6. Spin–orbit-coupled fermi gases

In the previous sections, we have presented a thorough study of the phase diagram of the four-Fermi–Wilson model (10), combining various tools developed by the condensed-matter, high-energy physics and quantum-information communities. We have seen that large-N methods yield a powerful tool to identify how the QAH phases are modified by interactions, and to understand the nature of the topological and symmetry-breaking phase transitions. By focusing on the strong-coupling limit, we have also shown that the effective super-exchange interactions leading to a quantum compass model (31) can yield more accurate estimates of the position of the critical lines and, eventually, the corresponding scaling of the underlying strongly-coupled fixed point. This follows from our comparison of the large-N predictions with two different variational methods for the compass model, which shows a clear deviation of the critical lines using the more-accurate iPEPS algorithm. Thus, it would be interesting if future work could apply this method to the full fermionic model, rather than the effective compass model, in order to explore arbitrary couplings. Another promising approach in this direction would be to use the discrete-time formulation based on Euclidean LFT (79)–(81) with dimensionless fields (82), in combination with Monte Carlo sampling techniques. In this way, one may evaluate thermodynamic observables based on the partition function of the model (57) beyond the large-N limit. In this section, we discuss yet another alternative, that of quantum simulations (QSs) [93,94], where one exploits quantum-mechanical hardware to simulate a specific quantum many-body problem. We emphasize that these QSs have the potential of overcoming some of the limitations of the above alternatives to large-N methods, as they could probe real-time dynamics regardless of entanglement growth, and would not be limited by any sign problem as one explores finite fermion densities.

In this section, we focus on QSs based on ultracold atoms in optical lattices [92]. We present a detailed scheme for the QS of the four-Fermi–Wilson model using the so-called Raman optical lattices [121–126]. These quantum simulators can be considered as Fermi gases with a specific synthetic spin–orbit coupling [118–120], mimicking the coupling of the intrinsic angular momentum of the electron with its own motion [230] in the solid state [231,232]. Spin–orbit coupling has turned out to be a source of important recent developments in condensed matter, as it underlies the experimental discovery [233,234] of a new mechanism for the ordering of matter [41,42,235] in topological insulators and superconductors [25,26,29]. Given the special role of Chern insulators and the QAH effect within these topological phases, it does not come as a surprise that spin–orbit coupling is somehow disguised in our four-Fermi–Wilson model (10). Additionally, given that the

spin–orbit coupling is directly accounted for by the Dirac equation [236,237] and, ultimately, by quantum electrodynamics [238], it is natural that our discretization of a QFT of self-interacting Dirac fermions is also connected to spin–orbit coupling. Let us now discuss this connection in detail for our representation of the Clifford algebra (2).

Note that in $(2+1)$ spacetime dimensions, one can define rotations R of angle θ around the normal vector of the spatial plane, which are generated by

$$\boldsymbol{x} \to R\boldsymbol{x} = \mathrm{e}^{\theta \mathsf{M}}\boldsymbol{x}, \quad \mathsf{M} = \begin{pmatrix} 0 & 0 & 0 \\ 0 & 0 & -1 \\ 0 & 1 & 0 \end{pmatrix}. \tag{114}$$

For our particular choice of gamma matrices (2), the spinor representation of this rotation, which belongs to the Lorentz group $R \in SO(1,2)$, is generated by $\mathsf{S} = \frac{1}{4}[\gamma^1, \gamma^2] = -\frac{\mathrm{i}}{2}\gamma^0$, such that the fields transform as

$$\Psi(\boldsymbol{x}) \to S(R)\Psi(R\boldsymbol{x}) = \mathbb{I}_N \otimes \mathrm{e}^{\mathrm{i}\frac{\theta}{2}\gamma^0}\Psi(R\boldsymbol{x}). \tag{115}$$

As noted in Section 4.1, the $\theta = \pi$ rotation leads, up to an irrelevant phase, to the inversion symmetry defined in Eq. (61). Since this transformation can be generated infinitesimally, it does not correspond to parity symmetry.

In light of Eq. (115), the two spinor components for each flavour $\psi_{\mathrm{f},1}(\boldsymbol{x})$, $\psi_{\mathrm{f},2}(\boldsymbol{x})$ in the original QFT (1) can be identified with the spin up/down states of the fermions, respectively. From this perspective, the tunnellings of the naive discretization of the Hamiltonian field theory in Eq. (6), namely $\Psi^\dagger(\boldsymbol{x})\frac{\mathrm{i}\sigma^x}{2a_2}\Psi(\boldsymbol{x}+a_2\boldsymbol{e}_2) - \Psi^\dagger(\boldsymbol{x})\frac{\mathrm{i}\sigma^y}{2a_1}\Psi(\boldsymbol{x}+a_1\boldsymbol{e}_1)$, are understood as the finite-difference discretization of the so-called Rashba spin–orbit coupling $\boldsymbol{e}_3\cdot(\boldsymbol{p}\wedge\boldsymbol{\sigma}) = \mathrm{i}\sigma^x\partial_y - \mathrm{i}\sigma^y\partial_x$ [231], when written in terms of fermionic creation/annihilation operators in second quantization. From this perspective, the complete Wilson-type discretization in Eq. (10) can be considered as a Dirac-type spin–orbit coupling that generalizes the aforementioned Rashba terms [120].

Once the connection to spin–orbit coupling has been clarified, we can exploit the ideas underlying the cold-atom QSs of synthetic spin–orbit coupling in optical lattices and, in particular, we discuss how the schemes in [121,122] can be adapted with minor modifications to realize our four-Fermi–Wilson model (10), as briefly discussed in [117]. We also note that the recent experimental realization of the Qi–Wu–Zhang model using Raman optical lattices [126] is related to the non-interacting limit of our four-Fermi–Wilson model (10).

6.1. Raman Optical lattices and spin-flip tunnellings

Let us consider a gas of fermionic atoms, such as the alkali-earth ^{87}Sr gas, which are subjected to interfering laser beams that generate a cubic optical potential [239], namely

$$V_{\mathrm{ac}}(\boldsymbol{r}) = \sum_j V_{0,j}\cos^2(k_j r_j). \tag{116}$$

Here, $j \in \{1,2,3\}$ now labels all three spatial axes, $\boldsymbol{k}_j = k_j\boldsymbol{e}_j$ is the wave-vector of the laser beams with mutually-orthogonal polarizations $\boldsymbol{\epsilon}_j$ (see the blue and green arrows in Fig. 20**(a)**), which interfere along the j-axis and lead to a standing-wave pattern. We have also introduced $V_{0,j}$ as the amplitude of the corresponding ac-Stark shift experienced by the atoms in the groundstate manifold $|^1\mathrm{S}_0, F, M\rangle$, where $F = 9/2$ is the total angular momentum, and $M \in \{-9/2, -7/2, \ldots, 9/2\}$ are the 10 possible Zeeman sub-levels split by an additional external magnetic field $\boldsymbol{B}_{\mathrm{ex}}$ (we chose z as the quantization axis in Fig. 20**(a)**). In this work, it suffices to focus on two such hyperfine levels in order to define the spinor components $|\sigma\rangle \in \{|\uparrow\rangle = |^1\mathrm{S}_0, F, M_\uparrow\rangle, |\uparrow\rangle = |^1\mathrm{S}_0, F, M_\downarrow\rangle\}$, choosing $M_\uparrow, M_\downarrow$ in a way that the electric-dipole selection rules allow one to connect these levels via two-photon Raman transitions. These two states can be isolated from the remaining hyperfine levels in the groundstate manifold by exploiting a Zeeman shift, or an ac-Stark shift as in the case of the ^{87}Sr gas [126], which must depend non-linearly on the magnetic number M_σ.

In order to induce the Raman transitions, one needs to drive off-resonant couplings to states within the excited-state manifold $|e_\sigma\rangle \in |^3\mathrm{P}_1, F'_\sigma, M'_\sigma\rangle$, which requires using large detunings Δ_j to

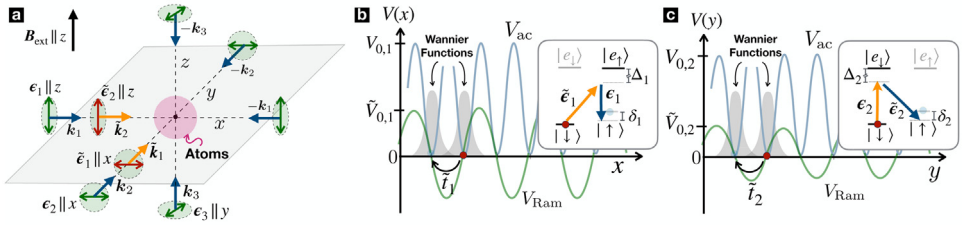

Fig. 20. Spin-flip tunnelling in a Raman optical lattice: **(a)** Atom cloud subjected to a cubic optical lattice stemming from the three pairs of counter-propagating laser beams depicted by blue arrows, all of which have mutually orthogonal polarizations depicted by green arrows. In the *xy* plane, we apply additional laser beams in a travelling-wave configuration (orange arrows) which can induce Raman transitions between two hyperfine groundstates $|\uparrow\rangle \leftrightarrow |\downarrow\rangle$ by absorbing a photon from this beam, and then subsequently emitting it in the standing wave, as depicted in the insets of **(b)** and **(c)**. In these two panels **(b)** and **(c)**, we depict the corresponding optical-lattice and Raman-lattice potentials, which lead to spin-flip tunnellings of strength $\tilde{t}_j$ due to the overlap of the neighbouring Wannier functions, mediated by the recoil of the laser beams. (For interpretation of the references to colour in this figure legend, the reader is referred to the web version of this article.)

minimize spontaneous photon emission and the associated heating mechanisms, as depicted in the insets of Figs. 20**(b)** and **(c)**. These drivings can be obtained by two additional laser beams in a travelling-wave configuration, selecting their wave-vectors $\tilde{\boldsymbol{k}}_j$ and polarizations $\tilde{\boldsymbol{\epsilon}}_j$ (see the orange and red arrows in Fig. 20**(a)**), following the general ideas of the schemes of synthetic spin–orbit coupling to create a Raman potential [120–122]. We note that a standing-wave pattern for these Raman beams can also be used which, in analogy to the optical-lattice potential (116), can be obtained by exploiting retro-reflecting mirrors [240], and underlies the recent implementation of synthetic spin–orbit coupling with the ^{87}Sr gas [126]. We would also like to remark that there have been other realizations of synthetic spin–orbit coupling that do not rely on Raman lattice potentials, using alkaline-earth [241,242] and lanthanide [243–245] atoms. In comparison to the alkalis, these atomic systems have ultra-narrow optical transitions and a larger fine-structure splitting of the excited states, which can be exploited for the QS of synthetic spin–orbit coupling minimizing the heating caused by the residual spontaneous emission from the excited-state manifold [246,247], as originally discussed in the context of synthetic gauge fields [248,249]. As discussed in the following paragraphs, these nice features can also be exploited for the generation of Raman lattice potentials.

Let us start by focusing on the Raman transition along the *x* axis (see Fig. 20 **(b)**). This transition is implemented by the standing-wave beams along the *x* direction, and an additional Raman beam with wave-vector $\tilde{\boldsymbol{k}}_1$, polarization $\tilde{\boldsymbol{\epsilon}}_1$ and relative phase ϕ_1, which propagates in a travelling-wave configuration along the *y* axis (see Fig. 20**(a)**). As depicted in the inset of Fig. 20**(b)**, since the standing wave is linearly polarized along the quantization direction, it can couple one of the groundstate spinors $|\sigma\rangle$ to an excited state $|e_\sigma\rangle$ with the same magnetic number. On the other hand, since the Raman beam is linearly polarized along a different direction, which corresponds to a linear combination of the two circular polarizations, it can impart the required angular momentum onto the atoms to connect this excited state to a groundstate spinor component of a different magnetic number through a dipole-allowed transition, i.e. $M_\downarrow = M_\uparrow \pm 1$. For the Raman transition along the *y* axis, the description is analogous (see Fig. 20**(c)**), but it is now the standing wave which can impart momentum into the atoms, whereas the Raman beam propagating along $\tilde{\boldsymbol{k}}_2$ has linear polarization $\tilde{\boldsymbol{\epsilon}}_2$ along the quantization axis. As discussed in more detail below, it is important to control the phase ϕ_2 of this second Raman process relative to ϕ_1.

As depicted in the insets of Figs. 20**(b)** and **(c)**, when the detunings with respect to the excited states Δ_j are very large, the two-photon processes only involve the spinor levels. Due to the participation of the standing wave, the Raman transition has a periodic intensity depicted with a green solid line in Figs. 20**(b)**–**(c)**, which has a doubled period with respect to the optical-lattice potentials depicted with blue solid lines (116). Altogether, the groundstate spinors $|\sigma\rangle$ are subjected

to the Raman potential

$$V_{\mathrm{Ram}}(\boldsymbol{r}) = \frac{\tilde{V}_{0,1}}{2}\cos(k_1 x)\mathrm{e}^{\mathrm{i}(\tilde{k}_1 y - \delta_1 t + \phi_1)}\sigma^+ + \mathrm{H.c.} + \frac{\tilde{V}_{0,2}}{2}\cos(k_2 y)\mathrm{e}^{\mathrm{i}(\tilde{k}_2 x - \delta_2 t + \phi_2)}\sigma^+ + \mathrm{H.c.}, \tag{117}$$

where we have introduced $\sigma^+ = |\uparrow\rangle\langle\downarrow|$, $\tilde{V}_{0,j}$ (δ_j) is the Rabi frequency (detuning) of the Raman transition driven by the jth travelling wave, and we work in the interaction picture with respect to the atomic transition, such that δ_j are the detunings of the laser beatnotes with respect to the transition frequency (see the insets of Figs. 20**(b)**–**(c)**). Let us note that, in principle, there can also be two-photon contributions from the standing- and travelling-wave beams that propagate along the same axis, but these will be highly off-resonant and contribute with higher-order shifts of the energy levels, which can be taken into account by adjusting the laser frequencies.

The gas of neutral atoms of mass m subjected to the total potential $V(\boldsymbol{r}) = V_{\mathrm{ac}}(\boldsymbol{r}) + V_{\mathrm{Ram}}(\boldsymbol{r})$ is described in second quantization, as customarily [92,97], and leads to the following non-relativistic Hamiltonian field theory

$$H = \int \mathrm{d}^3 r \sum_{\sigma,\sigma'} \Phi_\sigma^\dagger(\boldsymbol{r})\left(-\frac{\nabla_{\boldsymbol{r}}^2}{2m} + \langle\sigma|V(\boldsymbol{r})|\sigma'\rangle\right)\Phi_{\sigma'}(\boldsymbol{r}) + \int \mathrm{d}^3 r \int \mathrm{d}^3 r' \sum_{\sigma,\sigma'} \Phi_\sigma^\dagger(\boldsymbol{r})\Phi_{\sigma'}^\dagger(\boldsymbol{r}')\frac{2\pi a_s}{m}\delta(\boldsymbol{r}-\boldsymbol{r}')\Phi_{\sigma'}(\boldsymbol{r}')\Phi_\sigma(\boldsymbol{r}), \tag{118}$$

where $\Phi_\sigma^\dagger(\boldsymbol{r})$, $\Phi_\sigma(\boldsymbol{r})$ are the creation/annihilation fields of fermionic atoms at position $\boldsymbol{r}$ in the internal state σ, and we have introduced the so-called s-wave scattering length a_s, which determines the strength of the contact two-body collisions for these dilute and ultra-cold atomic gases.

We consider that all the laser beams have the same wavelength $k_j = \tilde{k}_j =: k = 2\pi/\lambda$, $\forall j$, such that they can actually be generated from a single laser source, using acousto-optical modulators to control the detunings $\delta_1 = \delta_2 =: \delta$. To obtain a lattice field theory, we make use of the Wannier basis [250] in

$$\Phi_\sigma(\boldsymbol{r}) = \sum_{\boldsymbol{n}} w(\boldsymbol{r} - \boldsymbol{r}_{\boldsymbol{n}}^0) f_{\boldsymbol{n},\sigma}. \tag{119}$$

As depicted in Figs. 20**(b)**–**(c)**, the Wannier functions $w(\boldsymbol{r} - \boldsymbol{r}_{\boldsymbol{n}}^0)$ are localized around the minima of the blue-detuned ac-Stark shift (116), namely

$$\boldsymbol{r}_{\boldsymbol{n}}^0 = \sum_j \frac{\lambda}{2}(n_j + \tfrac{1}{2})\boldsymbol{e}_j, \tag{120}$$

where $n_j \in \mathbb{Z}_{N_j}$. In Eq. (119), $f_{\boldsymbol{n},\sigma}^\dagger, f_{\boldsymbol{n},\sigma}$ are dimensionless creation-annihilation operators of fermions in the lowest band of the optical lattice. As realized in the seminal works [251,252], in the regime of deep optical lattices, where the potential barriers are much larger than the recoil energy $|V_{0,j}| \gg E_{\mathrm{R}} = k^2/2m$, the atoms are tightly confined within the minima, and the Hamiltonian field theory (118) can be expressed in terms of a lattice model with nearest-neighbour couplings. For instance, the kinetic, ac-Stark shift and interaction potentials lead to a spin-conserving tunnelling and density–density interactions

$$H_{\mathrm{sc}} = \sum_{\boldsymbol{n}}\left(\sum_{\sigma,j}\left(-t_j f_{\boldsymbol{n},\sigma}^\dagger f_{\boldsymbol{n}+\boldsymbol{e}_j,\sigma} + \mathrm{H.c.}\right) + \sum_{\sigma\neq\sigma'}\frac{U_{\uparrow\downarrow}}{2} n_{\boldsymbol{n},\sigma} n_{\boldsymbol{n},\sigma'}\right), \tag{121}$$

where the fermion number operators are $n_{\boldsymbol{n},\sigma} = f_{\boldsymbol{n},\sigma}^\dagger f_{\boldsymbol{n},\sigma}$. Here, the tunnelling amplitudes

$$t_j = \frac{4}{\sqrt{\pi}} E_{\mathrm{R}}\left(\frac{V_{0,j}}{E_{\mathrm{R}}}\right)^{\frac{3}{4}} \mathrm{e}^{-2\sqrt{\frac{V_{0,j}}{E_{\mathrm{R}}}}}, \tag{122}$$

and interaction strengths

$$U_{\uparrow\downarrow} = \sqrt{\frac{8}{\pi}} k a_s E_R \left(\frac{V_{0,1} V_{0,2} V_{0,3}}{E_R^3} \right)^{\frac{1}{4}}, \tag{123}$$

are obtained by overlap integrals of the Wannier functions, weighted by the kinetic and ac-Stark potentials or the interaction potential, respectively [92]. Note that these overlaps can in principle couple neighbouring sites that lie further apart, but the corresponding strengths decay exponentially fast with distance [251], and are thus routinely neglected. By increasing the standing-wave intensity along the z-axis, such that $V_{0,3} \gg V_{0,1}, V_{0,2}$, the dynamics of the atoms along the z direction is effectively frozen, and Eq. (121) corresponds to the 2D Fermi–Hubbard model [7,253] which, as discussed in the introduction, is a paradigm in the physics of strongly-correlated materials [8,12]. This Hamiltonian will be supplemented by additional tunnelling terms stemming from the Raman potential (117), which we now discuss in detail.

A crucial ingredient of the QSs of synthetic spin–orbit coupling using Raman potentials [120] is that, due to the specific form of the light interference in Eq. (117), the corresponding overlaps of Wannier functions cannot contribute with local Raman transitions whereby an atom remains tightly trapped in a minimum of the optical potential, while its spin gets flipped $|\uparrow\rangle \leftrightarrow |\downarrow\rangle$. In the scheme of Figs. 20**(b)**–**(c)**, the vanishing of these on-site spin flips could be easily understood in the limit of weak Raman potentials $|\tilde{V}_{0,j}| \ll |V_{0,j}|$, as a consequence of the zero value of this potential at the minima of the optical lattice (120). Remarkably, due to our choice of equal laser wave-vectors, symmetry arguments allow to prove that this is not limited to weak potentials. Mathematically, whereas the Wannier functions localized with respect to a single site are even with respect to lattice inversion about the site centre (120) (see the schematic drawing in Figs. 20**(b)**–**(c)**), the Raman potential (117) is odd, such that the corresponding overlap integrals vanish. The situation changes for the overlap between nearest-neighbour Wannier functions, as the above symmetry argument no longer applies in the direction of tunnelling. These overlaps lead to a non-zero spin-flip tunnelling with a complex-valued amplitude

$$H_{\mathrm{sf}} = -\sum_{\boldsymbol{n},j} \left(\mathrm{i}\tilde{t}_j \mathrm{e}^{\mathrm{i}(\delta t - \phi_{j,\boldsymbol{n}})} \left(f^\dagger_{\boldsymbol{n},\uparrow} f_{\boldsymbol{n}+\mathbf{e}_j,\downarrow} - f^\dagger_{\boldsymbol{n},\uparrow} f_{\boldsymbol{n}-\mathbf{e}_j,\downarrow} \right) + \mathrm{H.c.} \right). \tag{124}$$

The modulus of the tunnelling, $\tilde{t}_j$, can be estimated analytically by approximating the optical-lattice potential around the minima (120) by a harmonic oscillator of frequencies $\nu_j = 2\sqrt{V_{0,j} E_R}$ along each axis, such that the Wannier functions become a separable product of Gaussians. When tunnelling along the $x(y)$ axis, the above symmetry argument can still be applied to neglect the $\mathrm{Re}\{\mathrm{e}^{\mathrm{i}\tilde{k}_1 y}\}$ ($\mathrm{Re}\{\mathrm{e}^{\mathrm{i}\tilde{k}_2 x}\}$) contribution of the Raman potential (117) to the overlap integral along the $y(x)$ axis. On the other hand, the $\mathrm{Im}\{\mathrm{e}^{\mathrm{i}\tilde{k}_1 y}\}$ ($\mathrm{Im}\{\mathrm{e}^{\mathrm{i}\tilde{k}_2 x}\}$) part gives a non-zero contribution multiplying the overlaps along the $x(y)$ axis, and leads to

$$\tilde{t}_j = \frac{\tilde{V}_{0,j}}{2} \left(\mathrm{e}^{-\frac{\pi^2}{4}\sqrt{\frac{V_{0,j}}{E_R}} - \frac{1}{2}\sqrt{\frac{E_R}{V_{0,j}}}} \right). \tag{125}$$

In addition, one obtains a site-dependent phase

$$\phi_{j,\boldsymbol{n}} = \phi_j - \pi(n_1 + n_2). \tag{126}$$

In the schemes of Figs. 20**(b)**–**(c)**, the alternation of the signs of the spin-flip tunnellings $\mathrm{e}^{\mathrm{i}\phi_{j,\boldsymbol{n}}} = (-1)^{n_1+n_2}\mathrm{e}^{\mathrm{i}\phi_j}$ can be understood as a consequence of the doubled period of the Raman potential with respect to the optical lattice, which leads to alternating signs of the linear slopes of the Raman potential as one moves along the tunnelling direction. As discussed in the following subsection, this is another crucial property for the QS of our four-Fermi–Wilson model.

6.2. Four-Fermi–Wilson quantum simulator

Once we have obtained the microscopic Hamiltonian governing the dynamics of the two-component atoms in a deep optical Raman potential, we can discuss how this can be mapped via a

$U(2)$ gauge transformation, followed by a rescaling, to the four-Fermi–Wilson model of Eq. (10) in the single-flavour limit $\mathfrak{f} = 1 = N$. This transformation is

$$\begin{aligned}\psi_{\mathfrak{f},1}(\boldsymbol{x}) &= \frac{1}{\sqrt{a_1 a_2}} \mathrm{e}^{-\mathrm{i}\frac{\delta}{2}t} f_{\boldsymbol{n},\uparrow},\\ \psi_{\mathfrak{f},2}(\boldsymbol{x}) &= \frac{1}{\sqrt{a_1 a_2}} \mathrm{e}^{\mathrm{i}\frac{\delta}{2}t + \mathrm{i}\pi(n_1+n_2)} f_{\boldsymbol{n},\downarrow}.\end{aligned} \tag{127}$$

The time-dependence can be understood as a change from the aforementioned interaction picture to the so-called rotating frame, such that the detunings correspond to an energy imbalance that will contribute to the bare mass. In addition, the site-dependent phase transformation allows us to rewrite the model in a translationally-invariant manner, making direct connection with the starting point for the lattice discretization of our four-Fermi–Wilson QFT discussed in Section 2.2.

As discussed in [117], the dependence on the relative phases ϕ_j generalizes previous schemes for synthetic spin–orbit coupling [121,122], which can be exploited to connect precisely to our four-Fermi–Wilson models. Setting the Raman-beam phases to $\phi_1 = 0, \phi_2 = \pi/2$, we find that the sum of the spin-conserving (121) and spin-flipping (124) Hamiltonians maps directly to the lattice field theory (10) with the following correspondence of the microscopic parameters

$$a_j = \frac{1}{2\tilde{t}_j}, \quad r_j = \frac{t_j}{\tilde{t}_j}, \quad m = \frac{\delta}{2} - 2(t_1 + t_2), \quad g^2 = \frac{U_{\uparrow\downarrow}}{4\tilde{t}_1\tilde{t}_2}. \tag{128}$$

Accordingly, the bare mass m can be controlled by the detuning of the Raman beams, whereas the coupling strength g^2 is proportional to the s-wave scattering length (123), and can thus be modified independently via a Feshbach resonance [113]. Alternatively, since it is inversely proportional to the spin-flip tunnellings (125), one can tune this parameter by modifying the corresponding potential depths $V_{0,j}$ or $\tilde{V}_{0,j}$. At this point, it is worth mentioning that the recent experimental realization of the Qi–Wu–Zhang model with the ^{87}Sr gas [126] is related to the non-interacting limit of our four-Fermi–Wilson model (10) by a simple $SU(2)$ rotation of gamma matrices (2) that makes $\sigma^x \leftrightarrow \sigma^y$. In this case, the experiment uses standing-wave Raman beams, and their relative phase enters differently in the microscopic Hamiltonian. The only important point is that this phase difference is $\pi/2$. In the presence of the Hubbard interactions, this would only lead to an interchange of the two symmetry-breaking channels. We thus believe that these experiments are a very promising route to explore the physics discussed in our work.

In this regard, it is important to note that the effective lattice spacings a_j are not set by the optical-lattice wavelength $\lambda/2$, but rather by the inverse of the spin-flip tunnelling strengths, which are proportional to the Rabi frequency of the Raman beams (125), and can thus be tuned by changing the corresponding laser power. Since this laser power can be different along the x, y axes, the cold-atom QS can also explore different anisotropies for the spatial $\xi_2 = a_1/a_2$, and Wilson parameters r_j. In this manuscript, we have explored in detail the limit $r_j = 1$, which would require equal spin-conserving and spin-flip tunnellings. We note, however, that non-unity Wilson parameters $r_j \neq 1$ will simply rescale the axes but maintain the same shape of the non-interacting phase diagram. As the interactions are switched on, we expect that $r_j \approx 1$ will not introduce additional strong-coupling phases. Exploring larger $r_j \gg 1$ or smaller values $r_j \ll 1$ is left for future studies, which could also be targeted by the proposed QS.

Let us now comment on the observable consequences of the $U(2)$ gauge transformation (127). The time-dependence due to the rotating frame is customary in quantum optics, and can be accounted for during the measurement process. The local site-dependent phase can change the interpretation of the symmetry-breaking order parameters related to the π-field condensates, while they do not change the σ-field scalar condensate. One can easily check that

$$\begin{aligned}\Sigma &\propto \langle f^\dagger_{\boldsymbol{n},\uparrow} f_{\boldsymbol{n},\uparrow} - f^\dagger_{\boldsymbol{n},\downarrow} f_{\boldsymbol{n},\downarrow}\rangle,\\ \Pi_1 &\propto (-1)^{n_1+n_2} \langle f^\dagger_{\boldsymbol{n},\uparrow} f_{\boldsymbol{n},\downarrow} + f^\dagger_{\boldsymbol{n},\downarrow} f_{\boldsymbol{n},\uparrow}\rangle,\\ \Pi_2 &\propto (-1)^{n_1+n_2} \langle \mathrm{i} f^\dagger_{\boldsymbol{n},\downarrow} f_{\boldsymbol{n},\uparrow} - \mathrm{i} f^\dagger_{\boldsymbol{n},\uparrow} f_{\boldsymbol{n},\downarrow}\rangle.\end{aligned} \tag{129}$$

Accordingly, in the language of the cold-atom QS, a non-zero value of the scalar condensate corresponds to an atomic density imbalance between the two hyperfine groundstates. For the Lorentz-breaking Π_j condensates the situation changes, as a non-zero value marks an alternating pattern that turns the orbital ferromagnets FM_x (FM_y) into Néel-ordered anti-ferromagnets AFM_x (AFM_y). In order to prepare these phases, as well as the correlated QAH or trivial band insulators discussed in this manuscript, one would start by preparing an ultra-cold spin-polarized Fermi gas by optical pumping, and then adiabatically ramping up the ac-Stark and Raman potentials to create the non-interacting groundstate for specific values of ma_1, ξ_2. One could then adiabatically change the coupling strength g^2/a_1. According to Eq. (128), one can increase the Hubbard interactions via a Feshbach resonance, or decrease the spin-flip tunnellings, until the desired point of parameter space $(ma_1, \xi_2, g^2/a_1)$ is reached. Once this groundstate is approximately prepared, let us discuss possible characterization techniques in the experiment.

Note that the scalar condensate (129) can be inferred by spin-resolved in-situ imaging, where the trapped atoms are illuminated by an incoming laser and cast a shadow on a CCD-camera that is used to extract the integrated, so-called columnar, density of the atoms [254,255]. Absorptive [256] and dispersive [257] techniques can be applied in subsequent shots with lasers addressing each of the internal states separately, such that $\rho_\sigma(\boldsymbol{x}) = \langle \Phi^\dagger_\sigma(\boldsymbol{x})\Phi_\sigma(\boldsymbol{x})\rangle$ can be reconstructed from the spin-resolved columnar densities. To get lattice-site resolution for $\langle f^\dagger_{\boldsymbol{n},\sigma} f_{\boldsymbol{n},\sigma}\rangle$, one can exploit the so-called quantum gas microscopes [258–263]. To achieve spin resolution, one may separate different spin components spatially prior to the microscope imaging [264,265]. Alternatively, one can remove the atoms with a specific spin state by shining resonant light before the imaging [266,267]. Finally, in order to infer the values of the Π_j condensates, one would need to apply an additional microwave/Raman term that drives a $\pi/2$ rotation of the spins on the Bloch sphere in Fig. 5**(a)**. Controlling the phase of this rotation, provided that it is locked to the rotating frame of the original Raman beams, one can map the differential spin population to the x or y axis, such that the subsequent quantum-gas-microscope imaging gives the desired information about the Lorentz-breaking condensates (129).

Density imaging can also be performed after switching off the confining potential, which leads to the so-called time-of-flight (TOF) imaging. If the density is imaged after a sudden release [252], one gains information about the coherence properties of the system in momentum space [92]. Instead of the sudden release, one can adiabatically ramp-down the lattice potential, which gives access to the quasi-momentum atomic distribution through the so-called band-mapping technique [268,269]. In Ref. [109], this band-mapping technique was used to measure the differential drift of the atom cloud when subjected to two opposite gradients, which allows one to distinguish trivial from non-trivial Berry curvatures in Haldane's honeycomb model of the QAH effect. This type of measurements could be used to infer the value of the Chern number [270,271], as has been demonstrated in cold-atom experiments of the integer QHE [272].

Coming back to the QAH effect, we note that the spin-resolved TOF densities have been measured in quasi-momentum space for the simulated Qi–Wu–Zhang model with the ^{87}Sr gas [126]. Remarkably, exploiting a symmetry that corresponds exactly to our inversion symmetry (61), the measured differential spin densities at four high-symmetry points of the Brillouin zone give experimental access to the Chern number [273]. These points correspond to the centre Γ, edge centres M and corner R where the fermion doublers reside, as discussed below Eq. (17). According to our discussion of the static self-energy and the topological Hamiltonian in Section 5.2, we expect that these spin densities will get renormalized by the non-zero scalar condensate, but still serve to characterize the topological invariant in the presence of interactions in an analogous fashion to our Eq. (112). It would be interesting to combine this observable, together with the in-situ symmetry-breaking Π_1 (Π_2) condensates, to explore the full phase diagram of the model and the topological and symmetry-breaking phase transitions. We note that, in this case, the condensates would change into AFM_y (AFM_x) Néel orders due to the alternation in Eq. (129), and the $\sigma^x \to \sigma^y$ change of the different implementation of the Raman lattice.

Before closing this section, we emphasize that recovering the continuum limit of the lattice field theory (10) implemented by the cold-atom QS does not imply a drastic modification of the laser wavelength $\lambda \to 0$. Instead, it requires setting the microscopic parameters $(t_j, \tilde{t}_j, \delta, U_{\uparrow\downarrow})$ to certain

values, such that the bare couplings $(ma_1, \xi_2, r_j, g^2/a_1)$ lie in the vicinity of a critical point. Here, the energy gap is much smaller than the tunnellings $\Delta\epsilon \ll \tilde{t}_j$, and the relevant length scale $\xi_l \gg a_1, a_2$ leads to a continuum QFT. The question that could be addressed by the cold-atom QS is to explore this region and determine the critical scaling shedding light on the nature of the strongly-coupled fixed points of the continuum four-Fermi QFT, addressing questions that might otherwise require large-scale LFT simulations. Ultimately, the goal would be to explore different fillings and real-time dynamics in these models, going beyond the capabilities of classical simulations.

7. Conclusion and outlook

We have shown that Wilson-type discretizations of four-Fermi QFTs in (2+1) dimensions (1) with irreducible representations of the gamma matrices (2) yield a neat playground to address interesting questions in both high-energy physics and condensed matter. Although explicitly lacking chiral symmetry, these regularized QFTs present the analogue of dynamical mass generation which, in contrast to other spacetime dimensions, occurs both at a non-zero coupling strength within a renormalizable QFT with a strongly-coupled fixed point. In contrast to chiral-invariant theories, these four-Fermi–Wilson model can also host fermion condensates that break inversion symmetry spontaneously and, thus, Lorentz invariance in the continuum limit. From a condensed-matter perspective, these lattice models host QAH phases with non-zero Chern numbers, and the four-Fermi terms can be used to explore the role of interactions as one enters strongly-correlated regimes. Both of these topics are actively investigated in these two fields.

We have presented a multidisciplinary approach that combines tools from these communities to advance our understanding of these four-Fermi–Wilson models. In the strong-coupling and single-flavour limit, we have shown that the condensed-matter concept of super-exchange interactions can be used to find an effective description in terms of a 90^0 quantum compass model in a transverse field. Analysing this model with variational mean-field and tensor-network techniques, we have identified two possible symmetry-breaking channels that connect to two versions of the aforementioned Lorentz-breaking condensates. This has allowed us to formulate a large-N limit of this field theory in terms of auxiliary fields, which has been used to predict the whole extent of the condensates away from the strong-coupling limit by solving a set of non-linear gap equations. By comparing a continuum-time Hamiltonian formalism with a discrete-time Euclidean approach, we have been able to identify additive renormalizations of the bare parameters that must be carefully considered when one explores the phases of the model using the discrete-time Euclidean approach common to the lattice field theory community.

Moreover, using the Euclidean approach, we have calculated the effective potential resumming the leading-order Feynman diagrams for $N \to \infty$. This has allowed us to unveil a new type of radiative corrections that give rise to novel effects in comparison to chiral-invariant theories, such as an interesting crossover between first- and second-order phase transitions. This effective potential has also allowed us to explore regions of parameter space where the inversion symmetry remains intact, extracting the large-N contributions to the self-energy, and using those to calculate the many-body Chern numbers that characterize the groundstate and the QAH in the presence of correlations. This leads to a non-perturbative characterization of a rich phase diagram, which contains large-N Chern insulators, trivial band insulators, and Lorentz-breaking fermion condensates separated by various critical lines, around which one can recover continuum QFTs and explore the nature of the corresponding strongly-coupled fixed points.

Finally, we have shown that quantum simulators based on ultra-cold alkali-earth atoms trapped in optical lattices and subjected to synthetic spin–orbit coupling yield a very promising avenue to realize these four-Fermi–Wilson models in experiments. In particular, we have argued that recent experiments with a ^{87}Sr gas subjected to Raman lattice potentials [126] are related to the non-interacting limit of our four-Fermi–Wilson model, and give a unique opportunity to explore a correlated QAH effect in the laboratory. Such an implementation would benefit from the microscopic tunability of cold-atom quantum gases, which would allow to infer all of the relevant observables such as the symmetry-breaking order parameters related to the fermion condensates or the many-body Chern numbers. Moreover, these quantum simulators would open the route to the study

of real-time dynamics and finite-fermion densities, overcoming current limitations of numerical studies based on classical hardware.

As an outlook, we believe that exploiting the current multi-disciplinary view will be very interesting to explore effects that have not been covered by this article. An interesting open question is to determine the role of anisotropic Wilson parameters in the nature of the Lorentz-breaking fermion condensates, exploring if new phases can appear as one increases the interactions. We also believe that further studies of the isotropic regime $a_1 = a_2$ will be very interesting. As noted in this manuscript, there is an emerging $O(2)$ symmetry in the $\boldsymbol{\pi}(x)$ field, which can modify substantially the dynamics of the theory due to an additional Chern–Simons term that is generated by quantum corrections. In analogy to quantum electrodynamics in (2+1) dimensions, where photons acquire a mass due to a Chern–Simons term [45], the low-lying excitations about the condensate phase that breaks the $O(2)$ symmetry spontaneously can also acquire a non-zero mass. It will be very interesting to explore this phenomenon in the presence of boundaries, since there can be an interplay with the QAH effect and the topological edge states. Finally, we finish by mentioning that the cold-atom quantum simulators would open a new route to the study of real-time dynamics and finite-fermion densities, overcoming current limitations of numerical studies based on classical hardware. In the future, it will be very interesting to exploit this multidisciplinary view and to identify new interaction-induced topological phases, such as fractional Chern insulators.

Declaration of competing interest

The authors declare that they have no known competing financial interests or personal relationships that could have appeared to influence the work reported in this paper.

Acknowledgements

The ICFO group acknowledges support from ERC AdG NOQIA, State Research Agency AEI (“Severo Ochoa” Center of Excellence CEX2019-000910-S) Plan National FIDEUA PID2019-106901GB-I00 project funded by MCIN/AEI /10.13039/501100011033, FPI, QUANTERA MAQS PCI2019-111828-2 project funded by MCIN/AEI /10.13039/501100011033, Proyectos de I+D+I “Retos Colaboración” RTC2019-007196-7 project funded by MCIN/AEI /10.13039/501100011033, Fundació Privada Cellex, Fundació Mir-Puig, Generalitat de Catalunya (AGAUR Grant No. 2017 SGR 1341, CERCA program, QuantumCAT U16-011424, co-funded by ERDF Operational Program of Catalonia 2014–2020), EU Horizon 2020 FET-OPEN OPTOLogic (Grant No 899794), and the National Science Centre, Poland (Symfonia Grant No. 2016/20/W/ST4/00314), Marie Skłodowska-Curie grant STREDCH No 101029393, “La Caixa” Junior Leaders fellowships (ID100010434), and EU Horizon 2020 under Marie Skłodowska-Curie grant agreement No. 847648 (LCF/BQ/PI19/11690013, LCF/BQ/PI20/11760031, LCF/BQ/PR20/11770012).). A.B. acknowledges support from the Ramón y Cajal program RYC-2016-20066, CAM/FEDER Project S2018/TCS- 4342 (QUITEMADCM), and PGC2018-099169-B-I00 (MCIU/AEI/FEDER, UE). S.J.H. acknowledges the support of STFC grant ST/T000813/1.

Appendix A. Absence of two simultaneous π condensates

In this Appendix, we give a detailed account of the gap equations obtained by using a Hubbard–Stratonovich transformation to rewrite the action (58) in terms of two π fields, and show that there cannot be a simultaneous condensation for general anisotropies.

To find the effective action in terms of the $\sigma(x)$ and $\boldsymbol{\pi}(x) = (\pi_1(x), \pi_2(x))$ auxiliary fields, we note that in the single-flavour limit $N = 1$ one can exactly rewrite the quartic interaction as the combination $(\overline{\Psi}(\boldsymbol{x})\Psi(\boldsymbol{x}))^2 \rightarrow \frac{1}{3}((\overline{\Psi}(\boldsymbol{x})\gamma^1\Psi(\boldsymbol{x}))^2 + (\overline{\Psi}(\boldsymbol{x})\gamma^2\Psi(\boldsymbol{x}))^2 + (\overline{\Psi}(\boldsymbol{x})\Psi(\boldsymbol{x}))^2)$, such that the auxiliary fields can be introduced symmetrically. We proceed by assuming once more that the

corresponding condensates are homogeneous, i.e. $\Sigma(\boldsymbol{x}) = \Sigma$, $(\Pi_1(\boldsymbol{x}), \Pi_2(\boldsymbol{x})) = (\Pi_1, \Pi_2) = \boldsymbol{\Pi}$, such that the effective action is now

$$S_E = \int_0^\beta \mathrm{d}\tau \left(\frac{3NA_s}{2g^2} \left(\Sigma^2 + \boldsymbol{\Pi}^2\right) + \sum_{\boldsymbol{k}\in \mathrm{BZ}} \Psi^\star_{\boldsymbol{k}}(\tau)\big(\partial_\tau + h_{\boldsymbol{k}}(m+\Sigma, \boldsymbol{\Pi})\big)\Psi_{\boldsymbol{k}}(\tau) \right). \tag{A.1}$$

Here, in analogy to the derivation for a single π channel presented in Section 4.1, we find that the single-particle Hamiltonian (13) gets modified to

$$h_{\boldsymbol{k}}(m) \to h_{\boldsymbol{k}}(m+\Sigma, \boldsymbol{\Pi}) = \boldsymbol{d}_{\boldsymbol{k}}(m+\Sigma, \boldsymbol{\Pi}) \cdot (\mathbb{I}_N \otimes \boldsymbol{\sigma}). \tag{A.2}$$

where the vector (14) also gets modified $\boldsymbol{d}_{\boldsymbol{k}}(m) \to \boldsymbol{d}_{\boldsymbol{k}}(m+\Sigma, \boldsymbol{\Pi})$ due to the presence of the auxiliary fields

$$\boldsymbol{d}_{\boldsymbol{k}}(m+\Sigma, \boldsymbol{\Pi}) = \boldsymbol{d}_{\boldsymbol{k}}(m) + (\Pi_1, \Pi_2, \Sigma)\,. \tag{A.3}$$

Therefore, the only differences with respect to Section 4.1 are that the couplings strength $g^2 \to 2g^2/3$, and that this vector is simultaneously shifted by both Π_j condensates.

The rest of the derivation follows exactly the steps described in Section 4.1, and leads to a saddle point of the action that is now determined by three non-linear gap equations

$$\mathbf{I}: \quad \frac{\Sigma}{g^2} = \frac{1}{3}\int_{\boldsymbol{k}} \frac{m+\Sigma+m_W(\boldsymbol{k})}{\epsilon_{\boldsymbol{k}}(m+\Sigma, \boldsymbol{\Pi})} \tag{A.4}$$

$$\mathbf{II}: \quad \frac{\Pi_1}{g^2} = \frac{1}{3}\int_{\boldsymbol{k}} \frac{\frac{1}{a_1}\sin(k_1 a_1) + \Pi_1}{\epsilon_{\boldsymbol{k}}(m+\Sigma, \boldsymbol{\Pi})} \tag{A.5}$$

$$\mathbf{III}: \quad \frac{\Pi_2}{g^2} = \frac{1}{3}\int_{\boldsymbol{k}} \frac{\frac{1}{a_2}\sin(k_2 a_2) + \Pi_2}{\epsilon_{\boldsymbol{k}}(m+\Sigma, \boldsymbol{\Pi})}, \tag{A.6}$$

Let us note that from **II** (A.5) and **III** (A.6), it follows that

$$\int_{\boldsymbol{k}} \left(\frac{\frac{1}{\Pi_1 a_1}\sin(a_1 k_1)}{\epsilon_{\boldsymbol{k}}(m+\Sigma, \boldsymbol{\Pi})} - \frac{\frac{1}{\Pi_2 a_2}\sin(k_2 a_2)}{\epsilon_{\boldsymbol{k}}(m+\Sigma, \boldsymbol{\Pi})} \right) = 0. \tag{A.7}$$

The left hand side does not vanish for any point (σ, Π_1, Π_2) in the anisotropic case $a_1 \neq a_2$, meaning that **II** and **III** cannot be satisfied simultaneously. For $a_1 = a_2$, gap equations **II** and **III** are equal and, around this regime, Eq. (A.7) changes from being negative to positive. As a consequence, there is no condensation with two simultaneous non-zero vacuum expectation values of the π fields for generic anisotropy, meaning that we must consider either the Π_1 or the Π_2 symmetry-breaking channels individually. This is in line with the prediction of the variational mean-field where, in the language of an effective spin model, the ground state is either a x- or y-ferromagnet unless $a_1 = a_2$. This discussion implies that we can improve on the auxiliary-field description by considering two independent sets of gap equations for Σ, Π_1 and Σ, Π_2 separately.

Appendix B. Continuum-time limit and time doublers

In this Appendix, we present a detailed derivation of the additive renormalization of the bare parameters in the time-continuum limit (98) caused by the spurious time doublers (95). To get an explicit expression for this renormalization, we start from the action for dimensional fields (78), using a subscript E in the bare parameters and condensates to distinguish this discrete-time Euclidean-lattice approach from the Hamiltonian one in Eqs. (70)–(71).

After repeating similar steps as those described in Section 4.1, we obtain an effective action for the auxiliary fields, and arrive at a pair of gap equations

$$\frac{\Sigma_E}{g_E^2} = \frac{1}{Q}\sum_{\boldsymbol{k}} \frac{m_E + \Sigma_E + m_E(\boldsymbol{k})}{\mathrm{s}^2_{\boldsymbol{k}}(m_E + \Sigma_E, \Pi_{2,E})}, \tag{B.1}$$

$$\frac{\Pi_{2,E}}{g_E^2} = \frac{1}{Q}\sum_{\boldsymbol{k}} \frac{\frac{1}{a_2}\sin(k_2 a_2) + \Pi_{2,E}}{\mathrm{s}_{\boldsymbol{k}}^2(m_E + \Sigma_E, \Pi_{2,E})}, \tag{B.2}$$

where the Euclidean contribution to the mass (92) due to the Wilson-term reads, for dimensional couplings, as follows

$$m_E(\boldsymbol{k}) = \sum_{\alpha} \frac{1 - \cos(k_\alpha a_\alpha)}{a_\alpha}. \tag{B.3}$$

In the above gap equations, we have also introduced the analogue of Eq. (91) for dimensional couplings

$$\begin{aligned}\mathrm{s}_{\boldsymbol{k}}^2(m_E + \Sigma_E, \Pi_{2,E}) = (m_E + \Sigma_E + m_E(\boldsymbol{k}))^2 \\ + \sum_{\alpha} \frac{1}{a_\alpha^2}\left(\sin(k_\alpha a_\alpha) + \Pi_{\alpha,E}\delta_{\alpha,2}\right)^2.\end{aligned} \tag{B.4}$$

With these expressions at hand, let us perform a long-wavelength approximation $k_0 = K_0 + \delta k_0$ around $K_0 \in \{0, \pi/a_0\}$, such that we can identify the contributions of the physical and spurious doublers. After a Taylor expansion, and using contour techniques for the integrals along δk_0, we find that the second gap equation can be expressed as

$$\frac{\Pi_{2,E}}{g_E^2} = \frac{1}{2}\int_{\boldsymbol{k}}\left(\frac{\frac{1}{a_2}\sin(k_2 a_2) + \Pi_{2,E}}{\epsilon_{\boldsymbol{k}}\left(m_E + \Sigma_E, \Pi_{2,E}\boldsymbol{e}_2\right)} + \frac{\frac{1}{a_2}\sin(k_2 a_2) + \Pi_{2,E}}{\epsilon_{\boldsymbol{k}}(m_E + \Sigma_E + \frac{2}{a_0}, \Pi_{2,E}\boldsymbol{e}_2)}\right), \tag{B.5}$$

where $\boldsymbol{k} = (k_1, k_2)^t$, and we have made use of the single-particle energy defined in Eq. (68). We can now let $a_0 \to 0$, noticing that the mass term of the spurious time doublers, proportional to $1/a_0$, dominates in the denominator of the second term, such that the integral vanishes linearly with a_0 in this limit. Accordingly, we recover the continuum gap equation (71) for $j = 2$, which is the desired single π-channel gap equation. Let us now recall that, in our numerical solution of the gap equations, we start by fixing the value of the coupling strength g^2 and $M = m + \Sigma$, after which we solve Eq. (B.2) to get the π condensate Π_2. As we have just shown that the Euclidean-lattice gap equation (B.2) yields the same gap equation (71) in the continuum-time limit, we can thus conclude that

$$g_E^2 = g^2, \quad \Pi_{2,E} = \Pi_2. \tag{B.6}$$

The situation changes for the first gap equation (B.1), since the Wilson-term contribution (B.3) for the time doublers leads to a term that scales with $1/a_0$ also in the numerator

$$\frac{\Sigma_E}{g_E^2} = \frac{1}{2}\int_{\boldsymbol{k}}\left(\frac{m_E + \Sigma_E + m_W(\boldsymbol{k})}{\epsilon_{\boldsymbol{k}}(m_E + \Sigma_E, \Pi_{2,E}\boldsymbol{e}_2)} + \frac{m_E + \Sigma_E + \frac{2}{a_0} + m_W(\boldsymbol{k})}{\epsilon_{\boldsymbol{k}}(m_E + \Sigma_E + \frac{2}{a_0}, \Pi_{2,E}\boldsymbol{e}_2)}\right). \tag{B.7}$$

In the limit $a_0 \to 0$, the second term no longer vanishes, but yields instead

$$\frac{\Sigma_E}{g_E^2} = \frac{1}{2}\int_{\boldsymbol{k}} \frac{m_E + \Sigma_E + m_W(\boldsymbol{k})}{\epsilon_{\boldsymbol{k}}(m_E + \Sigma_E, \Pi_{2,E}\boldsymbol{e}_2)} + \frac{1}{2\,a_1\,a_2}. \tag{B.8}$$

One can readily check that this gap equation differs from the Hamiltonian one (70), which was obtained by working directly in the time-continuum limit, by a constant additive term, where we consider the single π-channel. Going back to our numerical solution of the gap equations, and the discussion above Eq. (B.6), once we have solved the second gap equation and know g_E^2 and $\Pi_{2,E}$, we can solve Eq. (B.2) to obtain the value of the scalar condensate Σ_E, and finally infer the corresponding bare mass $m_E = M - \Sigma_E$. According to the shift in Eq. (B.8), we can readily infer that the Euclidean-lattice formalism gives the same value of the scalar condensate, but renormalizes additively the bare mass

$$\Sigma_E = \Sigma, \quad m_E = m - \frac{g^2}{2a_1 a_2}. \tag{B.9}$$

When this additive renormalization is taken into account, together with the required rescalings of the adimensional formulation (82), we finally arrive to Eq. (98).

Appendix C. Derivation of the effective potential

In this Appendix, we give a detailed account of the derivation of the resummation for the effective potential (101) to all orders of the couplings strength g^2. Let us start from the most general expression with an even/odd number of auxiliary lines

$$V_{\text{eff}}(\tilde{\Pi}_2) = \frac{N\tilde{\Pi}_2^2}{2\tilde{g}^2} + N\sum_{n=1}^{\infty}\frac{1}{n}\int_{\boldsymbol{p}}\text{Tr}\left(-\text{i}\tilde{\gamma}_2\frac{\tilde{\Pi}_2}{\text{i}\not{p}+\tilde{m}}\right)^n, \tag{C.1}$$

where we recall that $\int_{\boldsymbol{p}} = \sum_{\boldsymbol{k}}$, $\not{p} = \tilde{\gamma}^\alpha p_\alpha$ with $p_\alpha = 2\kappa_\alpha \sin k_\alpha$, and our choice for the Euclidean gamma matrices is given in Eq. (80). Although these are the specific for the anisotropic Wilson-type regularization of the four-Fermi QFT, we note that the following derivations are completely generic, and can be readily applied to the continuum case and to other representations of gamma matrices. For instance, if one aims at implementing chiral symmetry using the Euclidean version of Eq. (3), the expressions below need only be modified by letting $N \to 2N$ due to the doubled dimension of the gammas.

The trace in Eq. (C.1) can be calculated analytically via an inductive method, where

$$\text{Tr}\left(-\text{i}\tilde{\gamma}_2\frac{\tilde{\Pi}_2}{i\not{p}+\tilde{m}}\right)^n = \frac{\tilde{\Pi}_2^n}{(p^2+\tilde{m}^2)^n}\text{Tr}(I_n) \tag{C.2}$$

and we have defined

$$I_n = (-\text{i}\tilde{\gamma}_2(-\text{i}\not{p}+\tilde{m}))^n. \tag{C.3}$$

One can derive a recursive relation by noting that

$$I_n = -\tilde{\gamma}_2(-\text{i}\not{p}+\tilde{m})\tilde{\gamma}_2(-\text{i}\not{p}+\tilde{m})I_{n-2} \tag{C.4}$$

$$= -(p^2+\tilde{m}^2)I_{n-2} - 2p_2 I_{n-1}. \tag{C.5}$$

In the last step, we use the anti-commutation rules $\{\tilde{\gamma}_\mu, \tilde{\gamma}_\nu\} = 2\delta_{\mu,\nu}$, and the identity $\tilde{\gamma}_2\not{p}\tilde{\gamma}_2 = -\not{p} - 2p_2\tilde{\gamma}_2$. The recurrence relation starts with the first two terms $I_0 = \mathbb{I}_2$ and $I_1 = -\text{i}\tilde{\gamma}_2(-\text{i}\not{p}+\tilde{m})$ which, considering our choice in Eq. (80) and the properties of the Pauli matrices, have the traces

$$\text{Tr}(I_0) = \text{Tr}(\mathbb{I}_2) = 2, \quad \text{Tr}(I_1) = \text{Tr}(-p_2\mathbb{I}_2) = -2p_2. \tag{C.6}$$

For higher-dimensional representations, such as Eq. (3), these traces will have an overall multiplicative factor that shall carry onto the expressions of the effective potential.

With the aid of these first two terms, and the above recurrence relation, one can develop a general expression for arbitrary n with the general structure

$$\text{Tr}(I_n) = 2\sum_{k=1}^{n} A_{nk}p_2^k(p^2+\tilde{m}^2)^{\frac{n-k}{2}}, \tag{C.7}$$

where the first few values of the coefficients A_{nk} are given in Table 1. Note that we only present the coefficients for even integers $k = 0, 2, 4, \ldots, n$, and even n. Although the odd ones $k = 1, 3, 5, \ldots, n$, for odd n, can also be non-zero, they lead to mode sums, or integrals in the continuum, which vanish (C.1), as the function is odd in a symmetric interval. In the standard calculation of the effective potential for continuum four-Fermi QFTs [112], where the σ field couples to $(\overline{\Psi}\Psi)$ for the chiral symmetry-breaking channel; the odd terms vanish directly since they are proportional to the traces of the gamma matrices, all of which vanish. For the current $(\overline{\Psi}\tilde{\gamma}_1\Psi)$ channel, although the traces do not vanish, once we integrate over the Euclidean Brillouin zone (C.1), the odd terms do not contribute either. It is for this reason that the large-N Feynman diagrams depicted in Fig. only contain an even number of auxiliary π lines, and lead to Eq. (C.1).

Table 1
Coefficients A_{nk} in the expansion of Eq. (C.7). The lower row also gives the values of the coefficients $\mathscr{A}_k$ in Eq. (C.9).

n/k	0	2	4	6	8	10	12
2	−1	2					
4	1	−8	8				
6	−1	18	−48	32			
8	1	−32	160	−256	128		
10	−1	50	−400	1120	−1280	512	
12	1	−72	840	−3584	6912	−6144	2048
$\mathscr{A}_k$		-2	$\frac{2}{3}$	$-\frac{4}{45}$	$\frac{2}{315}$	$-\frac{4}{14175}$	$\frac{4}{467775}$

In order to perform the resummation, we need to express these coefficients A_{nk} in closed from. We have found that the exact expression is

$$A_{nk} = (-1)^{\frac{n}{2}} \mathscr{A}_k \left(\frac{n}{2}\right)^2 \left(\left(\frac{n}{2}\right)^2 - 1^2\right) \cdots \left(\left(\frac{n}{2}\right)^2 - \left(\frac{k}{2} - 1\right)^2\right), \tag{C.8}$$

where we have introduced

$$\mathscr{A}_k = \frac{(-1)^{\frac{k}{2}} 2^{k-1}}{\left(\frac{k}{2}\right)^2 \left(\left(\frac{k}{2}\right)^2 - 1^2\right) \cdots \left(\left(\frac{k}{2}\right)^2 - \left(\frac{k}{2} - 1\right)^2\right)}. \tag{C.9}$$

The first values of $\mathscr{A}_k$ shown in Table 1 can be readily checked to follow this general expression. This expression (C.8) must be supplemented with the $k = 0$ term $A_{n0} = (-1)^{\frac{n}{2}}$. Relabelling $n, k \to 2n, 2k$ to only account for terms with an even number of external π lines, we find

$$\begin{aligned} \frac{V_{\text{eff}}(\tilde{\Pi}_2)}{N} = \frac{\tilde{\Pi}_2^2}{2\tilde{g}^2} - \int_{\boldsymbol{p}} \log\left(1 + \frac{\tilde{\Pi}_2^2}{p^2 + \tilde{m}^2}\right) + \int_{\boldsymbol{p}} \sum_{n=1}^{\infty} \left(-\frac{\tilde{\Pi}_2^2}{p^2 + \tilde{m}^2}\right)^n \\ \times \sum_{k=1}^{n} \left(\frac{p_2^2}{p^2 + \tilde{m}^2}\right)^k \mathscr{A}_{2k}\, n(n^2 - 1^2)(n^2 - 2^2) \cdots (n^2 - (k-1)^2), \end{aligned} \tag{C.10}$$

where the first radiative term comes from resumming the series in n for the aforementioned $k = 0$ term, where we have used $\ln(1 + z) = \sum_{n=1}^{\infty} (-z)^n / n$ for the parameter

$$z = \frac{\tilde{\Pi}_2^2}{p^2 + \tilde{m}^2}, \tag{C.11}$$

such that convergence requires $|z| < 1$. We note that in the standard effective potential for continuum four-Fermi QFTs [112], where the σ field couples to the $(\overline{\Psi}\Psi)$ bilinear, all the radiative quantum corrections to the classical potential are contained in a term that is completely analogous to this one

$$\delta V_{\text{q},1} = -N \int_{\boldsymbol{p}} \log\left(1 + \frac{\tilde{\Pi}_2^2}{p^2 + \tilde{m}^2}\right) \tag{C.12}$$

after making the substitution $\tilde{\Pi}_2 \to \tilde{\sigma}$. Accordingly, the consequence of using a different π channel is that there are additional quantum corrections contained in the remaining contributions for $k \in \{1, 2, 3, \ldots\}$ of Eq. (C.10). Accounting for these new radiative corrections is crucial to find the correct phase diagram, identifying the regions that delimit the correlated QAH phase.

Let us now describe how to perform the resummation of these additional corrections. The idea is to focus on the different k contributions separately, performing the sums over n to arbitrary orders of the coupling strength, here corresponding to arbitrary pairs of external lines, by means of the

following generating functions

$$S_\ell(z) = \sum_n n^\ell (-z)^n = \left(z\frac{d}{dz}\right)^\ell \frac{1}{1+z}.$$

Note that the contributions in Eq. (C.10) of order $\mathcal{O}(p_2^{2k})$, considering a fixed value of k, can be expressed in terms of a combination of generating functions $\{S_{2r-1}(z)\}_{r=1}^k$, e.g. for $k = 2$ one gets a contribution proportional to $S_3(z) - S_1(z)$. Each of these generating functions is a rational function $P_{2k-1}(z)/(1+z)^{2k}$, the numerator of which $P_{2k-1}(z)$ is a polynomial of order $2k-1$. In light of Eq. (C.11), $z \propto \tilde{\Pi}_1^2$, and one would then expect that each k term has a different polynomial dependence on the π condensate, such that resummation cannot be performed. Remarkably, we find that the prefactors that multiply the generating functions inside each of the polynomials $P_{2k-1}(z)$ cancel all terms except for one scaling with z^k, e.g. for $k = 2$, we get $P_3(z) = 6z^2$. This leads to a scaling with the condensate of order $\mathcal{O}(\tilde{\Pi}_2^{2k})$ that can now be resummed. The first few terms of these additional quantum-mechanical corrections to the effective potential read

$$\frac{\delta V_{\mathrm{q},2}(\tilde{\Pi}_2)}{N} \approx \frac{1}{2}\int_{\boldsymbol{p}} \left(\frac{4p_2^2\tilde{\Pi}_2^2}{(p^2+\tilde{m}^2+\tilde{\Pi}_2^2)^2} + \frac{1}{2}\left(\frac{4p_2^2\tilde{\Pi}_2^2}{(p^2+\tilde{m}^2+\tilde{\Pi}_2^2)^2}\right)^2 + \frac{1}{3}\left(\frac{4p_2^2\tilde{\Pi}_2^2}{(p^2+\tilde{m}^2+\tilde{\Pi}_2^2)^2}\right)^3 + \frac{1}{4}\left(\frac{4p_2^2\tilde{\Pi}_2^2}{(p^2+\tilde{m}^2+\tilde{\Pi}_2^2)^2}\right)^4 + \cdots \right). \tag{C.13}$$

The particular form of these last four terms suggests that a resummation is possible using again the Taylor series of the logarithm series, such that

$$\delta V_{\mathrm{q},2}(\tilde{\Pi}_2) = -\frac{N}{2}\int_{\boldsymbol{p}} \log\left(1 - \frac{4p_2^2\tilde{\Pi}_2^2}{(p^2+\tilde{m}^2+\tilde{\Pi}_2^2)^2}\right).$$

References

[1] S. Sachdev, Quantum Phase Transitions, second ed., Cambridge University Press, 2011.
[2] L. Landau, Zh. Eksp. Teor. Fiz. 7 (1937) 19, [Phys. Z. Sowjetunion 11, 26 (1937)].
[3] V.L. Ginzburg, L.D. Landau, Zh. Eksp. Teor. Fiz. 20 (1950) 1064.
[4] P.W. Anderson, Science 177 (1972) 393–396.
[5] A. Altland, B. Simons, Condensed Matter Field Theory, Cambridge University Press, 2006, pp. i–iv.
[6] P. Fazekas, Lecture Notes on Electron Correlation and Magnetism, World Scientific, 1999.
[7] J. Hubbard, Proc. R. Soc. Lond. Ser. A Math. Phys. Eng. Sci. 276 (1963) 238–257.
[8] M. Imada, A. Fujimori, Y. Tokura, Rev. Modern Phys. 70 (1998) 1039–1263.
[9] P.W. Anderson, Phys. Rev. 79 (1950) 350–356.
[10] P.W. Anderson, in: F. Seitz, D. Turnbull (Eds.), Solid State Physics, vol. 14, Academic Press, 1963, pp. 99–214.
[11] P.W. Anderson, Science 235 (1987) 1196–1198.
[12] P.A. Lee, N. Nagaosa, X.-G. Wen, Rev. Modern Phys. 78 (2006) 17–85.
[13] E. Fermi, Z. Phys. 88 (1934) 161–177.
[14] F.L. Wilson, Am. J. Phys. 36 (1968) 1150–1160.
[15] Y. Nambu, G. Jona-Lasinio, Phys. Rev. 122 (1961) 345–358.
[16] Y. Nambu, G. Jona-Lasinio, Phys. Rev. 124 (1961) 246–254.
[17] S.P. Klevansky, Rev. Modern Phys. 64 (1992) 649–708.
[18] D.J. Gross, A. Neveu, Phys. Rev. D 10 (1974) 3235–3253.
[19] K.G. Wilson, Phys. Rev. D 10 (1974) 2445–2459.
[20] C. Gattringer, C.B. Lang, Quantum Chromodynamics on the Lattice: An Introductory Presentation, Springer, 2010.
[21] S. Hands, Fixed point four-Fermi theories, 1997, arXiv:hep-lat/9706018.
[22] M. Creutz, Quarks, Gluons and Lattices, Cambridge University Press, 1997.
[23] A.H. Castro Neto, F. Guinea, N.M.R. Peres, K.S. Novoselov, A.K. Geim, Rev. Modern Phys. 81 (2009) 109–162.
[24] N.P. Armitage, E.J. Mele, A. Vishwanath, Rev. Modern Phys. 90 (2018) 015001.
[25] X.-L. Qi, S.-C. Zhang, Rev. Modern Phys. 83 (2011) 1057–1110.
[26] M.Z. Hasan, C.L. Kane, Rev. Modern Phys. 82 (2010) 3045–3067.
[27] A.P. Schnyder, S. Ryu, A. Furusaki, A.W.W. Ludwig, Phys. Rev. B 78 (2008) 195125.

[28] A. Kitaev, AIP Conf. Proc. 1134 (2009) 22–30.
[29] C.-K. Chiu, J.C.Y. Teo, A.P. Schnyder, S. Ryu, Rev. Modern Phys. 88 (2016) 035005.
[30] A. Soumyanarayanan, N. Reyren, A. Fert, C. Panagopoulos, Nature 539 (2016) 509–517.
[31] K.v. Klitzing, G. Dorda, M. Pepper, Phys. Rev. Lett. 45 (1980) 494–497.
[32] D.J. Thouless, M. Kohmoto, M.P. Nightingale, M. den Nijs, Phys. Rev. Lett. 49 (1982) 405–408.
[33] M. Nakahara, Geometry, Topology and Physics, CRC Press, 2017.
[34] Q. Niu, D.J. Thouless, Y.-S. Wu, Phys. Rev. B 31 (1985) 3372.
[35] B.I. Halperin, Phys. Rev. B 25 (1982) 2185–2190.
[36] Y. Hatsugai, Phys. Rev. Lett. 71 (1993) 3697–3700.
[37] F.D.M. Haldane, Phys. Rev. Lett. 61 (1988) 2015–2018.
[38] X.-L. Qi, Y.-S. Wu, S.-C. Zhang, Phys. Rev. B 74 (2006) 085308.
[39] X.-L. Qi, T.L. Hughes, S.-C. Zhang, Phys. Rev. B 78 (2008) 195424.
[40] C.-X. Liu, S.-C. Zhang, X.-L. Qi, Annu. Rev. Condens. Matter Phys. 7 (2016) 301–321.
[41] C.L. Kane, E.J. Mele, Phys. Rev. Lett. 95 (2005) 146802.
[42] C.L. Kane, E.J. Mele, Phys. Rev. Lett. 95 (2005) 226801.
[43] A.J. Niemi, G.W. Semenoff, Phys. Rev. Lett. 51 (1983) 2077–2080.
[44] A.N. Redlich, Phys. Rev. Lett. 52 (1984) 18–21.
[45] A.N. Redlich, Phys. Rev. D 29 (1984) 2366–2374.
[46] G.W. Semenoff, Phys. Rev. Lett. 53 (1984) 2449–2452.
[47] H.B. Nielsen, M. Ninomiya, Nuclear Phys. B 185 (1981) 20–40.
[48] H.B. Nielsen, M. Ninomiya, Nuclear Phys. B 193 (1981) 173–194.
[49] K.G. Wilson, New Phenomena in Subnuclear Physics, Springer US, 1977, pp. 69–142.
[50] J. Kogut, L. Susskind, Phys. Rev. D 11 (1975) 395–408.
[51] D.B. Kaplan, Phys. Lett. B 288 (1992) 342–347.
[52] H. So, Progr. Theoret. Phys. 73 (1985) 528–532.
[53] M.F.L. Golterman, K. Jansen, D.B. Kaplan, Phys. Lett. B 301 (1993) 219–223.
[54] C.-Z. Chang, J. Zhang, X. Feng, J. Shen, Z. Zhang, M. Guo, K. Li, Y. Ou, P. Wei, L.-L. Wang, Z.-Q. Ji, Y. Feng, S. Ji, X. Chen, J. Jia, X. Dai, Z. Fang, S.-C. Zhang, K. He, Y. Wang, L. Lu, X.-C. Ma, Q.-K. Xue, Science 340 (2013) 167–170.
[55] C.-Z. Chang, W. Zhao, D.Y. Kim, H. Zhang, B.A. Assaf, D. Heiman, S.-C. Zhang, C. Liu, M.H.W. Chan, J.S. Moodera, Nature Mater. 14 (2015) 473–477.
[56] R. Yu, W. Zhang, H.-J. Zhang, S.-C. Zhang, X. Dai, Z. Fang, Science 329 (2010) 61–64.
[57] Y. Deng, Y. Yu, M.Z. Shi, Z. Guo, Z. Xu, J. Wang, X.H. Chen, Y. Zhang, Science 367 (2020) 895–900.
[58] Y.-F. Zhao, R. Zhang, R. Mei, L.-J. Zhou, H. Yi, Y.-Q. Zhang, J. Yu, R. Xiao, K. Wang, N. Samarth, M.H.W. Chan, C.-X. Liu, C.-Z. Chang, Nature 588 (2020) 419–423.
[59] Y.-F. Zhao, R. Zhang, L.-J. Zhou, R. Mei, Z.-J. Yan, M.H.W. Chan, C.-X. Liu, C.-Z. Chang, Zero magnetic field plateau phase transition in higher Chern number quantum anomalous Hall insulators, 2021, arXiv:2109.11382.
[60] M. Hohenadler, F.F. Assaad, J. Phys.: Condens. Matter. 25 (2013) 143201.
[61] E.J. Bergholtz, Z. Liu, Internat. J. Modern Phys. B 27 (2013) 1330017.
[62] T. Neupert, C. Chamon, T. Iadecola, L.H. Santos, C. Mudry, Phys. Scr. T164 (2015) 014005.
[63] S. Rachel, Rep. Progr. Phys. 81 (2018) 116501.
[64] Y. Hatsugai, J. Phys. Soc. Japan 75 (2006) 123601.
[65] K. Kudo, H. Watanabe, T. Kariyado, Y. Hatsugai, Phys. Rev. Lett. 122 (2019) 146601.
[66] Z. Wang, X.-L. Qi, S.-C. Zhang, Phys. Rev. Lett. 105 (2010) 256803.
[67] V. Gurarie, Phys. Rev. B 83 (2011) 085426.
[68] Z. Wang, S.-C. Zhang, Phys. Rev. X 2 (2012) 031008.
[69] Z. Wang, S.-C. Zhang, Phys. Rev. B 86 (2012) 165116.
[70] Z. Wang, B. Yan, J. Phys.: Condens. Matter. 25 (2013) 155601.
[71] H. Li, F.D.M. Haldane, Phys. Rev. Lett. 101 (2008) 010504.
[72] F. Pollmann, A.M. Turner, E. Berg, M. Oshikawa, Phys. Rev. B 81 (2010) 064439.
[73] M.P. Zaletel, R.S.K. Mong, F. Pollmann, J. Stat. Mech. Theory Exp. 2014 (2014) P10007.
[74] J.C. Budich, R. Thomale, G. Li, M. Laubach, S.-C. Zhang, Phys. Rev. B 86 (2012) 201407.
[75] L. Wang, H. Jiang, X. Dai, X.C. Xie, Phys. Rev. B 85 (2012) 235135.
[76] S. Raghu, X.-L. Qi, C. Honerkamp, S.-C. Zhang, Phys. Rev. Lett. 100 (2008) 156401.
[77] K. Sun, H. Yao, E. Fradkin, S.A. Kivelson, Phys. Rev. Lett. 103 (2009) 046811.
[78] W. Zhu, S.-S. Gong, T.-S. Zeng, L. Fu, D.N. Sheng, Phys. Rev. Lett. 117 (2016) 096402.
[79] S. Kourtis, M. Daghofer, Phys. Rev. Lett. 113 (2014) 216404.
[80] D. González-Cuadra, A. Dauphin, P.R. Grzybowski, P. Wójcik, M. Lewenstein, A. Bermudez, Phys. Rev. B 99 (2019) 045139.
[81] D. González-Cuadra, A. Bermudez, P.R. Grzybowski, M. Lewenstein, A. Dauphin, Nature Commun. 10 (2019) 2694.
[82] D. Pesin, L. Balents, Nat. Phys. 6 (2010) 376–381.
[83] T. Neupert, L. Santos, C. Chamon, C. Mudry, Phys. Rev. Lett. 106 (2011) 236804.
[84] N. Regnault, B.A. Bernevig, Phys. Rev. X 1 (2011) 021014.
[85] D.N. Sheng, Z.-C. Gu, K. Sun, L. Sheng, Nature Commun. 2 (2011) 389.
[86] M. Serlin, C.L. Tschirhart, H. Polshyn, Y. Zhang, J. Zhu, K. Watanabe, T. Taniguchi, L. Balents, A.F. Young, Science 367 (2020) 900–903.

[87] K.P. Nuckolls, M. Oh, D. Wong, B. Lian, K. Watanabe, T. Taniguchi, B.A. Bernevig, A. Yazdani, Nature 588 (2020) 610–615.
[88] Y. Saito, J. Ge, L. Rademaker, K. Watanabe, T. Taniguchi, D.A. Abanin, A.F. Young, Nat. Phys. 17 (2021) 478–481.
[89] Y. Choi, H. Kim, Y. Peng, A. Thomson, C. Lewandowski, R. Polski, Y. Zhang, H.S. Arora, K. Watanabe, T. Taniguchi, J. Alicea, S. Nadj-Perge, Nature 589 (2021) 536–541.
[90] Y. Xie, A.T. Pierce, J.M. Park, D.E. Parker, E. Khalaf, P. Ledwith, Y. Cao, S.H. Lee, S. Chen, P.R. Forrester, K. Watanabe, T. Taniguchi, A. Vishwanath, P. Jarillo-Herrero, A. Yacoby, Fractional Chern insulators in magic-angle twisted bilayer graphene, 2021, arXiv:2107.10854.
[91] E.M. Spanton, A.A. Zibrov, H. Zhou, T. Taniguchi, K. Watanabe, M.P. Zaletel, A.F. Young, Science 360 (2018) 62–66.
[92] I. Bloch, J. Dalibard, W. Zwerger, Rev. Modern Phys. 80 (2008) 885.
[93] R.P. Feynman, Internat. J. Theoret. Phys. 21 (1982) 467.
[94] J.I. Cirac, P. Zoller, Nat. Phys. 8 (2012) 264–266.
[95] N. Goldman, J.C. Budich, P. Zoller, Nat. Phys. 12 (2016) 639–645.
[96] I.M. Georgescu, S. Ashhab, F. Nori, Rev. Modern Phys. 86 (2014) 153–185.
[97] M. Lewenstein, A. Sanpera, V. Ahufinger, B. Damski, A. Sen(De), U. Sen, Adv. Phys. 56 (2007) 243–379.
[98] I. Bloch, J. Dalibard, S. Nascimbène, Nat. Phys. 8 (2012) 267–276.
[99] T. Esslinger, Annu. Rev. Condens. Matter Phys. 1 (2010) 129–152.
[100] U.-J. Wiese, Ann. Phys. 525 (2013) 777–796.
[101] E. Zohar, J.I. Cirac, B. Reznik, Rep. Progr. Phys. 79 (2015) 014401.
[102] M. Dalmonte, S. Montangero, Contemp. Phys. 57 (2016) 388–412.
[103] M.C. Bañuls, R. Blatt, J. Catani, A. Celi, J.I. Cirac, M. Dalmonte, L. Fallani, K. Jansen, M. Lewenstein, S. Montangero, C.A. Muschik, B. Reznik, E. Rico, L. Tagliacozzo, K. Van Acoleyen, F. Verstraete, U.-J. Wiese, M. Wingate, J. Zakrzewski, P. Zoller, Eur. Phys. J. D 74 (2020) 165.
[104] M.C. Bañuls, K. Cichy, Rep. Progr. Phys. 83 (2020) 024401.
[105] V. Kasper, G. Juzeliunas, M. Lewenstein, F. Jendrzejewski, E. Zohar, From the Jaynes-Cummings model to non-Abelian gauge theories: A guided tour for the quantum engineer, 2020, arXiv:2006.01258.
[106] M. Aidelsburger, L. Barbiero, A. Bermudez, T. Chanda, A. Dauphin, D. González-Cuadra, P.R. Grzybowski, S. Hands, F. Jendrzejewski, J. Jünemann, G. Juzeliunas, V. Kasper, A. Piga, S.-J. Ran, M. Rizzi, G. Sierra, L. Tagliacozzo, E. Tirrito, T.V. Zache, J. Zakrzewski, E. Zohar, M. Lewenstein, Cold atoms meet lattice gauge theory, 2021, arXiv:2106.03063 [cond-mat.quant-gas].
[107] E. Zohar, Quantum simulation of lattice gauge theories in more than one space dimension – Requirements, challenges, methods, 2021, arXiv:2106.04609 [quant-ph].
[108] N. Klco, A. Roggero, M.J. Savage, Standard model physics and the digital quantum revolution: Thoughts about the interface, 2021, arXiv:2107.04769 [quant-ph].
[109] G. Jotzu, M. Messer, R. Desbuquois, M. Lebrat, T. Uehlinger, D. Greif, T. Esslinger, Nature 515 (2014) 237–240.
[110] S. Hands, A. Kocic, J.B. Kogut, Ann. Physics 224 (1993) 29–89.
[111] J. Braun, J. Phys. G: Nucl. Part. Phys. 39 (2012) 033001.
[112] S. Coleman, Aspects of Symmetry: Selected Erice Lectures, Cambridge University Press, 1985.
[113] C. Chin, R. Grimm, P. Julienne, E. Tiesinga, Rev. Modern Phys. 82 (2010) 1225–1286.
[114] M. Reitter, J. Näger, K. Wintersperger, C. Sträter, I. Bloch, A. Eckardt, U. Schneider, Phys. Rev. Lett. 119 (2017) 200402.
[115] K. Wintersperger, M. Bukov, J. Näger, S. Lellouch, E. Demler, U. Schneider, I. Bloch, N. Goldman, M. Aidelsburger, Phys. Rev. X 10 (2020) 011030.
[116] A. Eckardt, Rev. Modern Phys. 89 (2017) 011004.
[117] L. Ziegler, E. Tirrito, M. Lewenstein, S. Hands, A. Bermudez, Correlated Chern insulators in two-dimensional Raman lattices: A cold-atom regularization of strongly-coupled four-Fermi field theories, 2020, arXiv:2011.08744 [cond-mat.quant-gas].
[118] V. Galitski, I.B. Spielman, Nature 494 (2013) 49–54.
[119] H. Zhai, Rep. Progr. Phys. 78 (2015) 026001.
[120] L. Zhang, X.-J. Liu, Synthetic Spin-Orbit Coupling in Cold Atoms, pp. 1–87, Chapter 1.
[121] X.-J. Liu, K.T. Law, T.K. Ng, Phys. Rev. Lett. 112 (2014) 086401.
[122] X.-J. Liu, K.T. Law, T.K. Ng, Phys. Rev. Lett. 113 (2014) 059901.
[123] Z. Wu, L. Zhang, W. Sun, X.-T. Xu, B.-Z. Wang, S.-C. Ji, Y. Deng, S. Chen, X.-J. Liu, J.-W. Pan, Science 354 (2016) 83–88.
[124] W. Sun, B.-Z. Wang, X.-T. Xu, C.-R. Yi, L. Zhang, Z. Wu, Y. Deng, X.-J. Liu, S. Chen, J.-W. Pan, Phys. Rev. Lett. 121 (2018) 150401.
[125] B. Song, L. Zhang, C. He, T.F.J. Poon, E. Hajiyev, S. Zhang, X.-J. Liu, G.-B. Jo, Sci. Adv. 4 (2018).
[126] M.-C. Liang, Y.-D. Wei, L. Zhang, X.-J. Wang, H. Zhang, W.-W. Wang, W. Qi, X.-J. Liu, X. Zhang, Realization of Qi-Wu-Zhang model in spin-orbit-coupled ultracold fermions, 2021, arXiv:2109.08885 [cond-mat.quant-gas].
[127] L. Susskind, Phys. Rev. D 16 (1977) 3031–3039.
[128] A. Bermudez, L. Mazza, M. Rizzi, N. Goldman, M. Lewenstein, M.A. Martin-Delgado, Phys. Rev. Lett. 105 (2010) 190404.
[129] D.B. Kaplan, S. Sun, Phys. Rev. Lett. 108 (2012) 181807.
[130] J. Jünemann, A. Piga, S.-J. Ran, M. Lewenstein, M. Rizzi, A. Bermudez, Phys. Rev. X 7 (2017) 031057.
[131] A. Bermudez, E. Tirrito, M. Rizzi, M. Lewenstein, S. Hands, Ann. Physics 399 (2018) 149–180.
[132] Y. Kuno, Phys. Rev. B 99 (2019) 064105.

[133] E. Tirrito, M. Rizzi, G. Sierra, M. Lewenstein, A. Bermudez, Phys. Rev. B 99 (2019) 125106.
[134] G. Roose, N. Bultinck, L. Vanderstraeten, F. Verstraete, K. Van Acoleyen, J. Haegeman, J. High Energy Phys. 2021 (2021) 207.
[135] S. Sen, Phys. Rev. D 102 (2020) 094520.
[136] S. Ryu, A.P. Schnyder, A. Furusaki, A.W.W. Ludwig, New J. Phys. 12 (2010) 065010.
[137] K.G. Wilson, J. Kogut, Phys. Rep. 12 (1974) 75–199.
[138] R. Shankar, Rev. Modern Phys. 66 (1994) 129–192.
[139] M. Creutz, Phys. Rev. Lett. 83 (1999) 2636–2639.
[140] A. Bermudez, D. Patanè, L. Amico, M.A. Martin-Delgado, Phys. Rev. Lett. 102 (2009) 135702.
[141] O. Viyuela, A. Rivas, M.A. Martin-Delgado, Phys. Rev. Lett. 112 (2014) 130401.
[142] M. Tovmasyan, S. Peotta, P. Törmä, S.D. Huber, Phys. Rev. B 94 (2016) 245149.
[143] S. Takayoshi, H. Katsura, N. Watanabe, H. Aoki, Phys. Rev. A 88 (2013) 063613.
[144] N. Sun, L.-K. Lim, Phys. Rev. B 96 (2017) 035139.
[145] J.H. Kang, J.H. Han, Y. Shin, Phys. Rev. Lett. 121 (2018) 150403.
[146] R. Mondaini, G.G. Batrouni, B. Grémaud, Phys. Rev. B 98 (2018) 155142.
[147] D. González-Cuadra, L. Tagliacozzo, M. Lewenstein, A. Bermudez, Phys. Rev. X 10 (2020) 041007.
[148] O. Boada, A. Celi, J.I. Latorre, M. Lewenstein, Phys. Rev. Lett. 108 (2012) 133001.
[149] A. Celi, P. Massignan, J. Ruseckas, N. Goldman, I.B. Spielman, G. Juzeliūnas, M. Lewenstein, Phys. Rev. Lett. 112 (2014) 043001.
[150] M.V. Berry, Proc. R. Soc. A 392 (1984) 45–57.
[151] B.A. Bernevig, T.L. Hughes, Topological Insulators and Topological Superconductors, Princeton University Press, 2013.
[152] A.H. MacDonald, S.M. Girvin, D. Yoshioka, Phys. Rev. B 37 (1988) 9753–9756.
[153] Z. Nussinov, J. van den Brink, Rev. Modern Phys. 87 (2015) 1–59.
[154] W. Heisenberg, Z. Phys. 49 (1928) 619–636.
[155] A. Auerbach, Interacting Electrons and Quantum Magnetism, Springer-Verlag, 1994.
[156] Z. Nussinov, E. Fradkin, Phys. Rev. B 71 (2005) 195120.
[157] A. Kitaev, Ann. Physics 321 (2006) 2–111, (January special issue).
[158] M. Hermanns, I. Kimchi, J. Knolle, Annu. Rev. Condens. Matter Phys. 9 (2018) 17–33.
[159] J. Knolle, R. Moessner, Annu. Rev. Condens. Matter Phys. 10 (2019) 451–472.
[160] B. Douçot, M.V. Feigel'man, L.B. Ioffe, A.S. Ioselevich, Phys. Rev. B 71 (2005) 024505.
[161] A.Y. Kitaev, Ann. Physics 303 (2003) 2–30.
[162] S.B. Bravyi, A.Y. Kitaev, Quantum codes on a lattice with boundary, 1998, arXiv:quant-ph/9811052.
[163] M.H. Freedman, D.A. Meyer, Found. Comput. Math. 1 (2001) 325–332.
[164] E. Dennis, A. Kitaev, A. Landahl, J. Preskill, J. Math. Phys. 43 (2002) 4452–4505.
[165] F.J. Wegner, J. Math. Phys. 12 (1971) 2259–2272.
[166] J.B. Kogut, Rev. Modern Phys. 51 (1979) 659–713.
[167] E. Fradkin, Field Theories of Condensed Matter Physics, second ed., Cambridge University Press, 2013.
[168] D. Gottesman, Stabilizer codes and quantum error correction, 1997, arXiv:quant-ph/9705052.
[169] B.M. Terhal, Rev. Modern Phys. 87 (2015) 307–346.
[170] D. Bacon, Phys. Rev. A 73 (2006) 012340.
[171] D. Poulin, Phys. Rev. Lett. 95 (2005) 230504.
[172] P. Aliferis, A.W. Cross, Phys. Rev. Lett. 98 (2007) 220502.
[173] T.J. Yoder, Universal fault-tolerant quantum computation with Bacon-Shor codes, 2017, arXiv:1705.01686.
[174] J. Napp, J. Preskill, Optimal Bacon-Shor codes, 2012, arXiv:1209.0794 [quant-ph].
[175] M. Li, D. Miller, M. Newman, Y. Wu, K.R. Brown, Phys. Rev. X 9 (2019) 021041.
[176] S. Huang, K.R. Brown, Phys. Rev. A 101 (2020) 042312.
[177] J. Dorier, F. Becca, F. Mila, Phys. Rev. B 72 (2005) 024448.
[178] J. Villain, R. Bidaux, J.-P. Carton, R. Conte, J. Physique 41 (1980) 1263–1272.
[179] H.-D. Chen, C. Fang, J. Hu, H. Yao, Phys. Rev. B 75 (2007) 144401.
[180] R. Orús, A.C. Doherty, G. Vidal, Phys. Rev. Lett. 102 (2009) 077203.
[181] P.M. Chaikin, T.C. Lubensky, Principles of Condensed Matter Physics, Cambridge University Press, 1995.
[182] J.M. Radcliffe, J. Phys. A: Gen. Phys. 4 (1971) 313–323.
[183] F. Verstraete, J.I. Cirac, Renormalization algorithms for quantum-many body systems in two and higher dimensions, 2004, arXiv preprint cond-mat/0407066.
[184] F. Verstraete, V. Murg, J.I. Cirac, Adv. Phys. 57 (2008) 143–224.
[185] R. Orús, Ann. Physics 349 (2014) 117–158.
[186] S.-J. Ran, E. Tirrito, C. Peng, X. Chen, L. Tagliacozzo, G. Su, M. Lewenstein, Tensor Network Contractions: Methods and Applications to Quantum Many-Body Systems, Springer Nature, 2020.
[187] U. Schollwöck, Ann. Physics 326 (2011) 96–192.
[188] P. Corboz, Phys. Rev. B 94 (2016) 035133.
[189] M. Lubasch, J.I. Cirac, M.-C. Banuls, Phys. Rev. B 90 (2014) 064425.
[190] G. Vidal, Phys. Rev. Lett. 98 (2007) 070201.
[191] R. Orus, G. Vidal, Phys. Rev. B 78 (2008) 155117.
[192] J. Jordan, R. Orús, G. Vidal, F. Verstraete, J.I. Cirac, Phys. Rev. Lett. 101 (2008) 250602.
[193] R. Orús, G. Vidal, Phys. Rev. B 80 (2009) 094403.
[194] H.N. Phien, J.A. Bengua, H.D. Tuan, P. Corboz, R. Orús, Phys. Rev. B 92 (2015) 035142.
[195] R.J. Baxter, J. Stat. Phys. 19 (1978) 461–478.

[196] R.J. Baxter, Exactly Solved Models in Statistical Mechanics, Elsevier, 2016.
[197] T. Nishino, K. Okunishi, J. Phys. Soc. Japan 65 (1996) 891–894.
[198] P. Pfeuty, Ann. Physics 57 (1970) 79–90.
[199] J. Goldstone, A. Salam, S. Weinberg, Phys. Rev. 127 (1962) 965–970.
[200] K.G. Wilson, Phys. Rev. D 7 (1973) 2911–2926.
[201] S.-k. Ma, Rev. Modern Phys. 45 (1973) 589–614.
[202] S. Coleman, E. Weinberg, Phys. Rev. D 7 (1973) 1888–1910.
[203] S. Coleman, R. Jackiw, H.D. Politzer, Phys. Rev. D 10 (1974) 2491–2499.
[204] L. Dolan, R. Jackiw, Phys. Rev. D 9 (1974) 3320–3341.
[205] R.L. Stratonovich, Sov. Phys. 2 (1958) 416.
[206] J. Hubbard, Phys. Rev. Lett. 3 (1959) 77–78.
[207] P. Coleman, Introduction to Many-Body Physics, Cambridge University Press, 2015.
[208] J.W. Negele, H. Orland, Quantum Many-Particle Systems, CRC Press Taylor and Francis Group, 2019.
[209] M.E. Peskin, D.V. Schroeder, An Introduction to Quantum Field Theory, Addison-Wesley, Reading, USA, 1995.
[210] S. Aoki, Phys. Rev. D 30 (1984) 2653–2663.
[211] S. Sharpe, R. Singleton, Phys. Rev. D 58 (1998) 074501.
[212] T. Misumi, Y. Tanizaki, Prog. Theor. Exp. Phys. 2020 (2020).
[213] T. Misumi, J. Yumoto, Phys. Rev. D 102 (2020) 034516.
[214] F.D.M. Haldane, Phys. Lett. A 93 (1983) 464–468.
[215] F.D.M. Haldane, Phys. Rev. Lett. 50 (1983) 1153–1156.
[216] F. Karsch, Nuclear Phys. B 205 (1982) 285–300.
[217] G. Burgers, F. Karsch, A. Nakamura, I.O. Stamatescu, Nuclear Phys. B 304 (1988) 587–600.
[218] M. Alford, T.R. Klassen, G.P. Lepage, Nuclear Phys. B 496 (1997) 377–407.
[219] T.R. Klassen, Nuclear Phys. B 533 (1998) 557–575.
[220] C.J. Morningstar, M. Peardon, Phys. Rev. D 60 (1999) 034509.
[221] M. Okamoto, S. Aoki, R. Burkhalter, S. Ejiri, M. Fukugita, S. Hashimoto, K.-I. Ishikawa, N. Ishizuka, Y. Iwasaki, K. Kanaya, T. Kaneko, Y. Kuramashi, V. Lesk, K. Nagai, M. Okawa, Y. Taniguchi, A. Ukawa, T. Yoshié, CP-PACS Collaboration, Phys. Rev. D 65 (2002) 094508.
[222] A. Amato, G. Aarts, C. Allton, P. Giudice, S. Hands, J.-I. Skullerud, Phys. Rev. Lett. 111 (2013) 172001.
[223] G. Aarts, C. Allton, J. Glesaaen, S. Hands, B. Jäger, S. Kim, M.P. Lombardo, A. Nikolaev, S.M. Ryan, J. Skullerud, L.-K. Wu, Spectral quantities in thermal QCD: A progress report from the FASTSUM collaboration, 2019, arXiv:1912.09827 [hep-lat].
[224] C.L.Q.C. (CLQCD), X. Li, Y. Chen, G.-Z. Meng, X. Feng, M. Gong, S. He, G. Li, C. Liu, Y.-B. Liu, J.-P. Ma, X.-F. Meng, Y. Shen, J.-B. Zhang, 2007 (2007) 053.
[225] S. Hands, J. High Energy Phys. 2015 (2015) 47.
[226] S. Hands, Phys. Rev. D 99 (2019) 034504.
[227] S. Hands, M. Mesiti, J. Worthy, Phys. Rev. D 102 (2020) 094502.
[228] I. Montvay, G. Münster, Quantum Fields on a Lattice, in: Cambridge Monographs on Mathematical Physics, Cambridge University Press, 1994.
[229] R. Jackiw, Phys. Rev. D 9 (1974) 1686–1701.
[230] L.H. Thomas, Nature 117 (1926) 514.
[231] Y.A. Bychkov, E.I. Rashba, J. Phys. C: Solid State Phys. 17 (1984) 6039–6045.
[232] G. Dresselhaus, Phys. Rev. 100 (1955) 580–586.
[233] M. König, S. Wiedmann, C. Brüne, A. Roth, H. Buhmann, L.W. Molenkamp, X.-L. Qi, S.-C. Zhang, Science 318 (2007) 766–770.
[234] D. Hsieh, D. Qian, L. Wray, Y. Xia, Y.S. Hor, R.J. Cava, M.Z. Hasan, Nature 452 (2008) 970 EP.
[235] B.A. Bernevig, T.L. Hughes, S.-C. Zhang, Science 314 (2006) 1757–1761.
[236] P.A.M. Dirac, Proc. R. Soc. A 117 (1928) 610–624.
[237] P.A.M. Dirac, Proc. R. Soc. A 126 (1930) 360–365.
[238] S.S. Schweber, QED and the Men Who Made It: Dyson, Feynman, Schwinger, and Tomonaga, Vol. 104, Princeton University Press, 1994.
[239] R. Grimm, M. Weidemüller, Y.B. Ovchinnikov, in: B. Bederson, H. Walther (Eds.), Advances In Atomic, Molecular, and Optical Physics, vol. 42, Academic Press, 2000, pp. 95–170.
[240] B.-Z. Wang, Y.-H. Lu, W. Sun, S. Chen, Y. Deng, X.-J. Liu, Phys. Rev. A 97 (2018) 011605.
[241] S. Kolkowitz, S.L. Bromley, T. Bothwell, M.L. Wall, G.E. Marti, A.P. Koller, X. Zhang, A.M. Rey, J. Ye, Nature 542 (2017) 66–70.
[242] S.L. Bromley, S. Kolkowitz, T. Bothwell, D. Kedar, A. Safavi-Naini, M.L. Wall, C. Salomon, A.M. Rey, J. Ye, Nat. Phys. 14 (2018) 399–404.
[243] N.Q. Burdick, Y. Tang, B.L. Lev, Phys. Rev. X 6 (2016) 031022.
[244] B. Song, C. He, S. Zhang, E. Hajiyev, W. Huang, X.-J. Liu, G.-B. Jo, Phys. Rev. A 94 (2016) 061604.
[245] L.F. Livi, G. Cappellini, M. Diem, L. Franchi, C. Clivati, M. Frittelli, F. Levi, D. Calonico, J. Catani, M. Inguscio, L. Fallani, Phys. Rev. Lett. 117 (2016) 220401.
[246] X. Cui, B. Lian, T.-L. Ho, B.L. Lev, H. Zhai, Phys. Rev. A 88 (2013) 011601.
[247] M.L. Wall, A.P. Koller, S. Li, X. Zhang, N.R. Cooper, J. Ye, A.M. Rey, Phys. Rev. Lett. 116 (2016) 035301.
[248] F. Gerbier, J. Dalibard, 12 (2010) 033007.
[249] N. Goldman, G. Juzeliūnas, P. Öhberg, I.B. Spielman, 77 (2014) 126401.

[250] W. Kohn, Phys. Rev. 115 (1959) 809–821.
[251] D. Jaksch, C. Bruder, J.I. Cirac, C.W. Gardiner, P. Zoller, Phys. Rev. Lett. 81 (1998) 3108–3111.
[252] M. Greiner, O. Mandel, T. Esslinger, T.W. Hänsch, I. Bloch, Nature 415 (2002) 39.
[253] W. Hofstetter, J.I. Cirac, P. Zoller, E. Demler, M.D. Lukin, Phys. Rev. Lett. 89 (2002) 220407.
[254] W. Ketterle, D.S. Durfee, D.M. Stamper-Kurn, Making, probing and understanding Bose-Einstein condensates, 1999, arXiv:cond-mat/9904034.
[255] W. Ketterle, M.W. Zwierlein, Making, probing and understanding ultracold Fermi gases, 2008, arXiv:0801.2500.
[256] G.B. Partridge, W. Li, R.I. Kamar, Y.-a. Liao, R.G. Hulet, Science 311 (2006) 503–505.
[257] Y. Shin, M.W. Zwierlein, C.H. Schunck, A. Schirotzek, W. Ketterle, Phys. Rev. Lett. 97 (2006) 030401.
[258] S. Kuhr, Natl. Sci. Rev. 3 (2016) 170–172.
[259] W.S. Bakr, J.I. Gillen, A. Peng, S. Fölling, M. Greiner, Nature 462 (2009) 74–77.
[260] J.F. Sherson, C. Weitenberg, M. Endres, M. Cheneau, I. Bloch, S. Kuhr, Nature 467 (2010) 68–72.
[261] E. Haller, J. Hudson, A. Kelly, D.A. Cotta, B. Peaudecerf, G.D. Bruce, S. Kuhr, Nat. Phys. 11 (2015) 738–742.
[262] L.W. Cheuk, M.A. Nichols, K.R. Lawrence, M. Okan, H. Zhang, M.W. Zwierlein, Phys. Rev. Lett. 116 (2016) 235301.
[263] D. Greif, M.F. Parsons, A. Mazurenko, C.S. Chiu, S. Blatt, F. Huber, G. Ji, M. Greiner, Science 351 (2016) 953–957.
[264] C. Weitenberg, M. Endres, J.F. Sherson, M. Cheneau, P. Schauß, T. Fukuhara, I. Bloch, S. Kuhr, Nature 471 (2011) 319–324.
[265] M. Boll, T.A. Hilker, G. Salomon, A. Omran, J. Nespolo, L. Pollet, I. Bloch, C. Gross, Science 353 (2016) 1257–1260.
[266] M.F. Parsons, A. Mazurenko, C.S. Chiu, G. Ji, D. Greif, M. Greiner, Science 353 (2016) 1253–1256.
[267] L.W. Cheuk, M.A. Nichols, K.R. Lawrence, M. Okan, H. Zhang, E. Khatami, N. Trivedi, T. Paiva, M. Rigol, M.W. Zwierlein, Science 353 (2016) 1260–1264.
[268] M. Greiner, I. Bloch, O. Mandel, T.W. Hänsch, T. Esslinger, Phys. Rev. Lett. 87 (2001) 160405.
[269] M. Köhl, H. Moritz, T. Stöferle, K. Günter, T. Esslinger, Phys. Rev. Lett. 94 (2005) 080403.
[270] H.M. Price, N.R. Cooper, Phys. Rev. A 85 (2012) 033620.
[271] A. Dauphin, N. Goldman, Phys. Rev. Lett. 111 (2013) 135302.
[272] M. Aidelsburger, M. Lohse, C. Schweizer, M. Atala, J.T. Barreiro, S. Nascimbène, N.R. Cooper, I. Bloch, N. Goldman, Nature Phys. 11 (2014) 3171.
[273] X.-J. Liu, K.T. Law, T.K. Ng, P.A. Lee, Phys. Rev. Lett. 111 (2013) 120402.